Improving Thermal Cancer Treatment with 2D to 3D Heat Map Reconstruction

DISSERTATION

zur Erlangung des akademischen Grades

Doktoringenieur (Dr.-Ing.)

angenommen durch die Fakultät für Informatik

der Otto-von-Guericke-Universität Magdeburg

von

Julian Alpers, M. Sc.

geb. am 27.02.1992 in Hoya (Weser)

Gutachterinnen/Gutachter:

Prof. Dr. Christian Hansen

Prof. Dr. rer. nat. habil. Oliver Speck

Bruno Madore, PhD

Einreichungsdatum:

28. März 2023

Verteidigungsdatum:

22. September 2023

Magdeburg, October 24, 2023

Julian Alpers
Improving Thermal Cancer Treatment with 2D to 3D Heat Map Reconstruction
Dissertation, October 24, 2023
Supervisor: Prof. Dr. Christian Hansen

Otto-von-Guericke-Universität Magdeburg
Virtual and Augmented Reality Group
Institut für Simulation und Grafik
Fakultät für Informatik
Universitätsplatz 2
39106 Magdeburg

October 24, 2023
Version: Pflichtexemplar

Declaration

I hereby certify that I have prepared this thesis without the unauthorized assistance of third parties and without the use of resources other than those indicated; external and my own sources used are identified as such. In particular, I have not used the help of a commercial doctoral advisor. Third parties have neither directly nor indirectly received monetary benefits from me for work related to the content of the submitted dissertation. In particular, I did not knowingly:

- invent any results or conceal contradictory results,
- intentionally misuse statistical procedures to interpret data in an unjustified manner,
- plagiarize other people's results or publications,
- distort the results of other research.

I am aware that violations of copyright law may give rise to injunctive relief and claims for damages by the author as well as criminal prosecution by the law enforcing authorities. The work has not yet been submitted as a dissertation in the same or a similar form either in Germany or abroad and has not yet been published as a whole.

Magdeburg, October 24, 2023

Julian Alpers

Kurzfassung

Krebs ist eine sich schnell ausbreitende Krankheit mit vielen Behandlungsmöglichkeiten. Eine dieser Behandlungsmethoden ist der Einsatz von Wärmeenergie zur Zerstörung des bösartigen Gewebes, ohne dass eine offene Operation erforderlich ist. Bei diesen minimal-invasiven Verfahren ist die Überwachung der Wärmeverteilung ein dringender klinischer Bedarf. Mit Hilfe der MRT kann die Temperatur im Gewebe mit Methoden wie der Protonenresonanzfrequenzverschiebung berechnet werden. Bislang ist die Erfassung von volumetrischen Wärmekarten entweder auf die Entwicklung spezieller MR-Sequenzen oder auf die Verwendung interventioneller Simulationen beschränkt. Bei den MR-Sequenzen kann zwischen reinen 3D- und überlagerten 2D-Sequenzen unterschieden werden. Im Hinblick auf die interventionelle Simulation sind die Pennes'sche Biowärmeübertragungsgleichung in Kombination mit Levenberg-Marquardt-Schätzern und erweiterten Kalman-Filtern beliebte Ansätze. Dennoch haben sowohl der MR-Sequenzansatz als auch die Simulationsansätze Nachteile. Vollständige 3D-Sequenzen sind anfälliger für z. B. MR-Interferenzen und Bewegungen als 2D-Sequenzen. Für Simulationen mit dem Kalman-Filter ist die Einführung eines behandlungsspezifischen Wärmequellenterms erforderlich. Dieser Term erhöht den Rechenaufwand erheblich und erfordert viel A-priori-Wissen.

In dieser Arbeit wird ein Konzept für die Rekonstruktion von volumetrischen Wärmekarten vorgestellt. Dazu wird ein neues Sequenzprotokoll vorgestellt, das eine Standard-Gradient-Recalled-Echo-Sequenz verwendet, die in vielen klinischen Einrichtungen verfügbar ist. Diese 2D-Sequenz wird mit Hilfe einer Fernsteuerungsschnittstelle des Scanners um die Hauptachse des Applikators gedreht. Durch diese spezielle Art der Abtastung des 3D-Raums ist das resultierende Rekonstruktionsproblem weniger komplex und kann entweder mit üblichen Bildverarbeitungsmethoden oder einfachen Simulationsansätzen gelöst werden, ohne dass ein behandlungsspezifischer Wärmequellenterm eingeführt werden muss. Zu diesem Zweck wird in dieser Arbeit gezeigt, dass einfache 2D-zu-3D-Rekonstruktionsalgorithmen geeignet sind, eine volumetrische Wärmekarte zu rekonstruieren. Darüber hinaus wird ein neuer Ansatz für adpative Simulationen während des Eingriffs vorgestellt, um die Genauigkeit der berechneten volumetrischen Wärmekarten weiter zu erhöhen. Die in dieser Arbeit entwickelten Algorithmen können in einer Vielzahl von klinischen Situationen eingesetzt werden.

Abstract

Cancer is a rapidly spreading disease with many treatment options. One of these treatment procedures is the use of thermal energy to destroy the malignant tissue without the need of open surgery. During those minimally invasive procedures the monitoring of the heat distribution is an urgent clinical need. Using MRI, the temperature inside the tissue can be computed using methods like the proton resonance frequency shift. Until this time, the acquisition of volumetric heat maps is limited either to the development of special MR sequences or the use of intervetional simulations. Regarding the MR sequences, fully 3D and stack of 2D sequences can be divided. with respect to the inertventional simulation, the Pennes' bioheat transfer equation in combination with Levenberg-Marquardt estimators and extended Kalman filters are popular approaches. Nonetheless, the MR sequence approach as well as the simulation approaches yield disadvantages. Fully 3D sequences are more prone to e.g., MR interference and motion than 2D sequences. For simulations using the Kalman filter the introduction of a treatment specific heat source term is necessary. This term increases the computational effort significantly and requires much a priori knowledge.

In this thesis a concept for the reconstruction of volumetric heat maps is proposed. Here, a new sequence protocol is introduced, which utilizes a standard gradient-recalled echo sequence available to a wide range of clinical setups. This 2D sequence will be rotated around the applicator's main axis using a scanner remote control interface. By sampling the 3D space in this special way the resulting reconstruction problem is less complex and can be solved with either common image processing methods or simple simulation approaches without the introduction of a treatment specific heat source term. For this purpose, we will show that that simple 2D to 3D reconstruction algorithms are suitable to reconstruct a volumetric heat map. In addition, a new approach for adaptive simulations during the intervention is introduced to further increase the accuracy of the computed volumetric heat maps. The algorithms developed in this thesis will be applicable to a wide range of clinical setups.

Acknowledgement

The research conducted in this PhD thesis was funded by the Federal Ministry of Education and Research within the Forschungscampus STIMULATE under grant numbers ’13GW0095A’, ’13GW0473A’ and ’13GW0473B’; And by PRACTIS - Clinician Scientist Program, funded by the German Research Foundation (DFG, ME 3696/3- 1).

Contents

Acronyms

BHTE bioheat transfer equation.

DSC dice score coefficient.

EPI echo planar imaging.

FN false negatives.

FOV field of view.

FP false positives.

FPR false positive rate.

GM grey matter.

GRE gradient-recalled echo.

HBB hydrogen bridge bond.

HIFU (high) focused ultrasound.

LTP local tumor progression.

MAM minimum ablative margin.

MHH Hannover Medical School.

MPM material-to-points.

MR magnetic resonance.

MVEE minimum volume enclosing ellipsoid.

MWA microwave ablation.

PDF probability density function.

PRFS proton resonance frequency shift.

PVC polyvinyl chloride.

RF radiofrequency.

ROI region of interest.

SEM standard error of the mean.

SNR signal-to-noise-ratio.

TP true positives.

TSE turbo spin echo.

UMD University Hospital Magdeburg.

VOI volume of interest.

WM white matter.

1 Introduction

> *Modern Cancer Surgery someday will be regarded with the same kind of horror that we now regard the use of leeches in George Washington's time.*
>
> — **Dr. Robert Mendelsohn**
> American pediatrician

Cancer is a rapidly spreading disease. In 2018, the number of new cancer cases was estimated at around 17 million, with 9.5 million deaths (excluding nonmelanoma skin cancer) (Bray et al., 2018). In 2020, the numbers increased by 6.47% and 4.21% for new cases and deaths, respectively (Sung et al., 2021). In addition to open surgery, which usually yields a higher trauma for the patient, a wide range of minimally invasive therapies have been developed for cancer treatment over the past decades. Among these, mild hyperthermia has been proven to be able to enhance the efficacy of radiation and chemotherapy, the usual methods of treatment (VilasBoas-Ribeiro et al., 2022). Here, the tissue is heated up to 39°C - 43°C over a long period of time, causing the cells to irreversibly loose their functionality. Aside from these approaches, thermal ablation procedures have also been developed over the past decade (Ahmed et al., 2014; Mauri et al., 2017; Tomasian et al., 2018). In addition to radiofrequency (RF) and (high) focused ultrasound (HIFU) ablations, one of these methods is the use of microwave ablation (MWA). Especially for smaller tumors, MWA shows promising results for treatment (Tehrani et al., 2020).

To fully treat malignant tissue, it is important to not only destroy the malignant cells, but also ensure a corresponding safety margin. As this minimum ablative margin (MAM) is crucial for the local tumor progression (LTP), it is of greatest importance to assess if the malignancy has been adequately and completely treated, regardless of the etiology. For each millimeter increase of the MAM, a 30% reduction of the relative risk for LTP was found. The MAM itself is especially important as the only significant independent predictor of LTP ($p = 0.036$) (Laimer et al., 2020). During the intervention, magnetic resonance (MR) imaging offers several advantages for guidance, such as good soft-tissue contrast without the need of contrast agent, free

orientation and positioning of single slice scans and the possibility to accurately track changes in the temperature inside the tissue (MR thermometry) (Gorny et al., 2019; Kägebein et al., 2018; Rieke et al., 2008; Senneville et al., 2007).

Recently, Fedderson et al. (2020) performed an in-depth study on more than 4000 patients treated with superficial and deep hyperthermia. They were able to identify two major aspects: first, MR thermometry is the only non-invasive clinically accepted method to measure the heat distribution inside the human body. Second, up to now this method is only applicable in areas without motion, and little progress has been made for 20 years in applying this method to more challenging areas like the abdomen and thorax. Unfortunately, the research provided by Fedderson et al. (2020) focuses mainly on 2D MR thermometry approaches. 2D thermometry in a single slice is not capable of adequately monitoring whether the malignant tissue and the MAM have been fully treated. For this reason, it is necessary to investigate possibilities on how to extend the clinically accepted 2D thermometry to a volumetric approach.

In 2D thermometry, the proton resonance frequency shift (PRFS) method for thermometry computation is reported to be clinically accepted because of its linear behaviour and the near-independence of different tissue types (Rieke et al., 2008). Using MR-guidance in combination with the PRFS method, the heat distribution can be tracked during hyperthermia and thermal ablation procedures. Nonetheless, whether a volumetric thermometry map can be clinically acceptable, as well as whether the errors caused by respiratory motion, e.g., in the thorax can be minimized, remain open questions.

1.1 Problem Definition

During an initial literature research, the following problems and limitations regarding volumetric thermometry maps could be identified:

1. **Real-time Image Acquisition**

   3D volume acquisition using MR imaging involves a major trade-off between temporal and spatial resolution, especially with respect to temperature measurements. In order to acquire high accuracy temperature maps, the resolution of the acquired volume has to be sufficiently high enough with respect to the spacing of the voxels. To achieve this resolution, the acquisition time is increased depending on the used sequence. This increase in acquisition time

also increases the risk for MR inhomogeneities to arise and may decrease the signal-to-noise-ratio (SNR) significantly.

2. **Minimizing Motion Artifacts**

   An increased acquisition time also increases the risk for motion artifacts. Full anaesthesia minimizes the patient's body movement but always yields a risk for the patient. In addition, even during full anesthesia, the motion caused by breathing is not negligible. Therefore, 3D thermometry acquisition is usually paired with complex motion correction methods which increase the computational effort and reduce the real-time capabilities.

3. **Ease of Use**

   In general, 3D thermometry sequences can be capable of real-time image acquisition, but, to achieve this, they are usually unique, custom-made and utilize individual reconstruction pipelines. Therefore, they are not applicable to a wide range of clinical setups. Installation and operation of these sequences require special expertise or training, which can be troublesome in the daily routine of the hospitals.

4. **Coagulation Estimation**

   To aid radiologists during their decision process, it is necessary to provide real-time information about the current coagulation necrosis estimation. Many approaches for 3D thermometry acquisition use offline reconstruction and do not provide an intra-operative coagulation estimation.

Detailed information on the literature research can be found in the related Subchapters 3.2, 4.2, 5.2 and 6.2.

Derived from the current problems and limitations, the aim of the present work is to conceptualize, develop and evaluate a prototype for the monitoring of heat distributions during minimally invasive tumor ablation. Because the problems mentioned before can be more easily addressed in 2D, the focus is on the development of a volumetric thermometry map, which is based on already available 2D sequences. The proposed method must provide a reconstruction approach based on the derived temperature maps while being applicable (to a certain extent) to areas with high motion. In addition, the developed prototype shall be real-time capable in order to be used in a wide range of clinical contexts and it would be mandatory for a volumetric thermometry reconstruction to be at least as accurate as the current 2D state-of-the-art solution. Due to the lack of clinical patient data, all test data is acquired on bioprotein phantoms, as explained in Chapter 3. As a result of the use

of these phantoms, the critical temperature model is used for necrosis estimation as it is easily adaptable to the individual characteristics of each phantom. Yung et al. (2010) performed a quantitative analysis on thermal dose models, including the critical temperature threshold model. According to their analysis, a dice score coefficient (DSC) > 0.7 is excellent, and therefore clinically applicable in the context of 2D thermometry. Reported DSC values do not differ much with respect to the used thermal dose model. Regarding the critical temperature threshold, average results show a DSC > 0.8 with a maximum of up to 0.91. Taking this into account, the following research question can be formulated:

R1

"Can conventional image processing algorithms be used to reconstruct volumetric thermometry maps from 2D slices with at least 80% accuracy (DSC > 0.8) while being real-time capable?"

Another approach for the computation of volumetric heat maps is the use of simulations of the heat distribution. Here, Harry H. Pennes (1948) introduced a bioheat transfer equation (BHTE) to simulate the heat distribution in the forearm. Even though he made many assumptions without being able to prove them, his BHTE showed promising results. Fifty years later, Eugene H. Wissler (1998) revised the paper and was also able to reproduce the mathematical results from Pennes. The introduced simulation is very easy to compute but is also very prone to error accumulation. Nonetheless, this BHTE might be able to be utilized for volumetric thermometry reconstruction. By feeding the algorithm with live data and adapting the simulation parameters in real-time it should be possible to reduce the accumulated error over the time of the intervention. Therefore, a second research question can be formulated:

R2

"Is it possible to utilize the Pennes' Bioheat Transfer Equation to simulate the actual coagulation necrosis during thermal tumor ablation in real-time while avoiding simulation error accumulation?"

1.2 Concept Design

Based on the identified problems and the formulated research questions, the conceptional design for a prototype was developed. Aside from the integration of the

Siemens Healthineers' Access-I framework for direct control of the MR device, the focus lies on the 2D to 3D reconstruction module. A schematic overview of the proposed architectural design can be seen in Figure 1.1. Addressing the current

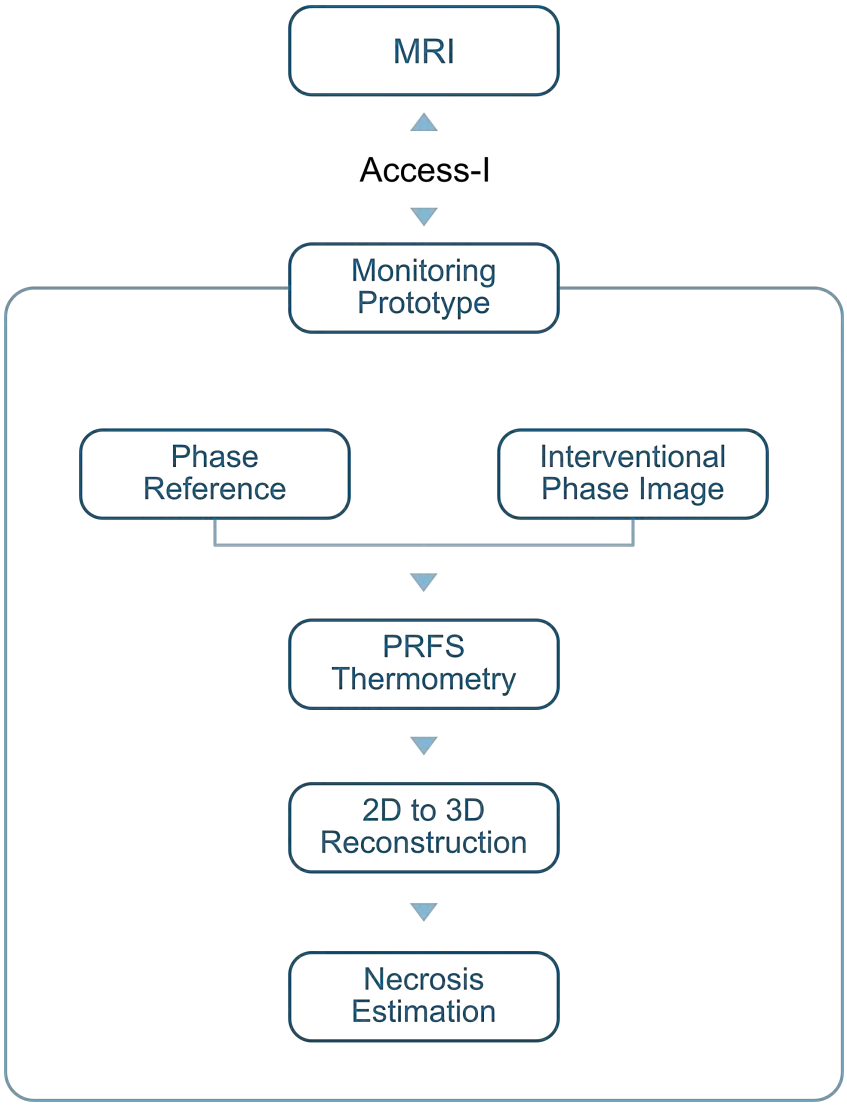

Fig. 1.1: General architectural diagram for the proposed prototype. Control of the MR device can be obtained by using the Access-I framework provided by Siemens Healthineers. The monitoring prototype consists of the following modules: 1) The already existing 2D thermometry based on the PRFS method. 2) The 2D to 3D reconstruction for volumetric thermometry computation to be developed in the present thesis. 3) The necrosis estimation based on state of the art thermal dose models.

limitations in the field of volumetric thermometry maps, the problem of real-time monitoring will be transferred from the domain of MR physics and MR sequence programming to that of computer science.

In the context of the present thesis, the term "real-time" is highly connected to the used imaging protocol. The consultation of clinical experts in the field of interventional radiology yielded the following (paraphrased by the author of the present work): "Real-time" in the context of minimally invasive radiology means that the processing of the images is faster than the continuous imaging technique used for guidance. In the case of an MR sequence, which takes one second for image acquisition, the processing of the acquired image and the resulting 2D to 3D reconstruction has to be less than one second to be considered "real-time". By focusing on conventional reconstruction algorithms and a very basic simulation approach, the computational effort can also be optimized to address the first limitation: *Real-time Image Acquisition*.

With respect to the image acquisition, a standardized MR sequence has to be available on a large scale of MR devices as default. One available sequence is a 2D gradient-recalled echo (GRE) sequence. This sequence is suitable for thermometry, as it is capable of not only generating magnitude images for diagnosis but also phase images for the PRFS method. In addition, Gorny et al. (2019) provide an in-depth analysis for the 2D GRE sequence regarding the breathing cycles of patients and the SNR during MWA. The sequence used should be based on the information given by their work. Furthermore, they claim that this sequence can be manually synchronized with the breathing cycle of the patient, minimizing the respiratory movement during intervention. By utilizing their research as an input for the 2D to 3D reconstruction, the second limitation *Minimizing Motion Artifacts* could be addressed adequately.

R1 refers to "conventional" image processing algorithms. For those, artificial intelligence is neglected and the input for those algorithms has to be available a priori or provided directly during the intervention. In order to provide a proper 2D to 3D reconstruction of a volumetric heat map, the volume of interest needs to be sampled in a sufficient way. Because the heat source of the applicator's main axis is a crucial factor during heat propagation, all acquired images should contain this heat source. A possible way to achieve this is the rotation around the applicator's main axis. Manual planning of the slice rotation for each individual patient and applicator will be difficult. So that it can still address the third limitation *Ease of Use*, the prototype must provide the possibility for taking control of the used MR device. Regarding Siemens devices, the Access-I framework provided by Siemens Healthineers can be utilized. This framework allows for not only fetching live images, but also for taking host control and rotate the 2D sequence around the applicator's main axis automatically.

Regarding R2, an alternative for conventional 2D to 3D reconstruction is the use of BHTEs for simulation of the heat propagation. Simulations in general do not rely on a frequent input of information. Using simulations, a continuous feedback loop can be achieved providing a better understanding of the distribution of the heat in between image acquisitions. Nonetheless, to be real-time capable in the context of minimally invasive radiology, the BHTE must not be to complex. Pennes' BHTE describes a simple optimization while being very prone to errors accumulating over time. Combining this approach with the continuous image information from the live data it should be possible to correct the error over time and thus optimizing the final outcome of the interventional simulation resulting in an increased accuracy of the last limitation *Coagulation Estimation*.

1.3 Thesis Structure

The present thesis describes the reconstruction of a volumetric thermometry map based on equally distributed 2D MR images for minimally invasive tumor ablation. The focus lies on the transferal of the problem from the domain of pure MR physics into the domain of computer science. To address the problem of volumetric thermometry reconstruction and to open this field to a broader range of researchers, the thesis is structured as follows:

- Chapter 2 introduces the technical and medical background information necessary to understand this thesis. This includes the physical properties of an MR device and the acquisition of thermometry maps, as well as the basic idea of MWA and the clinical procedure for minimally invasive interventions.
- Chapter 3 explains the proof-of-concept study conducted to test the feasibility of this thesis. Here, the generation of a bioprotein phantom data base is explained, in addition to a first basic 2D to 3D reconstruction approach.
- Chapter 4 conducts research regarding different conventional 2D to 3D approaches. Here, the focus lies on the identification of the optimal base setup. Factors considered are volume-based, layer-based and model-based approaches.
- Chapter 5 introduces a probabilistic thermal dose model based on the state-of-the-art CEM_{43} model. Here, the probability density function (PDF) from the complex phase image is derived and transformed into the thermal dose PDF

to compute a probabilistic necrosis map in order to increase the accuracy and therefore improve the input for the presented reconstruction methods.

- Based on the information gained in the previous chapters, Chapter 6 focuses on the development of an adaptive bio heat transfer simulation. The goal of this work is the utilization of the easy to compute Pennes' BHTE while reducing the accumulation error and preserving the real-time capabilities of the previous approaches.
- Chapter 7 concludes this thesis by summarizing the methods and contributions of the presented work and discussing their limitations and potential future work.

Background

2

> *An MRI scan can reveal a world of information, showing us the secrets hidden within our bodies and unlocking mysteries we never knew existed.*
>
> — **Dr. Sanjay Gupta**
> American neurosurgeon

The following chapter will describe the medical and technical background of the proposed methods. The focus lies on the MWA as the chosen method for thermal ablation, utilizing the MRI device for image guidance. Here, the basic principle of the device will be explained in more detail with focus on the creation of the thermometry images, using the PRFS method and one of the current used workflows.

2.1 Magnetic Resonance Tomography

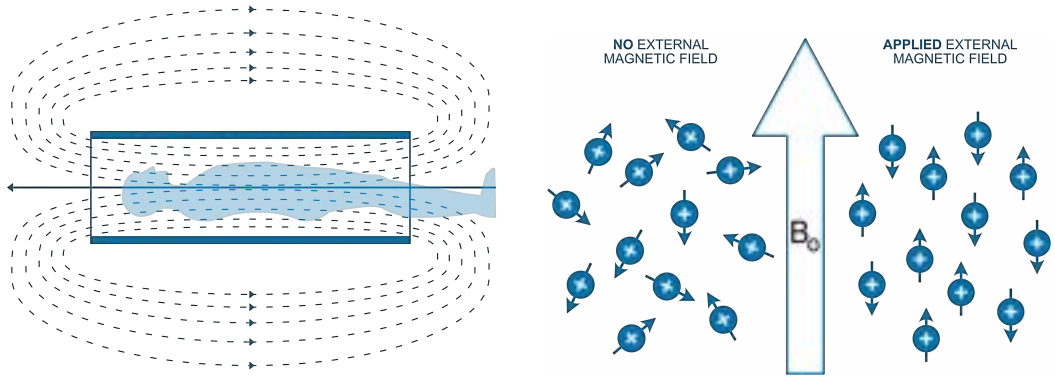

(a) Illustration of the main magnetic field created by the electric current in the looped wires of the MR device. Based on (Pooley, 2005).

(b) Illustration of the longitudinal aligned net magnetization. Based on (Pooley, 2005).

Fig. 2.1: Illustration of the main magnetic field and the proton precession.

One of the main parts of an MR device is the giant main magnetic field referred to as B_0, which is created by an electric current moving through looped wires (Figure

2.1a). In an MR device, these wires form a giant magnet perpendicular to the loop. This magnetic field is very stable with respect to the loss in power and magnetic field strength. After powering up the device and removing the power source the MR device, depending on the type, is able to maintain the electric current for several years. Nonetheless, the immense power input causes the wires to produce very high temperatures. To cope with the immense heat produced in this state, these wires are immersed in liquid helium to keep the different parts from breaking (Pooley, 2005).

Observing all kinds of atoms, it can be seen that atomic nuclei with an odd number of protons and/or neutrons (like hydrogen ^1H) have a "nuclear spin" I. The nuclear spin is always related to the magnetic momentum μ in the form:

$$\mu = \gamma I \tag{2.1}$$

with γ representing the characteristic gyromagnetic ratio for each nucleus (Reiser et al., 2007). In the normal state of the human body, the hydrogen protons are randomly aligned, causing their local magnetic fields to cancel out each other. Applying a strong magnetic field B_0 from the outside, forces these nuclei to align, creating a net magnetization parallel to B_0. An illustration can be seen in Figure 2.1b. This alignment results in an accumulation of the tiny magnetic fields, creating a larger local magnetic field. Nonetheless, even when aligned parallel or anti-parallel to B_0, the nuclei still have a magnetic momentum (Pooley, 2005). Therefore, they start spinning and precessing around the B_0 main axis as seen in Figure 2.2a.

To enforce a measurable response from the nuclei, a second RF magnetic field has to be applied e.g., through a body or head coil. Here, the flow current rapidly changes back and forth, causing the magnetic field created by the flow of electrons to also change direction rapidly. The RF signal is usually transmitted during a short time period. Each of these transmissions is called a single RF pulse. In order to optimize the energy transfer from the RF pulses to the protons the transmitted pulses must match the frequency of the precession of the protons (Pooley, 2005). This precession can be computed using the Larmor equation 2.2:

$$\omega_0 = \gamma B_0 \tag{2.2}$$

with ω_0 representing the proton precessional frequency, γ representing the nucleus dependent gyromagnetic constant (e.g., hydrogen protons = 42.6 MHz/T) and B_0 representing the magnetic field strength (e.g., 3T) (Grover et al., 2015). The nuclei absorb the energy from the RF pulses causing the net magnetization field to rotate

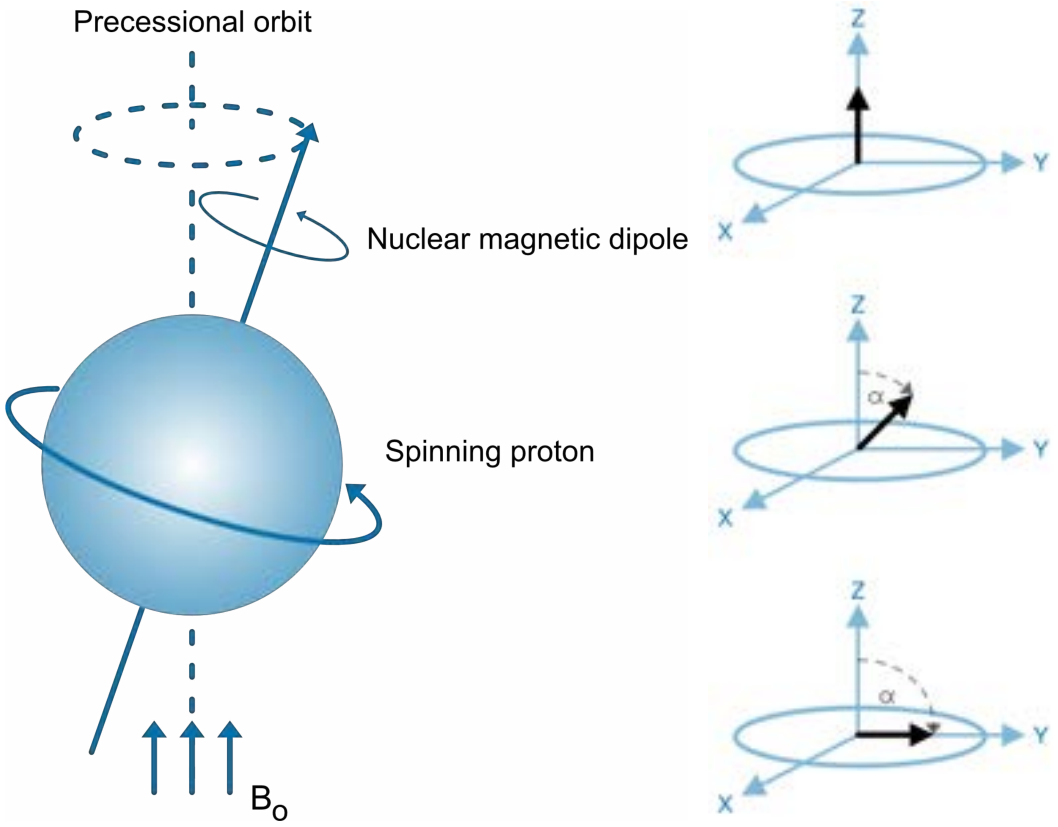

(a) Illustration of the precession of a nucleus around the main magnetic field B_0. Based on (Reiser et al., 2007).

(b) New angulation after RF pulse transmission. Based on (Pooley, 2005).

Fig. 2.2: Illustration of the net magnetization and the RF pulse transmition.

away from its initial orientation depending on the strength and length of the RF pulse (Figure 2.2b). The strength of the rotation towards the transversal x-y plane is referred to as the flip angle and it can be at any angle possible. In general, higher flip angles (e.g., 90° or 180°) are important when using spin echos while lower flip angles define faster imaging techniques like the GRE sequence used in this thesis (Pooley, 2005). The flip angle α can be computed using the gyromagnetic constant γ and the length of the RF pulse τ at a constant amplitude $\hat{B}_1$ (Brown et al., 2014):

$$\alpha = \gamma \hat{B}_1 \tau \tag{2.3}$$

The standard net magnetization, as explained previously, is aligned longitudinal, and therefore called longitudinal magnetization. By applying a 90° RF pulse, the longitudinal magnetization becomes zero as the whole magnetic field is rotated away from the longitudinal direction in the transverse plane. The following relaxation

can be divided into Spin-Lattice relaxation and Spin-Spin relaxation (Brown et al., 2014).

The Spin-Lattice interdependency describes the recurrence of the spins into the thermodynamic steady state, which correlates to the minimum energy state of the system. The constant to describe the time needed for aligning the spins parallel to the external magnetic field is called T_1. During this process, the exchange of energy mainly occurs with the crystal lattice (Brown et al., 2014).

The Spin-Spin interdependency is responsible for dissipation of the transversal magnetization. Here, the precession frequency of each nucleus varies because their local magnetic field is a combination of the external magnetic field and the individual magnetic field of each nucleus. This results in a different dephasing process of the individual spins, which is why the transversal magnetization decreases over time. The constant describing this time is called T_2 and is mainly dependent on the different tissue compositions in the human body. In addition, local inhomogeneities in the external magnetic field cause a faster dissipation of the transversal magnetization. This phenomenon is described as $T_2^{'}$ and is part of the final relaxation time T_2^* (Brown et al., 2014):

$$\frac{1}{T_2^*} = \frac{1}{T_2} + \frac{1}{T_2^*} \tag{2.4}$$

Figure 2.3 shows an illustration of the T_1 and T_2 related relaxation curves in comparison to white matter (WM) and grey matter (GM) in the brain. It can be observed that, the bigger the distance between the WM and GM curves, the higher the corresponding contrast.

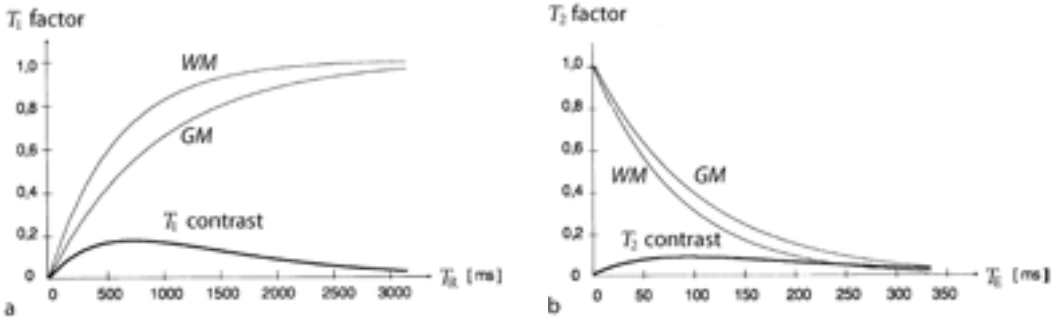

(a) Relaxation curves for T1 weighted images. **(b)** Relaxation curves for T2 weighted images.

Fig. 2.3: Image acquisition when the curves are furthest away from each other will result in high contrast images. Note that different tissue types show different relaxation times causing different intensities. Images taken from (Reiser et al., 2007).

The spatial enconding of the MR device can be described as the measurement of the transversal magnetization after the application of an RF-pulse. The time

point used for the measurement is specified by the echo time T_E. In addition, three independent gradient coils are used to create gradient fields in x-, y- and z-direction. The resulting magnetic field is overlapping the external magnetic field leading to local variations. The resulting spatial encoding process during one RF-pulse can be described by the following steps (Reiser et al., 2007):

1. *Slice-Selective Excitation.* In addition to the used RF-pulse, a gradient field is applied varying the Larmor frequency of the excited nuclei in a 2D slice. The width of the slice can be changed by changing the bandwidth of the RF-pulse, and the position can be changed by shifting the center frequency of the RF-pulse.

2. *Frequency Encoding.* During the readout of the transversal magnetization, the second gradient is applied constantly and orthogonal to the first one.

3. *Phase Encoding.* Between excitation of the nuclei and the readout of the transversal magnetization, a third gradient is applied orthogonal to the previous two. This gradient is applied for a certain time, after which the nuclei precess further but show different phases.

The results of this process are written down in a single row inside a matrix called k-space matrix. To ensure proper reconstruction of the anatomical image data, the k-space matrix has to be filled with an appropriate amount of data. Therefore, the process of spatial encoding is repeated several times using a repetition time T_R between each pulse. After filling the k-space matrix the image data can be decoded using the inverse Fourier transform. In order to visualize the morphological images, only the magnitude of the resulting complex signal is used (Paschal et al., 2004). An example for a magnitude and a phase image can be seen in Figure 2.4.

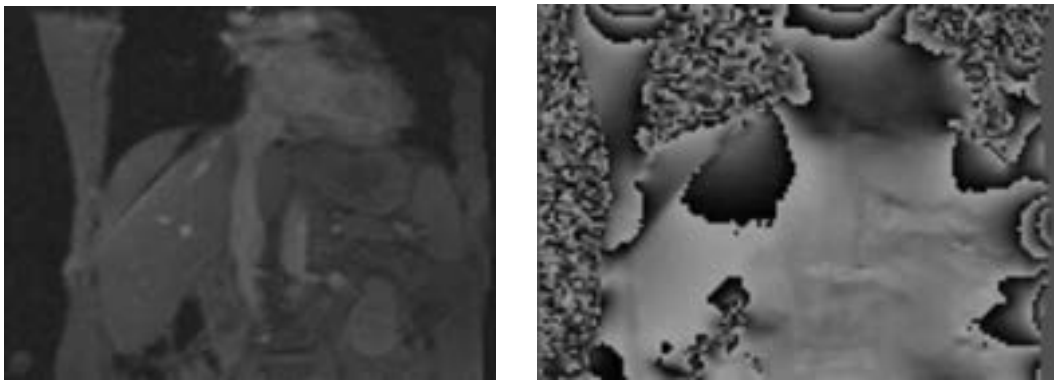

(a) Magnitude image of the liver. **(b)** Phase image of the liver.

Fig. 2.4: After the inverse Fourier Transform the magnitude of the complex result is used to generate the morphological images.

The combination of the RF-pulses, the gradient coils and the readout is called an MR pulse sequence. In the present thesis, the 2D GRE sequence is utilized. Using a 2D-GRE, the flip angles chosen are less than 90° allowing for smaller T_R and therefore reducing the imaging time. In addition, the sequence uses additional gradients before every RF-pulse to dephase the left over transversal magnetization (Reiser et al., 2007). An example pulse diagram of a GRE sequence can be seen in Figure 2.5.

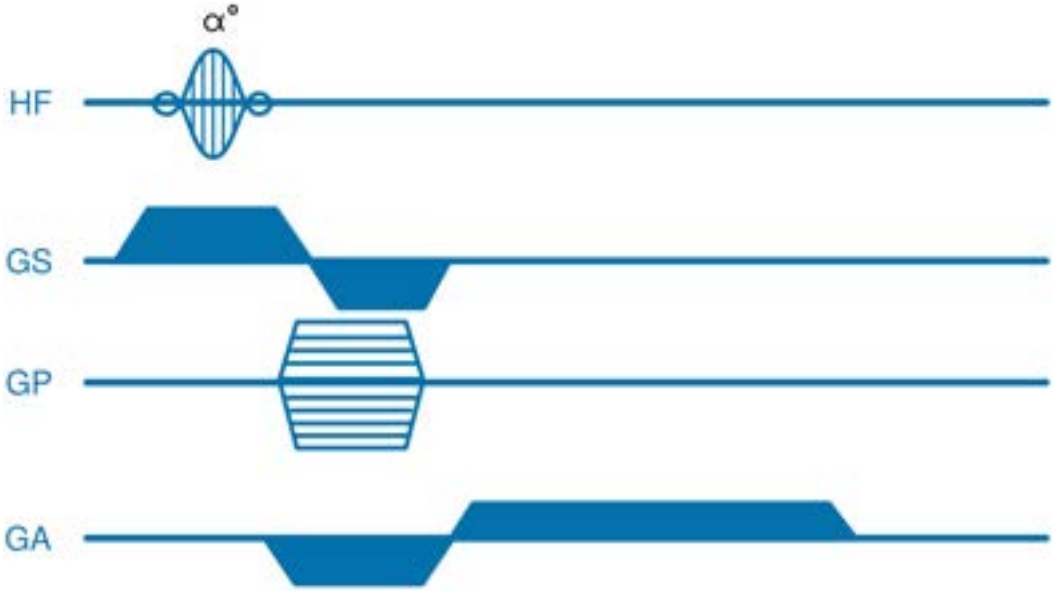

Fig. 2.5: An example pulse diagram for a GRE sequence using a flip angle α <90°. G_S = Slice-selective gradient. G_P = Phase gradient. G_A = Readout gradient. Based on (Reiser et al., 2007).

2.2 MR Thermometry

The MR device as explained in the previous section is not only used for interventional imaging but can also be utilized for measurement of the temperature inside the tissue. Because the clinical case of application focused on in this thesis are thermal ablation procedures, the following section will explain the basic principles of the MR thermometry. Here, the most commonly used technique is the PRFS thermometry introduced by Porter et al. (1995; 1995) and Ishihara et al. (1995). The PRFS method is able to achieve good spatial and temporal resolution with respect to real-time compatibility.

The resonance frequency of a nucleus is determined by the local magnetic field B_{loc} and can be computed by:

$$B_{loc} = (1 - \sigma) * B_0 \tag{2.5}$$

with σ representing the screening constant for each nucleus dependent on the chemical environment (Rieke et al., 2008). In the human body, every hydrogen nucleus is bound as a water molecule (H_20) and the nuclei are permanently screened by the electrons of the macroscopic field. These water molecules bond with each other creating an inter-molecular hydrogen bridge bond (HBB). As soon as an HBBis created, the screening of these nuclei is reduced; whereas, free water molecules show a higher screening. By applying temperature to the tissue (e.g., during thermal ablation), the HBBs are damaged. As a result, σ is increasing (Rieke et al., 2008). For temperatures in the range of -15°C up to 100°C, the screening constant increases linearly with the temperature T by the temperature-dependent chemical shift coefficient α (Rieke et al., 2008):

$$\begin{aligned} \sigma(T) &= \alpha * T \\ \alpha &= \frac{1 * 10^{-8}}{^\circ C} = 0.01 \frac{ppm}{^\circ C} \end{aligned} \tag{2.6}$$

In summary, the application of heat inside the tissue leads to an increase in screening efficiency; therefore, a decreasing of the local magnetic field and as a result also decreases the proton resonance frequency. These properties can be exploited to create thermometry maps for the monitoring of thermal procedures. Next to spectroscopic imaging, phase mapping has evolved as one of the possible methods. Phase images can be acquired, for example, by GRE imaging sequences. Due to the change in resonance frequency caused by the heating of the tissue, the resulting phase also changes. By computing the phase difference between two time points, a phase shift can be observed. To reduce temperature-independent confounding factors, several reference images prior to the treatment can be acquired and averaged (Rieke et al., 2008; Blackwell et al., 2022). Taking into account the physical properties and parameters of the MR device as well as the phase images at different time points, the total temperature T can be computed as:

$$T = \frac{\phi(t) - \phi(t_0)}{2\pi\gamma\alpha B_0 T_E} + T_0 \tag{2.7}$$

with $\phi(t) - \phi(t_0)$ defining the phase difference between the current time point $\phi(t)$ and the reference time point $\phi(t_0)$, $\gamma = 42,576 \frac{MHz}{T}$ representing the gyromagnetic ratio of hydrogen protons, $\alpha = 0.01 \frac{ppm}{\Delta T}$ representing the proton resonance frequency change coefficient, B_0 representing the used magnetic field strength and T_E repre-

senting the used echo time. The constant T_0 needs to be added to the temperature because Equation 2.7 otherwise only computes the temperature change, neglecting the tissue's base temperature. In addition, every image acquired is a trade-off between computational time and resolution (mainly the SNR). To achieve an optimal SNR, the T_E should be defined close to T_2^* (Rieke et al., 2008). Another factor to consider is the phase drift. El-Sharkawy et al. (2006) described the phase drift as a continuous change of the main magnetic field B_0 with 0,8 to 2,5 ppm. This spatial and temporal change of the magnetic field influences the phase measured by the MR device and therefore altering the results of the thermometry computation. Several approaches for phase drift correction have been introduced in the past using reference materials or non-heated areas in the images themselves (El-Sharkawy et al., 2006; Poorter, 1995).

In the present thesis the heat maps are transferred into necrosis maps by using the critical temperature model. In order to reduce the computational bias, the phase drift of around 2°C is considered during computation of the necrosis map by adapting the necessary threshold applied for the final reconstruction.

2.3 Minimally invasive Thermal Ablation: Microwave Ablation

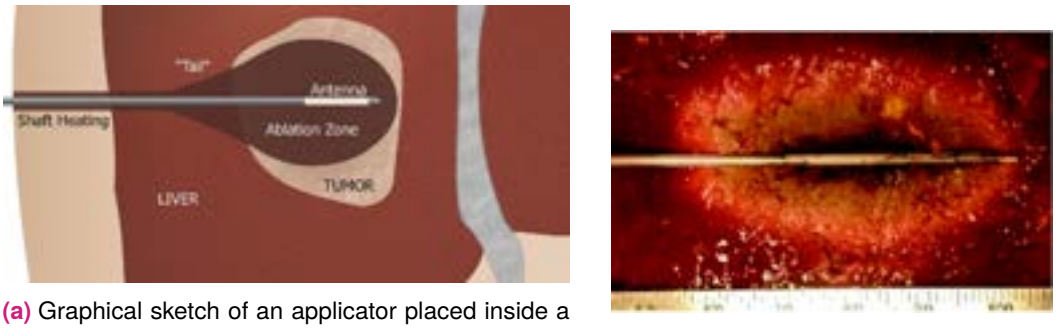

(a) Graphical sketch of an applicator placed inside a tumor in the liver.

(b) Real coagulation necrosis after MWA.

Fig. 2.6: During thermal ablation the heat is induced through the electrode in the tip creating the characteristic ellipsoid coagulation shape including the "tail" around the shaft. Images taken from (Lubner et al., 2010).

The interventional procedure in focus of the present thesis is the MWA. In contrast to other procedures like RF ablation, MWA offers several potential benefits like higher intratumoral temperatures, larger tumor ablation volumes, faster ablation times, the ability to use multiple applicators, and less procedural pain (Simon et al., 2005).

Especially, the ability to reach temperatures above 100°C allows for treatment of malignant tissues in areas with high water content. In addition, MWA seems to be more robust towards heat sink effects, which leads to bigger necrosis sizes on average (Lloyd et al., 2011). On the other side, the higher temperatures also cause the shaft of the applicator to heat up causing a "heat tail" along the shaft as illustrated in Figure 2.6a. This phenomenon and the overall faster heating of the tissue is hard to control when aiming for bigger necrotic areas (Poulou et al., 2015). To address the issue of the heat tail, MWA systems usually integrate a shaft cooling approach (Lubner et al., 2010).

The physical principle which the MWA is based on is called dielectric hysteresis. By applying a rapidly alternating electromagnetic field (2-3 billion times per second), the water molecules inside the tissue try to realign with the magnetic field. If the alternation is too fast, the remaining energy will be converted into heat instead of kinetic energy (Figure 2.7). The final rate of heat generation (Q_h) is computed using Equation 2.8:

$$Q_h = k * |E|^2 \tag{2.8}$$

with E representing the applied electric field magnitude and k the effective conductivity as a measure of microwave absorption (Bray et al., 2018).

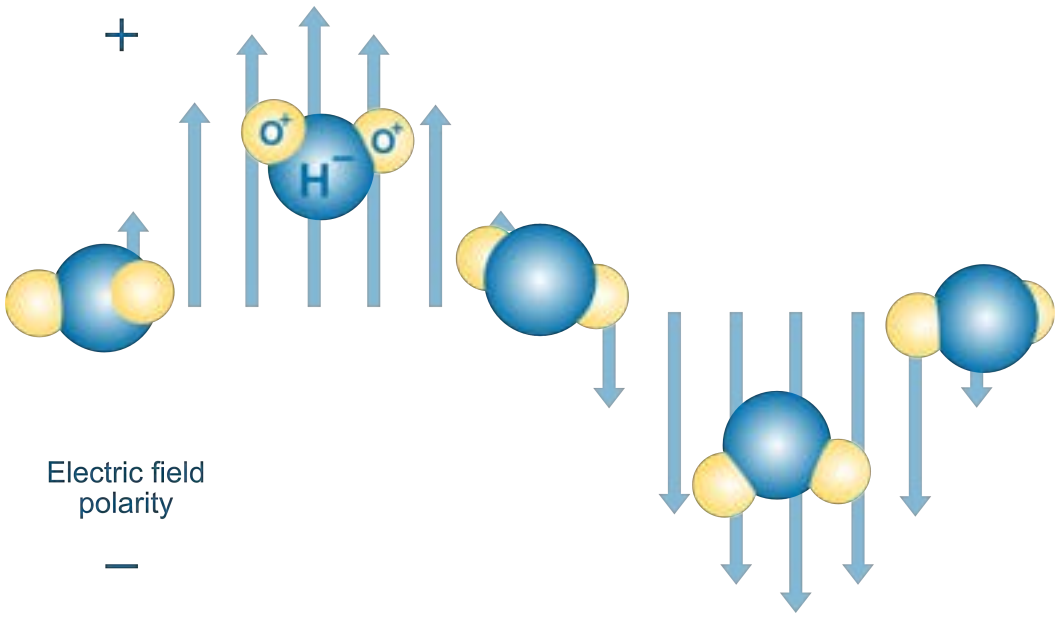

Fig. 2.7: Illustration of water molecules realigning with the alternating electromagnetic field. Based on (Christopher L Brace, 2009).

An MWA system consists of three main components: a generator, a power distribution system and an applicator (in the literature also referred to as antenna). The generator defines the power source of the system using frequencies of 915MHz up to 2.45GHz as allowed by the Federal Communications Commission. The distribution of this created energy is done through a coaxial transmission line. The most critical part in a MWA system is the applicator because the heat transfer to the tissue highly depends on its geometry. Therefore, most applicator designs are straight and needle like using a shaft cooling system to reduce the heat around the skin and prevent injuries like skin burn. An illustration of a placed applicator can be seen in Figure 2.6a. The actual size and shape of the coagulation necrosis highly depends on several factor like the applicator design, the tissue type, the thermal conduction or thermal heat sinks caused by vessels and other cooling structures (Lubner et al., 2010). A real coagulation necrosis can be seen in Figure 2.6b.

2.4 Minimally invasive Thermal Ablation: Current Workflow

The workflow procedures used for minimally invasive thermal ablation vary depending on the hospital and the performing radiologist. Nonetheless, some key steps are universally applicable. The following workflow description is based on the clinical procedure at the Hannover Medical School (MHH) and the University Hospital Magdeburg (UMD). The information presented was acquired during clinical visits, observations and discussion with the performing radiologists. In addition, Kaye et al. (2015) performed a review on closed-bore interventional MRI for percutaneous biopsies and thermal procedures. Their findings support the observations regarding the key steps during the procedures, which can be divided in a non-sterile and a sterile part. A summary of the derived state-of-the-art workflow for a procedures with general anesthesia can be seen in Figure 2.8. The key steps necessary to perform the intervention are briefly explained in the following starting with the non-sterile part of the intervention:

1. **Admit Patient**

   The very first step is the admittance to the hospital. Here, the preoperative discussion with the patient takes place. In addition, blood from the patient is drawn and analyzed regarding coagulation values and kidney values. If everything is in place and confirmed, the patient is prepared for the intervention.

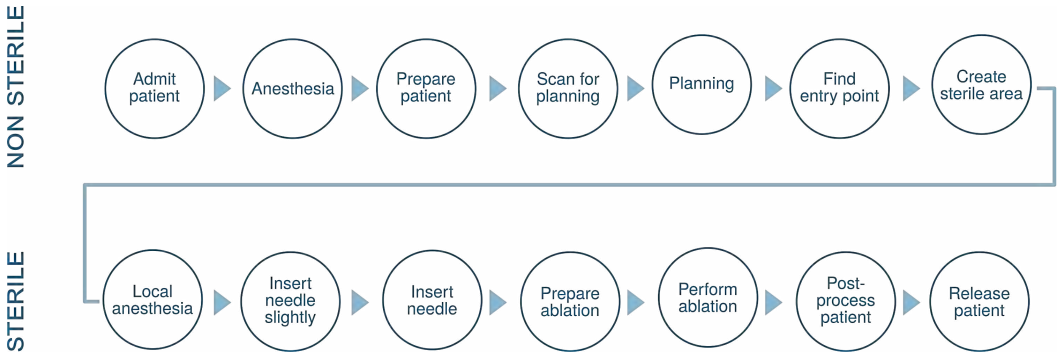

Fig. 2.8: Summary of the workflow derived from the MHH and UMD workflow. The different key steps are divided into non-sterile and sterile activities.

2. **General Anesthesia**

   The patient is put under general anesthesia before the preparation of the patient.

3. **Prepare Patient for MRI**

   The patient is checked for any metal objects, which may be attracted by the magnetic field causing harm to the patient or the staff. After that the patient is positioned on the table and fixated to reduce involuntary movement. The last step during patient preparation is the positioning of additional coils (e.g., a flex coil) on the patient to increase the signal strength and therefore contrast of the images.

4. **Scan for Planning**

   The patient is moved inside the MR bore and the localizer is used for checking the flex coil position. Afterwards, a 3D planning image is acquired. Note that usually the ventilation of the patient is stopped for every 3D volume acquisition.

5. **Planning the Procedure**

   During the planning of the procedure, the area of interest is defined by the performing radiologist. This also includes the definition of the entry and target points for used medical instrument (e.g., applicator for thermal ablation). When the trajectory of the used medical instrument has been defined, the medical technical assistant usually aligns the interventional MR sequence used during the procedure to the planned trajectory. The interventional sequence is then run to see if the target structure, in this case the malignant tissue, is visible.

6. **Find Entry Point**

   One of the most common approaches for finding the correct entry point is the "Finger-Tipping" - method. Here, the previously prepared interventional sequence is used, and the performing radiologist moves a finger across the patient's body until it appears in the live image data. When the finger is visible in the acquired images, it stays at the position while the patient is being moved out of the bore to mark the entry point with a bio-compatible ink marker. Example images during the Finger-Tipping can be seen in Figure 2.9.

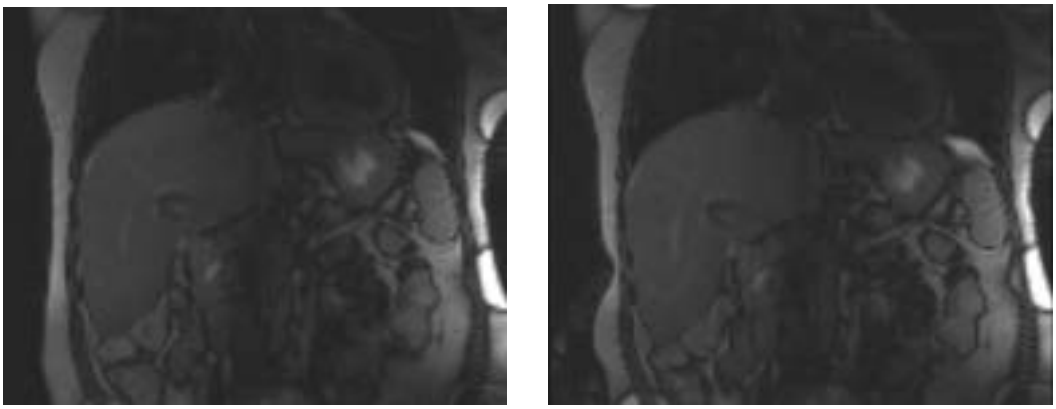

(a) No finger visible in the image. **(b)** Finger visible in the image.

Fig. 2.9: The Finger-Tipping method is a widely used technique to find the entry point during MR-guided needle-based interventions. The images shown are provided by the MHH and show a characteristic image with and without the finder visible.

7. **Create Sterile Area**

   The last step during the non-sterile part of the intervention is the sterilization of the patient and the used environment. First, the area of intervention is cleaned and sterilized. After that, the drapes are placed on top of the patient, with the interventional access point placed above the area of interest. Lastly, the performing radiologist is prepared for the upcoming intervention

After preparation and sterilization of the performing radiologist, the following steps are performed in a sterile environment. Every contamination of either the radiologist or the area of interest will result in a repetition of the sterilization process and may cause harm to the patient due to longer intervention times. The following steps cover the sterile process of the intervention:

1. **Local Anesthesia**

Even when placed under general anesthesia, a local anesthesia is applied through the marked entry point in order to reduce the deep tissue pain during and after the intervention.

2. **Insert Applicator Slightly**

   The patient's skin is cut open at the marked entry point using a scalpel. The applicator is inserted into the tissue for around 2-3cm with an assumed angulation and orientation. The patient table is moved into the bore while holding the applicator in place and the position and orientation is verified using the previously prepared interventional imaging sequence.

3. **Insert Applicator Completely**

   Complete insertion of the applicator is performed inside the bore and by utilizing live image data. Here, the position of the applicator is constantly monitored and adjusted based on the images provided and the experience of the performing radiologist. Example images during insertion can be seen in Figure 2.10.

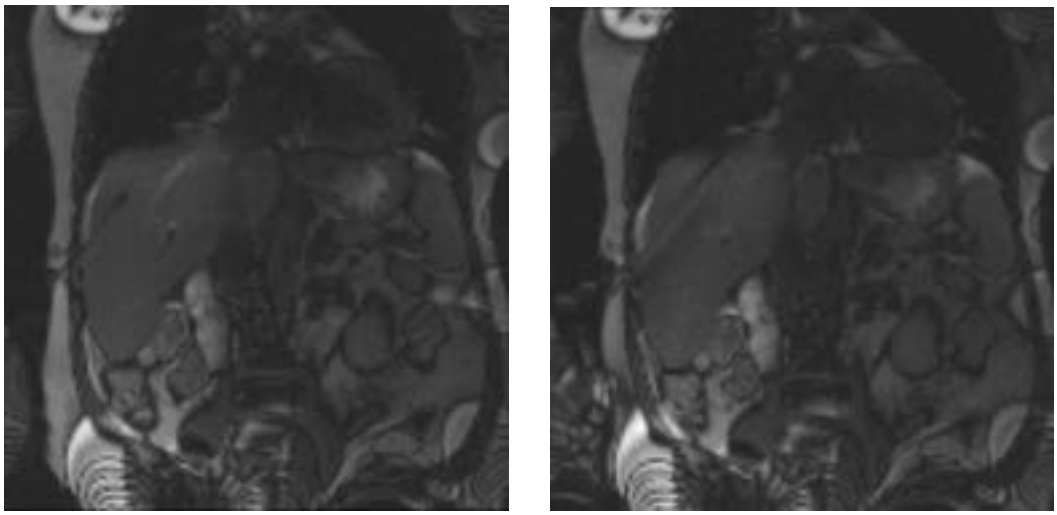

(a) Applicator inserted half way. **(b)** Applicator has reached the target position.

Fig. 2.10: During insertion of the applicator the position and orientation is verified using MR images. The applicator is visible as a black hole inside the image data. The presented examples are acquired during thermal ablation inside the liver and provided by the MHH.

4. **Control needle position**

   After insertion, the position of the applicator is verified using a 3D image sequence. If the position can be verified in 3D space, the thermal ablation will

be prepared. Otherwise, the applicator has to be removed to a certain degree and the orientation has to be corrected.

5. **Prepare Ablation**

   If a monitoring is used during the thermal ablation procedure, it is planned by preparation of a thermometry sequence. In the present thesis, a 2D GRE sequence is utilized. This sequence is placed in a way that it intersects with the applicator in the images, showing the increase of temperature around the electrode in the tip of the applicator.

6. **Perform Ablation**

   To perform the thermal ablation, the patient is moved outside the bore again. The applicator is connected to the generator and the patient is moved back into the bore. Usually, the cables involved need to be held during the movement and afterwards fixed somehow so that their weight does not alter the position of the applicator inside the patient. If everything is fixed, the thermal ablation starts. In the case that no holding device is used, the performing radiologist has to make sure that the applicator stays in position.

7. **Post-process patient**

   After the intervention the generator is turned off and the applicator is disconnected. A 3D volume is acquired to confirm the created coagulation necrosis inside the images and decide if the intervention has to be repeated. If that is not the case, the applicator is connected to the generator again and it is turned on. During removal of the applicator, the insertion canal is atrophied by the applied heat and the risk for residual malignant cells is reduced. A final 3D volume is acquired to check for inner bleeding. If everything is confirmed to be acceptable the patient table is moved outside of the bore and the equipment is removed.

8. **Release patient**

   Before releasing the patient, a final confirmation check is made. This can be, for example, an ultrasound scan after 3 hours to verify that no internal bleeding is present. Finally, the patient is released from the hospital.

The present thesis focuses on step number six in the sterile part of the intervention. During the performance of the intervention, a proper monitoring of the heat distribution is necessary in order to ensure a successful treatment of the malignant tissue. The following chapters will describe a method for 2D to 3D reconstruction of

thermometry maps by utilizing a 2D GRE sequence rotated around the applicator's main axis. The resulting volumetric thermometry approach is then evaluated with respect to similarity measurements to test the suitability for the clinical routine.

3

2.5D Thermometry Reconstruction

About this chapter

Parts of this chapter have been published in: Julian Alpers, Daniel L. Reimert, Maximilian Rötzer, Thomas Gerlach, Marcel Gutberlet, Frank Wacker, Bennet Hensen, and Christian Hansen (2021). “2.5 D Thermometry Maps for MR guided Tumor Ablation”. In: Proceedings of International Conference on Medical Image Computing and Computer Assisted Interventions (MICCAI), Strasbourg, France. Significant medical input was provided by Dr. Bennet Hensen. The experiments were conducted at the Clinical Research Center Hannover by Daniel L. Reimert.

3.1 Introduction

> *Life is really simple, but we insist on making it complicated.*
>
> — **Confucius**
> Chinese philosopher

Malignant tumor treatment using mild hyperthermia in combination with chemotherapy and/or radiotherapy has become a widely spread approach. Here, the temperature is ideally limited to 40°C - 43°C for 30 to 60 minutes to reduce the damaging of adjacent tissue (Feddersen et al., 2020). In addition to mild hyperthermia, thermal tumor ablation has also become a promising alternative to open surgery. Here, the heat is increased to over 55°C until coagulation of the tissue is introduced. This causes the cells to be irreversibly destroyed (Ahmed et al., 2014; Mauri et al., 2017; Tomasian et al., 2018). Regardless of the chosen method of treatment, monitoring of the heat distribution is an urgent clinical need. Up to this date, MR thermometry based on the PRFS is the only clinically accepted procedure to monitor the heat distribution during thermal interventions under MR guidance (Kokuryo et al., 2020). In the recent years, many studies have focused on multi-slice 2D approaches instead of full 3D thermometry acquisition due to the limited acquisition time during intervention. This trade-off between computational efficiency and resolution often results in the acquisition of less slices leaving several slice gaps. On the other hand, real-time capabilities must be ensured to create clinical acceptability during interventional procedures e.g., through computational acceleration of the used MR imaging sequences (R. Jiang et al., 2020).

In this chapter, a novel approach for the creation of a volumetric thermometry map without the development of a fully 3D sequence is presented. The introduced 2.5D thermometry method utilizes any common 2D GRE sequence. Therefore, possible temporal limitations are less restricting than for the 3D sequences and images with higher resolution may be acquired offering thermometry accuracy of around 1°C deviation while being more robust towards MR inhomogeneities (Gorny et al., 2019). The described method is well-suited to reconstruct the actual coagulation necrosis after thermal ablation.

3.2 Related Work - Volumetric Thermometry Imaging

The major novelty in the present chapter is the definition of a sequence protocol, which allows the implementation of basic 2D to 3D image reconstruction algorithms. To get a proper overview of the existing protocols and possibilities an initial unstructured literature research was conducted. Based on the results, frequently used phrases and synonyms where identified and collected to define a proper search term. Regarding the topic of volumetric thermometry, the term was divided into three major categories, also observable in Table 3.1:

1. The dimensionality of the thermometry data should be restricted to volumetric approaches. Many approaches exist in the field of pure 2D thermometry. Because the focus of the present thesis lies on the creation of a volumetric map, these 2D approaches are neglected. Included are full 3D sequences or stack of 2D sequences.
2. Any kind of heat map is interesting for the present thesis.
3. Even though other approaches like US thermometry exist, the present thesis only focuses on the use of MR guidance during minimally invasive radiology.

Tab. 3.1: Synonyms regarding the three categories "Dimensionality", "Type of map" and "imaging system". All synonyms were identified during the initial, unstructured literature research.

Synonym	Dimensionality	Type of map	Imaging system
1	3D	heat	MR
2	volumetric	heat map	MRI
3	volume	heatmap	Magnetic Resonance
4	three dimensional	thermometry	Magnetic Resonance Imaging
5	3 dimensional	heat distribution	—
6	three-dimensional	—	—

After definition of the presented categories a structured literature research was performed for the last ten years from 01.01.2012 to 31.07.2022 on PubMed. Connecting the columns in Table 3.1 with logical AND operations and including the date range the following search term was created:

((3D[Title/Abstract] OR volumetric[Title/Abstract] OR volume[Title/Abstract] OR three dimensional[Title/Abstract] OR 3 dimensional[Title/Abstract] OR three-dimensional[Title/Abstract])

AND

(heat[Title/Abstract] OR heat map[Title/Abstract] OR heatmap[Title/Abstract] OR thermometry[Title/Abstract] OR heat distribution[Title/Abstract])

AND

(MR[Title/Abstract] OR MRI[Title/Abstract] OR Magnetic Resonance[Title/Abstract] OR Magnetic Resonance Imaging[Title/Abstract])

AND

(2012/1/1:2022/7/31[pdat]))

This search term yields 343 results, which are analysed in a first title/abstract research. Considered for a more detailed analysis where 87 papers dealing with the topic of thermometry assuming they are not purely focused on 2D approaches. Those papers were analysed in more detail performing a full paper research. All papers describing volumetric thermometry approaches where included resulting in 22 relevant papers for the last ten years. In the last step, additional relevant papers not appearing in the search term but already known by the author of the present thesis where included in this chapter.

The results of the literature research can be mainly clustered in the categories "Full 3D Thermometry" and "Stack of 2D Thermometry". The former describes volumetric MR sequence approaches, whereas the latter describes a special arrangement of single 2D image slices sub-sampling the volume of interest (VOI).

A detailed analysis of the related work can be observed in Tables 3.2 and 3.3. In addition, Kokuryo et al. (2020) describe the clinical applicability of thermometry approaches also including a very brief description of volumetric approaches.

3.2.1 Full 3D Thermometry

The field of full 3D thermometry acquisition covers the part of the related work, which is focusing on the development of real 3D MR thermometry sequences. Here, the field of view (FOV) is three-dimensional without gaps between the adjacent image slices. In the following, the different approaches are briefly described and analysed regarding their general approach, acquisition time, resolution, volume coverage (FOV) and temperature accuracy. The related work is sorted according to the year of publication in ascending order.

Kickhefel et al. (2012) addressed the problem of susceptibility artifacts during cryoablation. The artifacts were corrected in a post-processing step, using a rapid numerical algorithm. For temperature measurements repetitive MR image acquisitions were performed using a 3D FLASH GRE sequence with twelve adjacent coronal slices covering an area of 300x300x24mm^2 in 57.8 seconds. The whole post-processing pipeline is set up on-line. Todd et al. (2014) introduced an approach called temporally constrained reconstruction to solve the problem of obtaining large coverage 3D temperature measurements. Their extended approach only uses acquired k-space data up to the current time and utilizes a GPU architecture to achieve real-time capabilities. Odeén et al. (2014) developed a 3D GRE pulse sequence using a segmented echo planar imaging (EPI) readout. Acquisition time of the raw data for the whole volume was roughly four seconds but image reconstruction was performed offline using MATLAB in 803 seconds for 250 iterations of their TCR algorithm. Two years later Odeén et al. (2016) introduced a US modeling combined with a hybrid angular spectrum method to obtain the US power deposition required for a model predictive filtering method to compute the heat distribution for MR guided interventions. Dharmadhikari et al. (2016) introduced a new 3D GRE sequence tested on a phantom study. They performed all data processing offline using MATLAB resulting in a very high resolution of 0.5mm isotropic voxels but a small volume coverage of 32x32x64mm^3. Overduin et al. (2016) assessed the feasibility and accuracy of a 3D ultrashort echo time MR thermometry. The sequence itself was provided by Siemens Healthineers as a work-in-progress package for Cryoablations. To compare the results of the thermometry three fiber optic temperature sensors were inserted into the tissue. Svedin et al. (2016) describe a 3D segmented EPI GRE sequence in combination with the PRFS method to obtain the thermometry maps. In addition, they explain a way for respiratory motion compensation by introducing a phase navigator inserted into the EPI before and after the readout to monitor the B_0 field variations. Their experiments consist of volunteer breast images without heating to verify the motion compensation algorithm and phantom experiments with a breathing person lying underneath the phantom to simulate the respiratory motion. Later, Svedin et al. (2018) also presented a multi-echo stack-of-stars sequence for MR thermometry. They combine the sequence with a pseudo-golden angle sampling and k-space weighted image contrast. This allows for simultaneous acquisition of multiple quantitative measurements for PRFS temperatures. Fielden et al. (2018) developed a 3D spiral MR thermometry sequence based on the retraced spiral-in/out trajectory and implemented it on a real-time platform for evaluation in an in vivo porcine model. Bever et al. (2018) introduced an in-house build single-channel RF coil for their experiments. Using a 3D GRE segmented multi-shot EPI sequence with 12 slices acquired. They evaluated their sequence using a total of five different

experiments including two phantom studies and three ex vivo porcine brains. They were able to achieve a high temperature accuracy of $\pm 0.3°C$ but report a image acquisition of around 20 seconds. Zhang et al. (2019) propose a a variable flip angle golden-angle ordered 3D stack-of-radial sequence for simultaneous T1-based temperature mapping using the PRFS method. Jeong et al. (2021) use a multi echo GRE sequence during a 21 minute ablation cycle. With an acquisition time of 41 seconds they were able to achieve 30 image repetitions during the intervention with a volume coverage of a solid 300x300x300mm^3.

Tab. 3.2: Overview of the related work on different approaches to create a volumetric heat map using a full 3D sequence approach. The table is sorted with respect to the year of publication starting in ascending order. The duplicate entry for Odeén et al. (2014) results from two different experiments described (phantom and lamb). Underlined entries did not appear in the structured literature research.

Author	Acq. Time [s]	Resolution [mm]	Coverage [mm]	Temp. [°C]
(Kickhefel et al., 2012)	57.8	1.56x1.56x2	300x300x24	±0.35
(Odéen et al., 2014)	3.3	1.2x1.2x2.5	192×192×110	—
(Odéen et al., 2014)	4.32	1.0x1.0x2.0	192x144x60	—
(Todd et al., 2014)	1.2	1.5x1.5x3.0	192x162x66	±0.5
(Dharmadhikari et al., 2016)	—	0.5x0.5x0.5	32x32x64	—
(Overduin et al., 2016)	74	1.62x1.62x1.62	260x260x260	-1.2± 2.7
(Odéen et al., 2016)	2.4	2.3x2.3x2.5	288x221x135	<1.1
(Svedin et al., 2016)	10.3	1x1x3	224x154x24	0.45±0.32
(Svedin et al., 2018)	<3	1.3x1.3x1.3	208x208x41.6	0.3-1.0
(Fielden et al., 2018)	2.9-3.3	0.4x0.4x0.4	224x224x224	1.3
(J. T. d. Bever et al., 2018)	19.4-20.3	1.25x1.25x3.0	160x114x36	±0.3
(L. Zhang et al., 2019)	2-5	1.17x1.17x5.0	300x300x160	<2
(Q. Chen et al., 2020)	3.3	2.0x2.0x5.0	192x192x80	± 0.56
(R. Jiang et al., 2020)	3	2.0x2.0x5.0	192x192x80	0.37-0.45
(Jeong et al., 2021)	41	4.7x4.7x10	300x300x300	—

3.2.2 Stack of 2D Thermometry

The second cluster for volumetric thermometry approaches can be described as a stack of 2D approach. The described image sequences do not cover the full VOI but single slices. Here, the FOV is mainly two-dimensional with moderate gaps between the adjacent image slices. In the following, the different approaches are

briefly described and analysed regarding their general approach, acquisition time, resolution, volume coverage (FOV) and temperature accuracy. The related work is sorted according to the year of publication in ascending order.

Köhler et al. (2009) introduce a new volumetric sonification approach for HIFU procedures. Rapid and volumetric temperature mapping is achieved by not only monitoring the target region but also along the beam axis and the near field. Nonetheless, this approach only offers a low sampling of the volumetric ROI and does not reconstruct a full 3D heat map. Reconstruction of the images and the thermal dose is performed online to allow for real-time capability. Petrusca et al. (2014) utilize a GRE EPI sequence with five acquired slices. One axial and one sagittal slice each aligned with the HIFU beam main axis, and three coronal slices with a 10mm gap. Because the MR Host was equipped with a real-time data export facility the images were sent to an online display interface using a fast ethernet connection. Due to the arrangement of the slices and the gap between adjacent slices the VOI was undersampled without any reconstruction of the missing information. Marx et al. (2014) introduced the so-called MASTER sequence for Multiple Adjacent Slice Thermometry with Excitation Refocusing. They tested the new image sequence against a common GRE sequence with three and six slices. In the experiments the gap between the slices was said to be 10mm with a slice thickness of 3mm, which resulted in an undersampling of the VOI. On the other hand, they reported an image acquisition time of only 5 seconds while providing a temperature accuracy of $\pm 0.73^{\circ}$C in vivo and $\pm 0.29^{\circ}$C in a phantom. Tillander et al. (2016) use a multishot RF-spoiled FFE-EPI sequence with a total of six differently aligned slices. Three coronal slices and one sagittal slice are placed within the region of interest while two more coronal slices were placed to monitor the near and far field of the HIFU beam. No full volume coverage was reported. Chu et al. (2016) are addressing HIFU hyperthermia using a RF-spoiled fast field-echo EPI sequence. Similar to Tillander et al. (2016) they also arrange six image slices in the region of interest. Three of them perpendicular to the HIFU beam, one sagitall centered at the focus, one across the near field of the beam and one image slice across the beam to monitor sensitive structures. Toupin et al. (2017) use a fat saturated, single-shot EPI combined with GRAPPA acceleration for reconstruction in the field of cardiovascular interventions. With their method they are able to acquire up to five slices at each heartbeat utilizing an ECG trigger. Marx et al. (2017) divide the treatment of lesions using MR guided focused US into three different stages with individually tailored MR protocols: focal spot localization, focal monitoring and background monitoring. To improve the performance during multi-slice acquisition multi-echo spiral thermometry was utilized. Odeén et al. (2019) performed a detailed comparison study of

different 2D and 3D approaches while introducing optimized and new sequences. The focus lies on widely used pulse sequences like Cartesian 2D, 3D GRE and EPI. They were able to demonstrate that their developed volumetric approach was able to acquire twelve slabs in the same time as the conventional 2D sequence while maintaining an equal precision as the 2D approaches.

Tab. 3.3: Overview of the related work on different approaches to create a volumetric heat map using a stack of 2D slices approach. The table is sorted with respect to the year of publication in ascending order. Underlined entries did not appear in the structured literature research.

Author	Acq. Time [s]	Resolution [mm]	Coverage [mm]	Temp. [°C]
(Köhler et al., 2009)	2.9	2.5x2.5x7.0	400x248x21	1.2±0.2
(Petrusca et al., 2014)	4	1.0x1.0x5.0	128x128x30	1.3±0.5
(Marx et al., 2014)	5	1.1x2.2x3.0	280x280x50	±0.73/±0.29
(Tillander et al., 2016)	3.2	2.5x2.5x7	400x400x??	-0.7±0.9
(Chu et al., 2016)	3.2	2.5x2.5x7	??x??x??	0.3±0.5
(Toupin et al., 2017)	—	1.6x1.6x3	180x180x16.5	±1.5
(Marx et al., 2017)	<=5	2.0x2.0x2.0	360x360x360	<0.5
(Odéen et al., 2019)	—	0.94x1.88x??	—	—
(Quah et al., 2020)	11.7	??x??x3.0	—	<1
(Campwala et al., 2021)	10	1.7x2.0x5.0	150x150x25	—
(Landro et al., 2021)	2.9	1.44x1.44x3.0	300x300x24	0.38
This Chapter	1.1	1.0x1.0x5.0	256x256x256	1

Quah et al. (2020) introduce a simultaneous multi-slice temperature imaging for acquisition of volumetric temperature maps combined from several 2D slices. Their approach can be implemented in the current 2D Fourier Transform scans currently used for temperature imaging. Campwala et al. (2021) developed another multi-slice volumetric 2D magnetic resonance thermal imaging method to access the heat distribution during robotically-assisted needle-based therapeutic US. To correlate the measurement volumes with histologically confirmed regions of tissue damage they tested their approach in seven swine and confirmed the temperature accuracy and outcome. De Landro et al. (2021) performed a comparison study between 2D and 3D segmented EPI sequences to test for temperature accuracy evaluated by applying a linear regression and Bland-Altman analysis. According to their reporting 2D segmented EPI is confirmed to be more robust in providing reliable temperature maps. this only applies if a high spatial and temporal resolution is not mandatory. 3D segmented EPI on the other hand show advantages during thermal

procedures due to the higher spatial resolution. VilasBoas-Ribeiro et al. (2022) utilize a double echo GRE sequence in combination with the PRFS method for thermometry reconstruction. Their approach is able to acquire 25 axial slices with a slice thickness of 1mm in around 83 seconds.

3.3 Material and Methods

3.3.1 Data Base Preparation

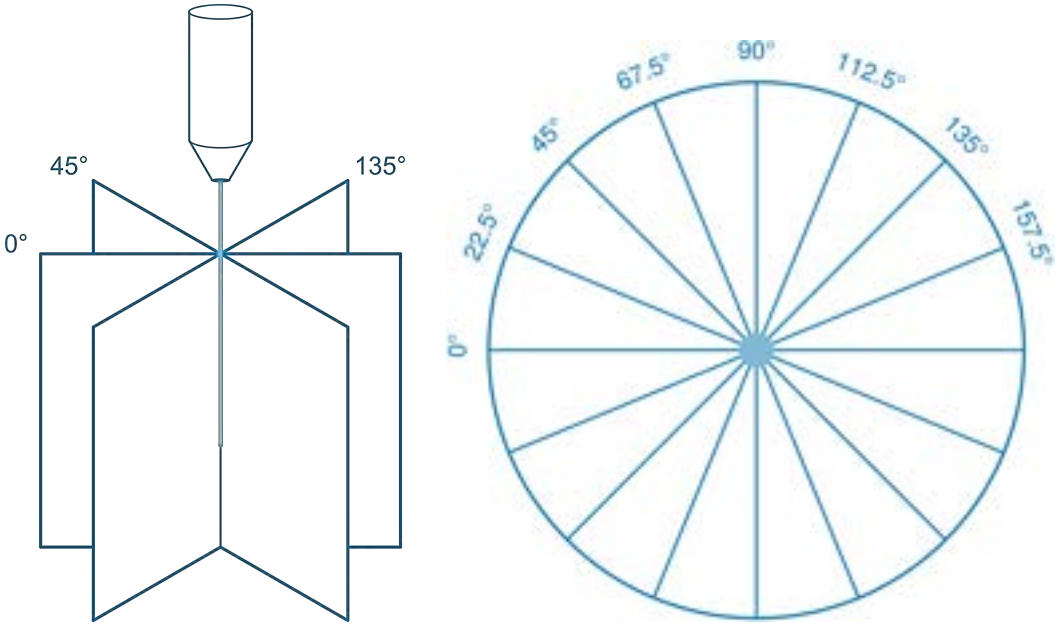

(a) Pictographic representation of the plane rotation around the applicator's main axis.

(b) View through the needle axis to show the arrangement of the individual image planes.

Fig. 3.1: Illustration of the proposed image acquisition protocol. The image plane is rotated around the applicator's main axis by a fixed rotation angle.

The proposed 2.5D thermometry relies on sampling the VOI using a common 2D GRE sequence. The GRE sequence can directly reconstruct magnitude and phase images simultaneously. The phase images are used as an input for the PRFS method afterwards to compute the actual temperature in the images. To ensure a proper sampling of the VOI the GRE sequence is rotated by 22.5° around the applicator's main axis, which results in an evenly distributed sample of eight different image orientations. To increase the spatial resolution, the angles between the acquired scans should be as high as possible, resulting in the following acquisition

order: 0°, 90°, 45°, 135°, 22.5°, 112.5°, 67.5°, and 157.5°. The delay between image acquisition and visualization of the volumetric thermometry map has been reduced by integration of the SIEMENS Healthineers Access-I Framework. The framework allows for fetching the image data directly from SIEMENS MR devices without an intermediate imaging archive system.

After defining the sequence protocol for image plane rotation around the applicator's main axis, ablation procedures where performed in a total of 13 tissue-mimicking bio-protein phantoms as described in the recipe by Bu Lin et al. (2008). To simulate vessels polyvinyl chloride (PVC) tubes were inserted in a subset of the phantoms to create an artificial heat sink effect. An example can be seen in Figure 3.2.

(a) A bio-protein phantom with PVC tubes inserted to simulate the heat sink effect prior to ablation and the same phantom after the ablation. The white opaque coagulation area is clearly visible.

(b) Profile of a homogeneous phantom without PVC tubes after the ablation. For reference the applicator was held in the correct position. The heat tail along the shaft is visible as well as the main coagulation area.

Fig. 3.2: The bio-protein phantoms are prepared in the lab and afterwards used for thermal ablation to create the test data.

The phantom was designed to mimic the physical properties of the human liver and tested in comparison with these specific parameters. Here, the authors of the original paper were able to show that the phantom values differ only slightly from the physical property values of a human liver as summarized in Table 3.4. In addition, it has to be noted that the absolute coagulation temperature of the phantoms differ slightly based on the pH-value. Slight inaccuracies in the dosage of the individual ingredients can lead to deviations of the pH value from the set value of 4.3. Evaluations provided by Bu Lin et al. (2008) show a range of coagulation temperatures based on a pH-value between 4.3 and 4.8 of 50.1°C to 59.5°C, respectively. The applicator of the permittivity feedback control MWA system (MedWaves Avecure, Medwaves, San Diego, CA, USA, 14G) was placed inside the phantom by sight and secured in position. Subsequently, the phantoms were placed inside a 1.5T MR scanner

Tab. 3.4: Difference between the phantom and a human liver regarding the physical properties. The range of the phantom values include variations caused by different pH-values in the range from 4.3 to 4.8. All values reported are based on the research conducted by Bu Lin et al. (2008)

	Density $[kg \cdot m^{-3}]$	**Electrical conductivity** $[S \cdot m^{-1}]$	**Specific heat capacity** $[J \cdot kg^{-1} \cdot^{\circ} C]$
Liver	1.060	0.148	3600
Phantom	[1.066,1.072]	[0.113,0.123]	[3481,3952]

(Siemens Avanto, Siemens Healthineers, Germany). The coaxial cables connected to the applicator and MW generator were led through a waveguide. Chokes and electrical grounding measures were added as described by Gorny et al. (2019) to reduce radio frequency interference. In the case of the perfusion phantoms, the PVC tubes were led through the wave guide. They were connected to a diaphragm pump and a water reservoir outside the scanning room. A flow meter (SM6000, ifm electronic, Essen, Germany) was interposed between the reservoir and the pump, providing a flow rate of 800 $\frac{mL}{min}$. Observations showed a moderate heat sink effect using this setup with a maximum antenna power of 36W. Additionally, temperature sensors were inserted in two phantoms to experimentally verify the temperature accuracy of 1°C. Right before treatment, ten reference phase images were acquired

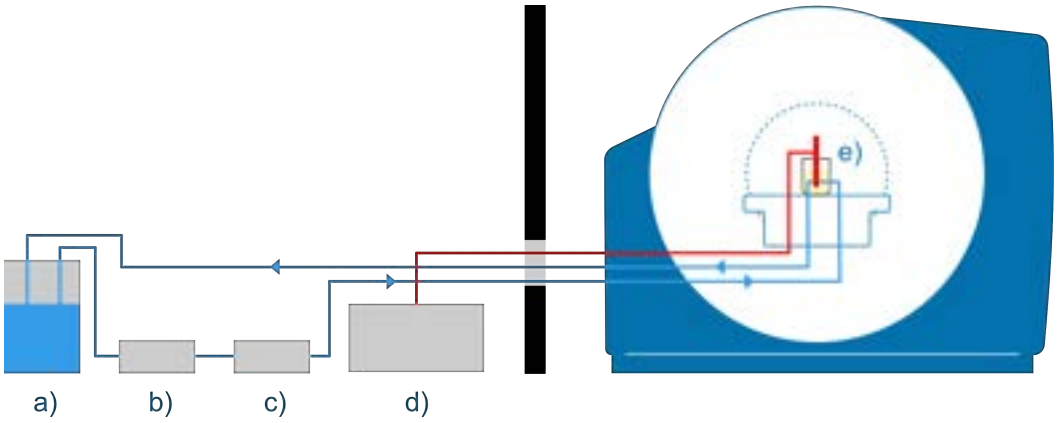

Fig. 3.3: Setup for data base creation. Flexible tubes (blue) lead the water (a) through a flow meter (b), a diaphragm pump (c) and the bio protein phantom (e). The coaxial cables (red) connect the applicator with the MW generator d).

and averaged for each orientation to compensate for static noise. The MWA duration was set to 15 minutes with a temperature limit of 90°C. The GRE sequence offers a slice thickness of 5mm, a FOV of 256mm x 256mm, a matrix of 256 x 256, and a bandwidth of 260 $\frac{Hz}{Px}$. Image acquisition took around 1.1s with a 5s break to simulate the temporal resolution for a breathing patient. The TE was 3.69ms, the TR 7.5ms,

and the flip angle 7°. For post-treatment observation a 3D turbo spin echo (TSE) sequence (TE = 156ms, TR = 11780ms, flip angle = 180°, matrix = 256 x 256, FOV = 256mm x 256mm, bandwidth = 40$\frac{Hz}{Px}$, slice thickness = 1mm) was used. The 3D TSE allows for proper visualization of the real coagulation zone due to a very high tissue contrast. Extraction of the coagulation ground truth was done manually by a clinical expert using MEVIS draw (Fraunhofer MEVIS, Bremen, Germany).

In the present Chapter, a cylindrical container with a diameter of 102.9mm and a filling volume of 1 liter was used. Additionally to the original recipe, the coagulation zone's visibility in the post-treatment MR data sets was increased by adding a contrast agent (0,5$\mu mol/L$ Dotarem) to the phantoms. This was done to aid the clinical experts during manual creation of the ground truth after the experiments. Furthermore, additional PVC tubes with a diameter of 5mm and a wall thickness of 1mm were integrated into six out of 13 phantoms (three single-tubes, three double-tubes) to simulate a possible heat sink effect. All data sets created in the experiments of the presented Chapter are publicly available via `http://open-science.ub.ovgu.de/xmlui/handle/684882692/89` and used for evaluation of all consecutive reconstruction and simulation methods.

3.3.2 Volumetric Heat Map Reconstruction

Before treatment starts, reference phase images are acquired for each of the eight orientations. Afterwards, each newly acquired phase image will start computing the up-to-date 2D thermometry map for the current orientation during the treatment. To do so, the PRFS method is used as described in 2.2. The temperature T based on the PRFS is computed using the following Equation

$$T = \frac{\phi(t) - \phi(t_0)}{\gamma \alpha B_0 TE} + T_0 \tag{3.1}$$

with $\phi(t) - \phi(t_0)$ defining the phase difference between the current time point $\phi(t_i)$ and the reference timepoint $\phi(t_0)$, $\gamma = 42,576\frac{MHz}{T}$ representing the gyromagnetic ratio of hydrogen protons, $\alpha = -0.01\frac{ppm}{\Delta T}$ representing the proton resonance frequency change coefficient, B_0 representing the used magnetic field strength and TE representing the used echo time. The constant T_0 needs to be added to the temperature because Equation 3.1 otherwise only computes the temperature change, neglecting the tissue's base temperature. The Access-I integration and 2D thermometry computation were implemented as modules using MeVisLab 3.4.1 (Ritter et al., 2011). The 2.5D thermometry reconstruction itself was implemented using

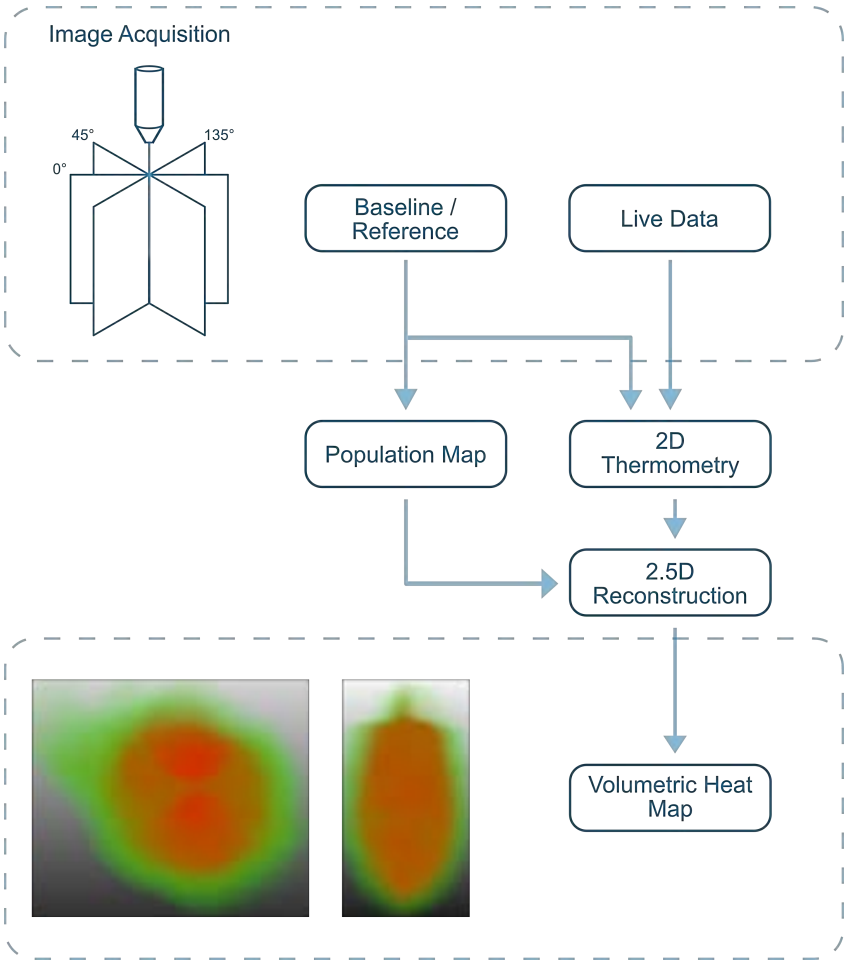

Fig. 3.4: Schematic overview of the proposed method. Based on the phase reference the population map is created. Including the live 2D thermometry data the reconstruction is performed and the volumetric heat map is generated.

C++. A schematic overview of the method can be seen in Figure 3.4. To handle the voxel values during slice rotation every cartesian coordinate was mapped to the corresponding cylindrical coordinate representation using Equation 3.2:

$$
\begin{aligned}
P_r(x, y, z) &= P_c(r, \theta, z) \\
r &= \sqrt{(x - x_c)^2 + (y - y_c)^2} \\
\theta &= atan2\left(\frac{x - x_c}{y - y_c}\right)
\end{aligned}
\tag{3.2}
$$

where x, y represents the Cartesian coordinates of the current voxel and x_c, y_c represents the Cartesian coordinates of the centerline corresponding to the applicator's axis for every slice z in the reconstructed volume. Upon acquisition of the reference images, a multi-dimensional population map is created. For each voxel (x_i, y_i, z_i) in

the reconstructed volume, this population map holds information about the radius r and angle θ of the cylindrical coordinates, the general interpolation weight I_w, the adjacent interpolation partner coordinates $IP_{left}(x, y)$ and $IP_{right}(x, y)$ in the 2D live data as Cartesian representation and the weights w_1 and w_2 of those interpolation partners. The weights may be acquired using Equation 3.3,

$$w_1 = \left| \frac{\theta_{IP_{left}} - \theta_i}{\theta_{IP_{left}} - \theta_{IP_{right}}} \right| \qquad (3.3)$$
$$w_2 = 1 - w_1$$

with θ_i representing the cylindric angle of the current Voxel i and $\theta_{IP_{left}}$, $\theta_{IP_{right}}$ representing the orientation angles of the left and right interpolation partners, respectively.

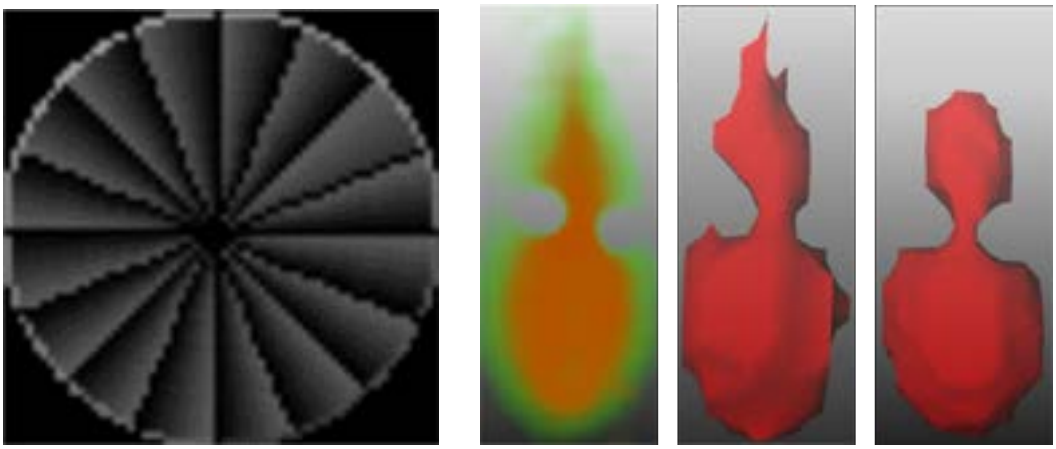

(a) Example population map for output weights color coded on gray scale.

(b) Left: Reconstructed volumetric heat map. Middle: Estimated coagulation necrosis based on a threshold of 57°C. Right: Manually segmented ground truth.

Fig. 3.5: For 2D to 3D reconstruction a population map is created to reduce the computational effort during reconstruction. The reconstructed necrosis map is afterwards compared to the groundtruth regarding DSC similarity.

The 2D population map can be applied to every slice of the final 3D output volume, reducing the computational power needed. During the intervention, every acquired live image triggers the reconstruction of the up-to-date 2.5D thermometry map. Here, the heat value for each voxel is reconstructed using Equation 3.4,

$$T_i = I_w \cdot (w_1 \cdot T_{IP_{left}} + w_2 \cdot T_{IP_{right}}) \qquad (3.4)$$

with T_i representing the temperature of the current voxel i and $T_{IP_{left}}$, $T_{IP_{right}}$ representing the temperature of the adjacent interpolation partners. Occurring

vessels or other structures, which cause a heat sink effect are segmented during the intervention planning. Subsequently, the segmented structure is saved as an additional Look-Up Volume. Here, each voxel can be checked if it is part of a heat sink structure. Using this knowledge, the interpolation weight I_w, which ranges between $[0, 1]$, may be adjusted. Figure 3.5 shows a single dimension of the population map for parameter weighting, a reconstructed heat map, a coagulation estimation based on an empirically defined threshold and the corresponding ground truth segmentation. All source code is available for download at `https://github.com/jalpers/2.5DThermometryReconstruction`.

3.4 Experimental Setup

For evaluation of the 2.5D Thermometry reconstruction method the data sets as specified in Section 3.3.1 were used. All data sets were loaded into the developed software retrospectively and the reconstruction was performed. Afterwards, the results were compared to the manually extracted ground truth.

3.4.1 Statistical evaluation

Final evaluation of the acquired data was performed using the DSC as explained in Equation 3.5

$$DSC = \frac{2 * TP}{2 * TP + FP + FN} \tag{3.5}$$

with TP representing the true positives, FP the false positives and FN the false negatives. Additionally, the standard error of the mean (SEM) was computed at a confidence level of 95% (p = 0.05) using Equation 3.6

$$\begin{aligned} \sigma &= \sqrt{\frac{\sum (x_i - \bar{x})^2}{N - 1}} \\ SEM &= \frac{\sigma}{\sqrt{N}} * 1.96 \end{aligned} \tag{3.6}$$

with σ representing the standard deviation, x_i the current sample, $\bar{x}$ the mean value and N the sample size. To compute the SEM at a confidence level of 95% it has to be multiplied by 1.96, which is the approximated value of the 97.5 percentile of the standard normal distribution.

3.5 Results

Summarized evaluation results can be seen in Figure 3.6. Empirically determined coagulation thresholds were set between 51°C and 61°C depending on each phantom's pH value. It is noticeable that the DSCs for heat sink phantoms show a

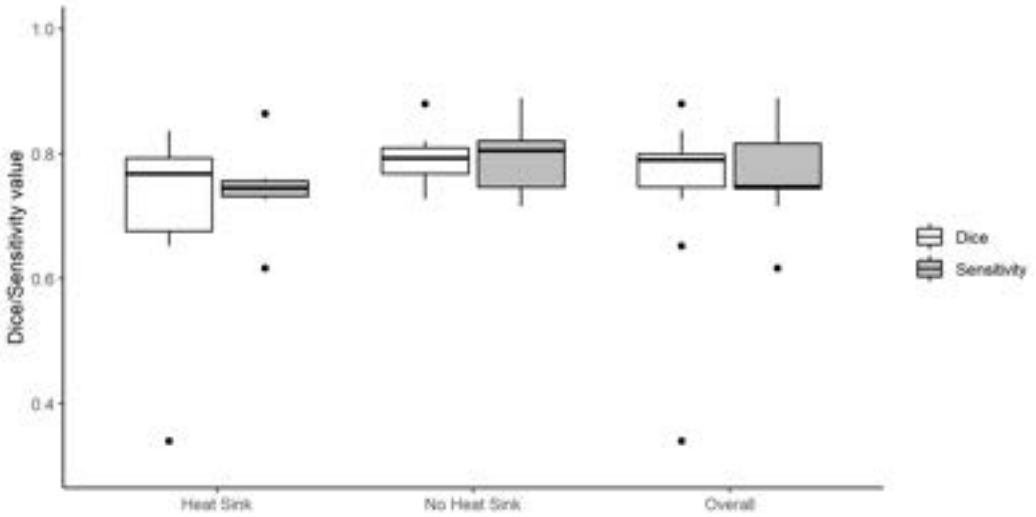

Fig. 3.6: Summarized evaluation results for phantoms without heat sink effect, phantoms with heat sink effect and the overall results. Note that the data range [0,0.3] was left out because no data points are present in that range.

very high SEM with 0.70±0.15 (±21.25%) and 0.74±0.06 (±8.49%) regarding the sensitivity. The high range results from a corrupted data set due to heavy artifacts within the image data.

Leaving the corrupted data set out of the evaluation, the SEM shows a significantly lower deviation of 0.76±0.062 (±8.07%) and 0.77±0.048 (±6.25%) for the DSC and sensitivity, respectively. Observations show a slightly higher DSC and sensitivity for phantoms without any heat sink effect. Here, the values range from 0.79±0.04 (±4.53%) and 0.79±0.04 (±5.55%), respectively. Evaluation showed an overall SEM for the DSC of 0.75±0.07 (±9.76%) and a SEM for sensitivity of 0.77±0.04 (±4.99%). To evaluate the computational effort, every major step was performed 100 times. The creation of the population map and the heat sink look up volume took 25.53ms±3.33ms and 3.91s±0.59s, respectively. These two steps need to be done just once before start of the treatment. The reconstruction of the 2.5D thermometry map was performed in 18.02ms±5.91ms on a customary workstation (Intel(R) Core(TM) i5-6200U CPU, double-core 2.30GHz, 8GB RAM, Intel(R) HD Graphics 520). This reconstruction will be performed every time a new image is acquired during treatment.

3.6 Discussion and Conclusion

The aim of the presented chapter was to develop a volumetric thermometry map, which can be applied to a wide variety of clinical setups. Therefore, this method heavily relies on the up-to-date standard 2D GRE sequence for image acquisition. This allows for an accuracy of the thermometry up to 1.0°C. Nonetheless, the sampling of the 3D volume also results in some disadvantages, which need to be addressed in the future. First, the diffusion of the heat inside the tissue is not linear over time. Therefore, it would be necessary to include an adaptive temporal and spatial resolution depending on the current intervention time. A new study should be conducted to identify an optimal sequence protocol for this 2.5D thermometry approach. Second, it was found that the reconstruction sometimes shows stair-case artifacts. Because only one image is acquired every few seconds, the time difference between adjacent orientations may be very high. The temperature difference for each voxel dependent on the applicator's radius may be computed and applied to the corresponding voxel on every other out-of-date data to compensate for this error. This transfer of the heat gradient may improve the reconstruction accuracy. Another approach may be the use of a model-based reconstruction to take different tissue characteristics into account. To pseudo-increase the temporal resolution, bio heat transfer simulations may also be included during reconstruction. The acquired live data may be able to adjust the simulation parameters to increase the simulation accuracy. Finally, this study only performs on bio protein phantoms. Results show a proof of concept for the proposed method, but it still has to be evaluated in real tissue and a more realistic clinical environment. Therefore, perfused ex vivo livers may be a way to go in the future (D. Becker et al., 2019). Additionally, this work currently assumes a breath-holding state or at least a breath-triggered image acquisition. Research shows that a wide range of interventional registration methods is available (Xue et al., 2011; Dutta et al., 2013; McClelland et al., 2014), but further investigations in this area still need to be done to create an applicable method. The last issues arise because of the MR inhomogeneity during image acquisition. The slightest disturbances may result in heavy image artifacts. Proper shielding of the MW generator is needed to reduce the SNR loss over time thus increasing the thermometry and reconstruction accuracy (Ehses et al., 2021).

Regarding the related work presented in Section 3.2 the proposed sequence protocol can be included in the cluster of stack-of-2D image approaches. Even though, other researchers show a higher temperature accuracy in their approaches the presented method outperforms all other research in terms of resolution and coverage. The stated acquisition time of 1.1 second on the other hand, is only given for

one reconstruction. A full coverage of the VOI requires eight image acquisitions resulting in a total acquisition time of 8.8s without the intermediate breaks for breath-triggered acquisition. Nonetheless, a major advantage of the proposed method is the distribution of the overall image acquisition time over a longer period of time. The presented approach can lead the way for other researchers not familiar with sequence programming to start addressing the complex problems of volumetric thermometry reconstruction.

In conclusion, this chapter proposed a novel method for 2.5D thermometry map reconstruction based on common GRE sequences rotated around the applicator's main axis. A pilot study was conducted using bio protein phantoms to simulate cases with possible heat sink effects and without. The evaluation shows promising results regarding the DSC of the reconstructed 2.5D thermometry map and a manually defined ground truth. Future work should address the reconstruction method's improvement by integrating further apriori knowledge like the estimated shape of the heat distribution. Furthermore, a more realistic study should be conducted with bigger sample size and real tissue. In sum, the method shows a high potential to improve the clinical success rate of minimally invasive ablation procedures without necessarily hampering the standard clinical workflow of the individual clinician.

4 Volumetric Necrosis Map Reconstruction - Comparison Study

About this chapter

Parts of this chapter have been published in: Julian Alpers, Bennet Hensen, Maximilian Rötzer, Daniel L. Reimert, Thomas Gerlach, Ralf Vick, Marcel Gutberlet, Frank Wacker, and Christian Hansen (2022). “Comparison study of reconstruction algorithms for volumetric necrosis maps from 2D multi-slice GRE thermometry images”. In: Scientific reports, 12.1 (2022): 1-12. Significant medical input was provided by Dr. Bennet Hensen. The methods described were implemented by Maximilian Rötzer as part of an university project supervised by the author of this thesis.

4.1 Introduction

> *Simplicity is about subtracting the obvious and adding the meaningful.*
>
> — **John Maeda**
> Chief Technology Officer of Everbridge

From 2018 to 2020, the incidences and deaths caused by cancer increased by 6.47% and 4.21%, respectively (Bray et al., 2018; Sung et al., 2021). Minimally invasive approaches are considered safer than open surgery. In addition, open surgery is not always applicable due to comorbidities, the spread of tumorous lesions or anatomical limitations. A growing alternative is the use of minimally invasive approaches. Along with others, MWA is a promising technique for treating primary and secondary liver lesions with several FDA-certified systems on the market (Ruiter et al., 2019). MWA offers several advantages for the treatment of tumorous lesions, such as fast temperature development within the tissue, fast ablation times, and the ability to use several applicators simultaneously. In addition, MWA tends to reduce patient trauma and to increase the 5-year survival rate of patients with, e.g., hepatocellular carcinoma and liver metastases (Yang et al., 2020). No matter what ablation technique is used, it is of greatest importance to assess if the whole lesion has been destroyed, including the MAM. This MAM was found to be the only important predictor of LTP for liver lesions. Laimer et al. (2020) showed that the chance for LTP was decreased by 30% for each millimeter increase of the MAM. To track the temperature inside the tissue and assess the live coagulation necrosis, MRI thermometry can be performed. Using MRI, the most common approach for thermometry monitoring is the PRFS method using phase mapping (Zhu et al., 2017; Kägebein et al., 2018). In Chapter 3, a novel approach was introduced for the creation of a volumetric thermometry map by utilizing common GRE sequence and performing a simple spatial interpolation. Nonetheless, the approach has disadvantages. This temperature interpolation is prone to errors and anatomical inhomogeneities. Therefore, a priori knowledge about risk structures is necessary. Additionally, the evaluation of bio-protein phantoms raises another bias due to the variable threshold for the coagulation necrosis, based on the pH-value.

In this Chapter, three approaches for reconstruction of a volumetric necrosis map are compared to each other. All algorithms are evaluated on the same data sets introduced in the previous Chapter, including updated thresholds to minimize the bias caused by the phantoms. This Chapter will show that the new approaches are able to exceed the accuracy of the previous reconstruction method while being more

robust towards artifacts and outliers. The goal of the evaluation is the identification of a suitable reconstruction approach with respect to the accuracy, robustness, and the adaptability (necessity of a priori knowledge).

4.2 Related Work - 3D Reconstruction Algorithms

The major novelty in the present chapter is the analysis whether basic image processing algorithms are capable of reconstructing a 3D heat or necrosis map from 2D interventional image data. The focus lies on the differentiation between a full 3D reconstruction and a layer-wise approach based on interpolation and volume stitching. To get a proper overview of the existing methods an initial unstructured literature research was conducted. Based on the results, frequently used phrases and synonyms where identified and collected to define a proper search term. Regarding the topic of volumetric reconstruction, the term was divided into three major categories, also observable in Table 4.1:

1. Again the dimensionality of the reconstruction is meant to be volumetric. Therefore, the search term should yield as few as possible results regarding 2D-2D reconstruction.
2. Basic image processing methods for 2D to 3D reconstruction are of interest for the present Chapter. These include but are not limited to the Delaunay triangulation, splines and enclosing ellipsoids (especially the MVEE approach).
3. To further reduce the amount of medical papers focusing on 3D image acquisition the term "reconstruction" must be present in either the title or the abstract. In combination with Category 2) the resulting set of scientific work is excluding most papers addressing the field of 3D image reconstruction from scanner raw data, which is not of interest for the present thesis.

After definition of the presented categories a structured literature research was performed for the last ten years from 01.01.2012 to 31.07.2022 on PubMed. Connecting the columns in Table 4.1 with logical AND operations and including the date range the following search term was created:

((3D[Title/Abstract] OR volumetric[Title/Abstract] OR volume[Title/Abstract] OR three dimensional[Title/Abstract] OR 3 dimensional[Title/Abstract] OR three-dimensional[Title/Abstract])

AND

(Delaunay[Title/Abstract] OR Delauney[Title/Abstract] OR Spline[Title/Abstract] OR Splines[Title/Abstract] OR Ellipsoid[Title/Abstract] OR MVEE[Title/Abstract])

AND

(Reconstruction[Title/Abstract])

AND

(2012/1/1:2022/7/31[pdat]))

Tab. 4.1: Synonyms for the literature research regarding 2D to 3D reconstruction approaches. The categories can be divided into "Dimensionality", the used "Approach" and "Others".

Synonym	Dimensionality	Approach	Others
1	3D	Delaunay	Reconstruction
2	volumetric	Delauney	—
3	volume	Spline	—
4	three dimensional	Splines	—
5	3 dimensional	Ellipsoid	—
6	three-dimensional	MVEE	—

This search term yields 171 results, which are analysed in a first title/abstract research. Considered for a more detailed analysis where 49 papers dealing with the topic of 2D-3D reconstruction. Those papers were analysed in more detail performing a full paper research. All papers describing a reconstruction of a volume from sparse 2D data or point clouds where included resulting in 12 relevant papers for the last ten years. Exempted from this are papers, which are describing 3D reconstruction approaches from photographs. In the last step, additional relevant papers not appearing in the search term but already known by the author of the present thesis where included in this chapter. The reconstruction methods analyzed include the minimum volume enclosing ellipsoid (MVEE), the Delaunay triangulation and Splines approaches.

Bowyer (1981) and Watson (1981) introduced an incremental 3D Delaunay triangulation. Their initial approach has a time complexity of $O(N^{3/4})$ to $O(N^2)$ and belongs to the serial strategies. Because the efficiency of their introduced method for large data sets is bad other approaches have emerged using parallel strategies. Wan et al. (2015) reconstruct a 3D volume for the left cardiac structure based on multi-planed cardiac MR images. Here, they use a layer-wise interpolation after contour registration from multiple images followed by a Delaunay triangulation for

surface mesh generation. Optimization of the Delaunay triangulation was performed by also applying a graph-cut algorithm. Results show promising DSCs of 0.9 and higher for all data sets. In 2019, Marot et al. (2019) provided a 3D triangulation approach using parallel computation, which is able to reconstruct 55 million tetrahedras in one second. Lately, Su et al. (2020) provided a detailed related work analysis and another approaches for a rapid 3D Delaunay algorithm adapting 3D Hilbert curves and 3D multi-grid division to extend the basic triangulation. Overall, the Delaunay triangulation is said to be suitable for reconstruction of homogeneous structures and convex surfaces.

Regarding the MVEE, Van Aelst et al. (2009) offer a detailed analysis and explanation of the algorithm. They are able to show that the it behaves properly under affine transformation of the data points while providing an efficient convergence rate. In addition, it is shown that the highest break down value lies at around 50%, which is said to be the maximum value for all affine equivariant estimators like the MVEE. Many years later, Abo et al. (2020) on the other hand introduced the use of MVEE for a finite set of points and show that the problem can also be solved by computing the MVEE of a polytope defined by the convex hull. Nonetheless, the literature research does not provide any approach where the MVEE method was used to reconstruct 3D volume data from 2D medical images in any way.

The Bezier splines are an efficient approach to evaluate a spline curve at a given point while being numerically stable. De Boor (1978) also increased the efficiency by introducing the condition that no terms are computed, which are guaranteed to be multiplied by zero. Denk et al. (2004) introduced the splines to perform a myocardial displacement and strain reconstruction using a new cylindrical coordinate B-Spline model, which takes roughly 20s to compute. Galassi et al. (2018) on the other hand reconstruct the 3D coronary artery from 2D X-ray images. They use a non-uniform rational basis splines called NURBS and perform an joint operation on the 2D reconstruction to compute the 3D volume at the end. Zhao et al. (2022) use an enhanced version of the NURBS approach for reconstruction of 3D model shapes from 2D CT angiography data while Reddy et al. (2022) are using cubic spline interpolation to restore the shape of the vocal fold medial surface. Yu et al. (2016) demonstrate a fully automatic reconstruction algorithm for the proximal femur from 2D X-ray images. They provide a 3D template model of the proximal femur and perform a hierarchical two-stage registration. First a rigid 2D to 3D registration is performed followed by regularized deformable B-spline registration. Xiong et al. (2015) are focusing on the reconstruction of the upper airway in the human nostril from MR images. They use a level-set approach to initially segment the structures and create 2D contour lines. The 3D surface is afterwards reconstructed by utilizing

NURBS from axial, sagittal and coronal slices. Fu et al. (2014) reconstruct the 3D representation of the endocardium surface based on sparse point clouds using Thin Plate Splines in combination with progressive approximation of the surface after euclidean-based point matching. Prakosa et al. (2014) introduce a pipeline for reconstruction of patient ventricles from low resolution clinical images. They compare different interpolation methods including splines (DSC = 0.86+-0.06) and harmonics (DSC = 0.87+-0.04). Rim et al. (2013) propose an approach for reconstruction of the arterial geometry based on non-linear cubic spline interpolation. The input data is acquired during intravascular ultrasound imaging.

Regarding the scope of the present thesis three papers can be considered to be closely related to the approaches presented. First, the already mentioned work from Prakosa et al. (2014) is using splines for interpolation of ellipsoidal structures in 2D images. This approach is easily adaptable to the problem of thermometry reconstruction because the cross-sectional plane through the coagulation necrosis perpendicular to the applicator's main axis is also ellipsoidal in shape. Hence, it is suitable to follow the approach from Prakosa et al. (2014) and optimize it for the problem of volumetric thermometry reconstruction. In addition, Faridi et al. (2020) propose a method to reconstruct a volumetric heat map from single 2D temperature maps during mild hyperthermia. Here, they utilize three slices in axial order for the phantom experiments and two axial plus one sagittal slice for their in-vivo experiments. Their approach is based on a compressed sensing algorithm, which is in need of all the afore mentioned orientation during the same time. Due to the sparsely distributed temporal data points of the method proposed in Chapter 3 this approach is not suitable. The last important related work dealing with the reconstruction of volumetric thermometry maps from 2D temperature maps is provided by Seasons et al. (2019). They use a 3D Gaussian fitting model to recreate a volumetric temperature map including necrosis estimation. They compared their approach to a ground truth using the DCS similarity measurement with an average DSC of 0.689. Unfortunately, their approach is only suitable for post-treatment evaluation of lesion. The predicted volumetric necrosis estimation is not meant for intra-operative use.

A summary of the important related work can be seen in Table 4.2. The table show the results analysed by the method used for reconstruction, the area of application, the used data input for the method and if provided the DSC similarity measurement.

Tab. 4.2: Related work regarding 2D to 3D reconstruction methods. The related work is clustered by the different methods and sorted by publication date in ascending order within the different clusters.

Author	Method	Area of Application	Data Input	DSC
Delaunay				
(Wan et al., 2015)	Optimized by graph-cuts	Left cardiac structure	MRI	<0.9
(Marot et al., 2019)	Acceleration by parallel computation	Non medical	Concurrently inserted points	None
(Su et al., 2020)	Adaptive Hilbert curve	Non medical	Randomly distributed point cloud	None
MVEE				
(Van Aelst et al., 2009)	Analysis of original algorithm	Non medical	Affine transformed data points	None
(Abo-Alsabeh et al., 2020)	Computation for polytope of convex hull	Non medical	Finite set of points	None
Splines				
(Rim et al., 2013)	Non-linear cubic splines	Arterial geometry	Intravascular ultrasound	None
(Prakosa et al., 2014)	Splines Surface harmonics	Ventricles	CT (Diffusion tensor) MRI	0.86+-0.06
(Fu et al., 2014)	Thin plate splines	Endocardium	CT Angio	None
(Xiong et al., 2015)	NURBS	Upper airway	MRI	None
(Yu et al., 2016)	B-spline registration	Proximal femur	X-ray	None
(Zhao et al., 2022)	Enhanced NURBS	Liver	CT Angio	None
(Reddy et al., 2022)	Cubic splines	Vocal fold	Video tracked landmark points	None
Others				
(Seasons et al., 2019)	3D Gaussian fitting	Necrosis estimation	MRI	0.689
(Faridi et al., 2020)	Block-based compressed sensing	Mild hypertermia	MRI	None

4.3 Material and Methods

In Chapter 3, a new approach for creating a volumetric heat map was described. Here, a 2D GRE sequence (TE = 3.69ms, TR = 7.5ms, flip angle = 7°, FOV = 256 x 256mm, matrix = 256 x 256, bandwidth = 40$\frac{Hz}{Px}$, slice thickness = 5mm) is utilized by rotating it around the applicator's main axis and reconstructing the missing information. The chosen GRE sequence is inspired by Gorny et al. (2019) who also provide an in depth study about the temporal resolution of GRE sequences during the use of MWA. Therefore, the 13 bio protein phantom data sets offer a temperature accuracy of $\pm 1°$C and each slice was acquired with a resolution of 1.0x1.0x5.0mm in 1.1s. In the following Subsections all tested algorithms are explained in detail. All coagulation necroses were computed using the critical temperature model and a phantom specific threshold between 50°C and 60°C. For rapid prototyping purposes, all three new approaches are implemented in python. The source code can be accessed via https://github.com/jalpers/ScientificReports2022_ComparisonStudy.

4.3.1 Temperature Interpolation

The temperature interpolation method aims at reconstructing the heat map and not the estimated necrosis map. Here, the Cartesian 2D coordinates were mapped to the corresponding polar coordinates. After acquisition of the phase reference images used for the PRFS method to compute the heat map, a population map is created. This population map holds the weights for each interpolation partner for every voxel. The weights are computed using Equation 4.1:

$$w_1 = \left| \frac{\theta_{IP_{left}} - \theta_i}{\theta_{IP_{left}} - \theta_{IP_{right}}} \right| \qquad (4.1)$$
$$w_2 = 1 - w_1$$

with θ_i representing the cylindric angle of the current voxel i and $\theta_{IP_{left}}$, $\theta_{IP_{right}}$ representing the orientation angles of the left and right interpolation partners, respectively. The final interpolation of the temperature is done by applying the population map to every slice along the applicator's main axis using Equation 4.2:

$$T_i = I_w \cdot (w_1 \cdot T_{IP_{left}} + w_2 \cdot T_{IP_{right}}) \qquad (4.2)$$

with T_i representing the temperature of the current voxel i and $T_{IP_{left}}$, $T_{IP_{right}}$ representing the temperature of the adjacent interpolation partners. To reduce

the background noise caused by the air outside of the phantoms, the data sets were cropped to a 60x60mm region of interest (ROI). The morphological opening to reduce the remaining background noise was replaced in this version by a connected component analysis. An example of the method from coronal, axial and sagittal view can be seen in Figure 4.1.

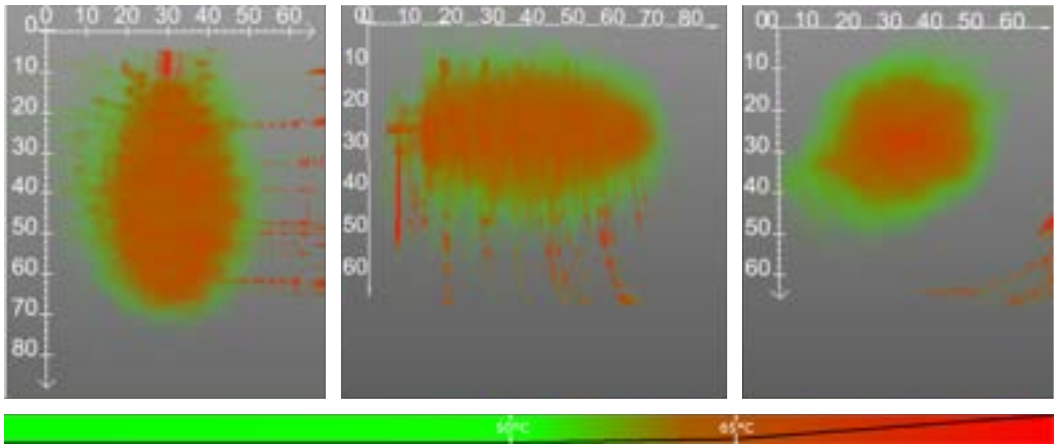

Fig. 4.1: Reconstruction results for the temperature interpolation in axial (left), sagittal (middle) and coronal (right). In addition, the bottom shows the color bar used for the temperature interpolation visualization (0°C - 100°C). The black line indicates the alpha value of the lookup table.

4.3.2 Outlier Detection

For the Delaunay triangulation, the MVEE and the splines method an outlier detection was developed to improve the robustness towards single outlier slices during image acquisition. For this approach the latest acquired image at time point t_i is compared to the previous time point t_{i-1} for that specific orientation with the assumption that the coagulation necrosis is always increasing in size and never shrinking. First, a connected component analysis is performed to remove background noise and small irregularities. Second, the growth of the coagulation necrosis ΔA in percentage is computed and compared between both time points using:

$$\Delta A = \frac{|A_{t_i} - A_{t_{i-1}}| \cdot 100\%}{A_{t_{i-1}}} \tag{4.3}$$

with A representing the area of the coagulation necrosis. If $\Delta A > 80\%$ an abnormal behaviour was detected. This specific value was defined empirically by observation of all phantoms. If a slice is considered an outlier this slice is not taken into account for the current reconstruction.

4.3.3 Delaunay Triangulation

By considering the necrotic voxels as a point cloud, a triangulation can be performed to get an outer hull. This hull features a global and smooth connection of edges resulting in the contour of the estimated coagulation necrosis. In addition, staircase artifacts due to consideration of only single slices are prevented and the polygon mesh is more suitable for post-processing and visualization.

A standardized method for generating a closed surface mesh from a set of points is the Delauny triangulation. It divides an unstructured point set into an uneven triangular grid. To compute the triangulation, the VTK implementation based on the works of Watson (1981) and Bowyer (1981) is utilized. Their algorithm is based on an incremental approach, where one point is added each time to an already valid Delaunay triangulation. Therefore, an initial triangle is placed inside the triangulation, which is big enough to enclose all points of the initial point cloud. These points are now added one after another to the triangulation. Every time this is done, all invalid triangles are identified. For these triangles, the polygonal hole is identified and the triangles are removed from the data structure. After removal, the polygonal hole is re-triangulated and the next point from the input point cloud is inserted in the triangulation. Finally, every triangle was determined whether it contains a vertex, which is part of the initial triangle. If a vertex is found, the corresponding triangle is removed from the triangulation as well. The approach from Watson and Bowyer also introduced a few acceleration steps which caused the algorithm to be faster than the original method. After computation of the modified Delaunay triangulation a convex hull is generated as an output. For creating a volumetric necrosis zone, the voxels within the surface mesh are also marked as necrotic. An example of the Delaunay reconstruction can be seen in Figure 4.2.

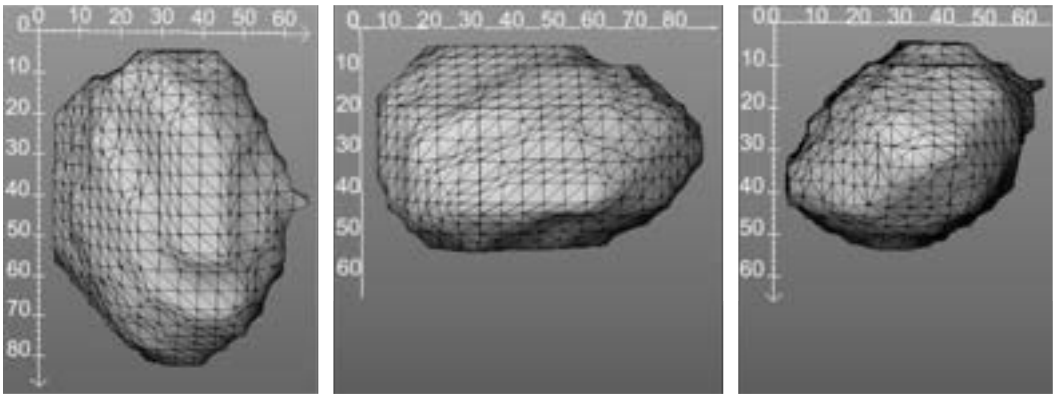

Fig. 4.2: Reconstruction results for the Delaunay triangulation in axial (left), sagittal (middle) and coronal (right).

4.3.4 Minimum Volume Enclosing Ellipsoid

The construction of an ellipse around the applicator's main axis models the idealized concentric heat distribution. The applicator can be interpreted as many heat point sources in a row. The maximum of heat is generated in the electrode of the applicator and decreases along the applicator's main axis. In homogeneous media, the heat of a plane point source decreases exponentially with quadratic distance. This results in the typical ellipsoid shape of the coagulation necrosis. With this a priori knowledge, a proper geometric model is determined. In the presented approach, ellipses are formed slice-wise perpendicular to the applicator's main axis following the extent and alignment of the necrotic voxels. By exploiting this behaviour, irregularities of the heat distribution or incomplete data can be compensated by the convex hull.

The implementation is based on the work by Nima Moshtagh's algorithm for the computation of the MVEE (Moshtagh et al., 2005). This algorithm calculates the parameters of an ellipsoid with the smallest volume by containing a set of n dimensional data points P_i. The algorithm is applied slice-wise on each 2D voxel slice perpendicular to the applicator's main axis. The parameter consisting of the center c, the two radii r_1 and r_2 and the rotation matrix of the ellipse are calculated by solving the following optimization problem:

$$log(det(A)) \rightarrow min \tag{4.4}$$

such that

$$(P_i - c)^T \cdot A \cdot (P_i - c) \leq 1 \tag{4.5}$$

with A containing all information regarding the shape of the ellipses. This information can be decomposed by a singular value decomposition:

$$[U\ Q\ V] = svd(A) \tag{4.6}$$

with U and V defining a first and second rotation matrix of the ellipse, respectively. The scaling matrix Q is containing the singular values σ_1 and σ_2, which are representing the semi-major and semi-minor axis of the ellipse. The radii r_i can now be calculated by:

$$r_i = \frac{1}{\sqrt{Q_{ii}}} \tag{4.7}$$

Each voxel x_i inside of the generated ellipses is assumed to be coagulated and will be flagged as necrotic. In this way, a three-dimensional coagulation necrosis is created. An example of two slices along the applicator's main axis can be seen in Figure 4.3.

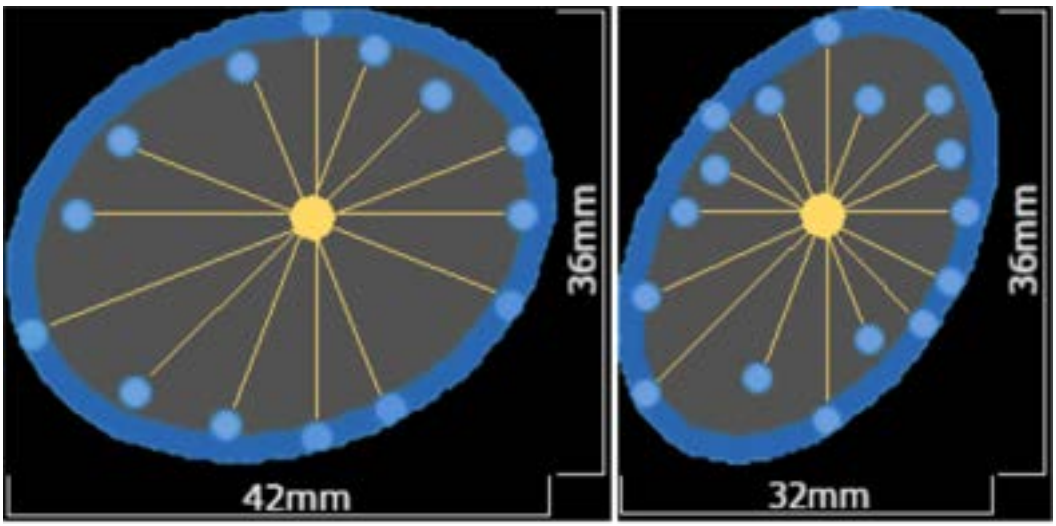

Fig. 4.3: MVEE reconstruction for homogeneous phantom number 1. Exemplary shown are slice 44 and 58 along the applicator's main axis (yellow dot). Visible are the rotated MR images (yellow lines), the data points used as an input (light turquoise) and the corresponding computed outline of the reconstruction (dark turquoise). Note that the number of input points may vary due to outlier detection.

4.3.5 Bezier Splines

Considering the necrotic contour voxels of the live data slice-wise perpendicular to the applicator's main axis, the link between two neighbored voxels is done by a polynomial of third degree for creating a smooth, naturally curved shape. This method forms a concave and closed hull. The effect of drawing a tight hull around the data only results in a local impact of outliers on the overall reconstruction. The interpolation of incorrect live data is determined by the two neighbored slices. Hence, a proper sampling rate of the volume leads to a good reconstruction despite erroneous or missing data.

The 3D volume consisting of the oriented necrosis maps is sliced perpendicular to the applicator's main axis. The order of connecting the voxels V is determined by the size of angles regarding their cylinder coordinates V_c:

$$\begin{aligned} V(x,y,z) &= V_c(r,\theta,z) \\ r &= \sqrt{(x-x_c)^2+(y-y_c)^2} \\ \theta &= atan2\left(\frac{x-x_c}{y-y_c}\right) \end{aligned} \tag{4.8}$$

with (x,y) representing the Cartesian coordinates of a voxel in a slice z, r representing the radius, θ representing the angle of the cylindric coordinates and (x_c,y_c)

representing the Cartesian coordinates of the applicator's main axis in each slice z. The voxels are listed in ascending order of their angles in relation to 0° MRI slice, so that for two voxels i and j, the following neighborhood condition applies:

$$0 > i < j \leq n \text{ if } \theta_i < \theta_j \tag{4.9}$$

Afterwards, the set of voxel data is interpolated by a continuous closed Cubic Bezier Curve using de Boor's Algorithm (De Boor et al., 1978). De Boor's algorithm introduces a fast and stable way to evaluate a point on a B-spline curve by not directly computing the B-spline functions but evaluating the spline curve through an equivalent recursion formula. For determining the voxels inside the closed hull to flag them as necrotic, the winding number algorithm after Sunday's implementation (Sunday, 2004) is used. This is more robust for points close to complex polygon boundaries and is as fast as comparable methods. An example of the splines method for two slices is shown in Figure 4.4.

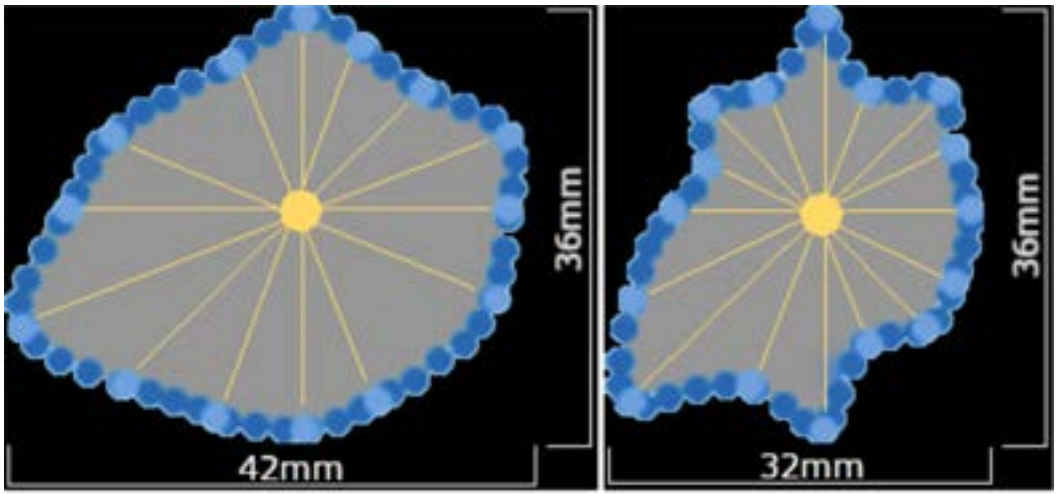

Fig. 4.4: Spline reconstruction for homogeneous phantom number 1. Exemplary shown are slice 44 and 58 along the applicator's main axis (yellow dot). Visible are the rotated MR images (yellow lines), the data points used as an input (light turquoise) and the corresponding computed outline of the reconstruction (dark turquoise). Note that the number of input points may vary due to outlier detection.

4.4 Experimental Setup

Evaluation of the explained reconstruction methods was conducted on the same 13 bio protein data sets as introduced in Chapter 3 to ensure comparability of the results. All methods are evaluated with respect to:

1. Accuracy: Improvement of the DSC and the SEM.
2. Robustness: Compensation of artifacts and MR inhomogeneities.
3. Adaptability: Necessity of a priori knowledge about vessels and real-time capability.

If not mentioned explicitly, all results were acquired without taking the a priori knowledge about vessels into account. All data sets provide a ground truth manually extracted by a medical expert after the intervention. The DSC was computed according as explained in Section 3.4 using an SEM at a confidence level of 95% ($p = 0.05$) over all 13 phantoms.

In the following Sections outliers will refer to single slices in the interventional protocol, which show a very low SNR. This causes the predefined threshold to highly overestimate the coagulation necrosis even when optimized. With respect to the original temperature interpolation these corrupted slices caused the method to fail. These outliers can mainly be observed in perfusion phantoms 1 and 4 and are therefore examined carefully during the evaluation. Outliers are detected and removed as explained in Subsection 4.3.2. Examples images of those phantoms for two orientations can be seen in Figure 4.5.

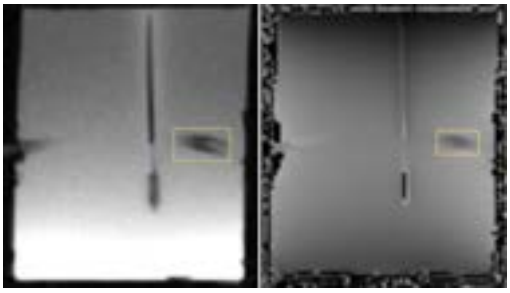

(a) Artifact affected perfusion phantom 1 at time point 1.

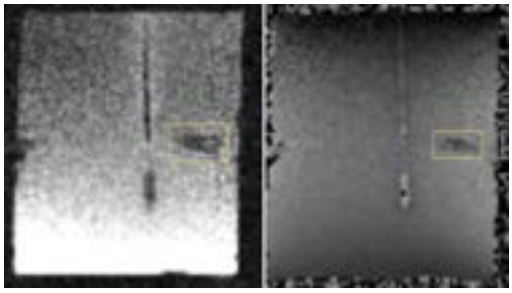

(b) Artifact affected perfusion phantom 1 at time point 2.

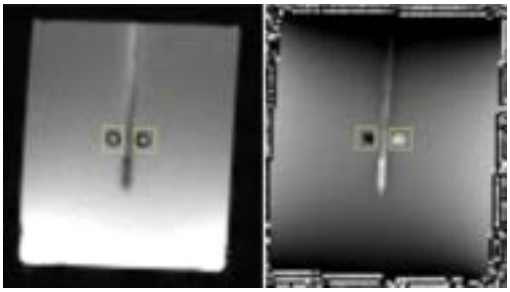

(c) Artifact affected perfusion phantom 4 at time point 1.

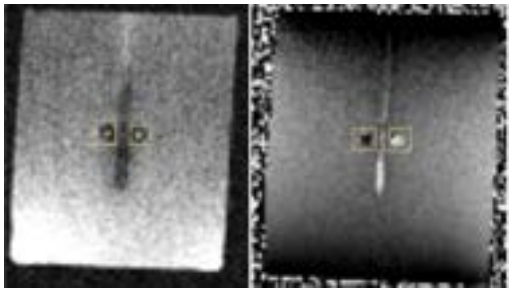

(d) Artifact affected perfusion phantom 4 at time point 2.

Fig. 4.5: All four panels show the magnitude (left) and corresponding phase (right). It is noticeable that the SNR of the data changing rapidly between two consecutive time points. The yellow rectangles show the inserted PVC tubes.

Accuracy

During testing of the accuracy, the introduced bias for estimating the coagulation necrosis was carefully examined. Due to the use of bio protein phantoms the critical temperature model is applied instead of the CEM_{43} or Arrhenius model (M. S. Breen et al., 2007; Rempp et al., 2012). The thermal threshold was identified for each phantom individually within a range of 50-60°C. Because the evaluation is focused on the reconstruction algorithms and not on the temperature accuracy of the acquired images the used coagulation thresholds were identified by applying the thresholds in a range from 0°C to 100°C for each orientation. The results for each value were compared to the corresponding image plane in the ground truth and the optimal threshold for each orientation was identified. Due to the pH-value inhomogeneities in the phantoms this approach shows different optimal thresholds for different orientations reflecting the tissue inhomogeneities in a human. Unfortunately, the phantoms did not show a proper sub-lethal transition zone in the post-treatment images. Therefore, only one threshold is applied to define if a voxel is coagulated or not, neglecting sub-lethal damage to the tissue. Nonetheless, the threshold for this estimation highly depends on the pH-value of the phantoms, which can vary much within each phantom according to Bu Lin et al. (2008). To address this bias, the new methods are not only evaluated with the original global threshold used in Chapter 3, but also with two other introduced thresholds. In addition, it is investigated how well the presented methods will perform considering perfect input. Therefore, the given ground truth is resliced for each data set and the eight predefined orientations, usually acquired during live imaging, are extracted. Afterwards, these eight slices are used as an input for reconstruction to simulate a perfect input. The resulting set of tested inputs consists of the following three thresholds for necrosis estimation and the resliced ground truth:

1. Global: Original threshold used in Chapter 3.

2. Median: The optimal threshold for each orientation was empirically determined. Afterwards, the median threshold value from each of the eight orientations was used for reconstruction to reliably remove outlier thresholds (global compensation of pH value inhomogeneities, which may result in unrealistic thresholds of e.g, 25°C or 84°C).

3. Local: The optimal threshold for each orientation is used for reconstruction (local compensation of pH value inhomogeneities).

4. Ground truth: Resliced ground truth offering perfect input.

Robustness

The test for the robustness of the proposed methods, is focused on the evaluation of phantoms with perfusion to simulate a heat sink effect. Here, the perfusion phantoms number 1 and 4 show strong artifacts and MR inhomogeneities causing th initial method presented in previous Chapter to fail. All the methods with and without these critical data sets are compared to determine the influence of heavily corrupted data on the methods.

Adaptability

Regarding the adaptability, each reconstruction is performed two times. First, the a priori knowledge is taken into account by providing the segmented vessel structures as input to each algorithm. After reconstruction, these vessels are subtracted from the result to enforce a proper deformation of the reconstructed volume. During the second reconstruction, no a priori knowledge is provided as additional input. For evaluation, the volume of false positive classified voxel values is computed by subtraction of both corresponding reconstructions. Thus, it can be identified which algorithm performs best in the presence of vessel structures.

In addition, each reconstruction was performed 100 times to measure the mean computational time and the standard deviation. For the accuracy and adaptability experiments, additional one-way ANOVAs were conducted with respect to the different used algorithms. Afterwards, post-hoc tests were performed using pairwise t-tests with Bonferroni correction. An exemplary overview about the performance of the algorithms tested can be seen in Figure 4.6.

4.5 Results

All methods where evaluated regarding accuracy, robustness, and adaptability. In the following subsections, the results with respect to these three parameters are presented. A summary of the ANOVAs' results can be observed in Table 4.3. Statistically significant post-hoc test results can be seen as horizonal lines in the corresponding Figures for accuracy and adaptability tests. All boxplots show the interquartile range (box), the 25th and 75th percentile (borders of each box), the median (horizontal line in the box), the minimum and maximum values (whiskers) and the potential outliers (dots).

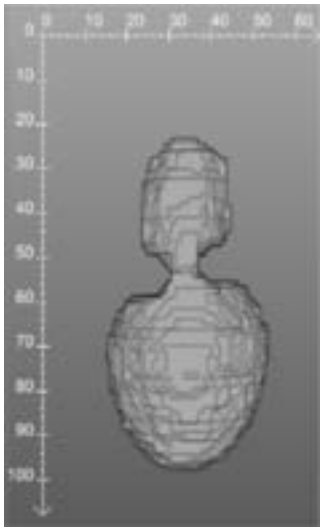

(a) Groundtruth for perfusion phantom 2.

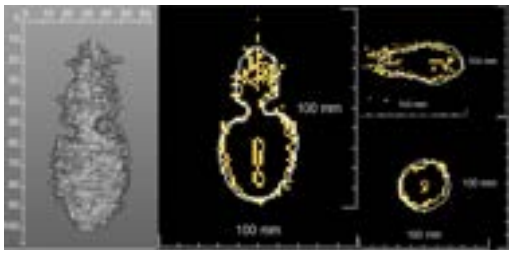

(b) Temperature interpolation reconstruction for perfusion phantom 2.

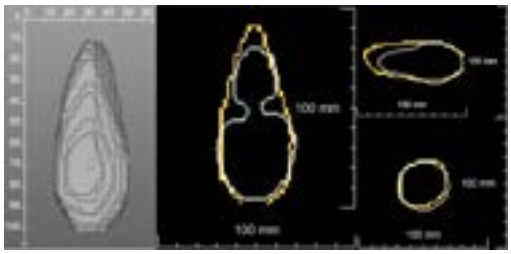

(c) Delaunay reconstruction for perfusion phantom 2.

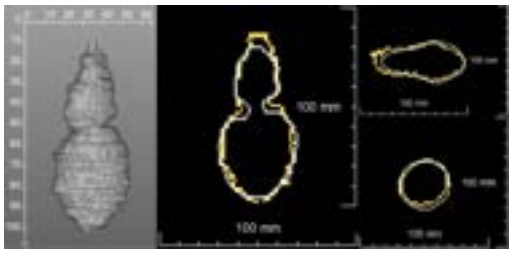

(d) MVEE reconstruction for perfusion phantom 2.

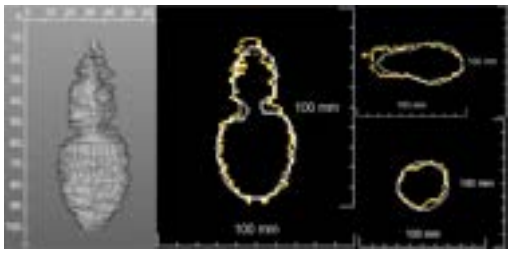

(e) Splines reconstruction for perfusion phantom 2.

Fig. 4.6: Reconstructions for perfusion phantom 2. Visible are the ground truth contours (white) in addition to the output contour (yellow) in axial, sagittal an coronal. The 3D representation is shown without any smoothing or other visual post-processing applied.

4.5.1 Accuracy

An overview of the accuracy test results can be observed in Figure 4.7. The global threshold is identical with the one used in Chapter 3. The splines (0.75 ± 0.08) and MVEE (0.74 ± 0.07) method yield comparable DSC results to the original temperature

Tab. 4.3: Summary of the ANOVAs' results. Df = Degrees of Freedom in the numerator, F = F-value, p = probability of the data given the null hypothesis, Sig. = p-values less than the traditional α <0.05, η^2 = Generalized Eta-Squared measure of effect size.

Variable	df	F	p	Sig.	η^2
Accuracy					
Algorithm with Global Threshold	3	3.86	0.017	*	0.056
Algorithm with Median Threshold	3	4.16	0.013	*	0.107
Algorithm with Local Threshold	2	51.82	<0.001	*	0.542
Algorithm with Ground Truth Threshold	2	116.66	<0.001	*	0.687
Adaptability					
Algorithm with Median Threshold	3	39.99	<0.001	*	0.81

interpolation (0.73±0.07) method, whereas the Delaunay triangulation performs more poorly (0.69±0.04). The median thresholds for each data set shows slightly different results. The effect of the new thresholds mainly affect the corrupted data sets of the perfusion phantom 1 and 4. Here, the compensation of the bias introduced by the pH value variations causes the splines (0.77±0.04), MVEE (0.80±0.03) and even the Delaunay triangulation (0.75±0.02) to outperform the initial method (0.73±0.07) presented in the previous Capter. The local threshold, which is individual for each of the eight orientations, could not be applied to the temperature interpolation method because the necrosis estimation was performed on the reconstructed volume instead of every input slide. For the new approaches, the optimized local threshold shows that the Delaunay triangulation (0.78±0.02) performs more poorly than the other two. The splines method (0.81±0.02) performes somewhat worse than the MVEE (0.84±0.02) regarding the mean DSC, but still better than Delaunay and the temperature interpolation method.

Overall, the results regarding accuracy show a meaningful trend in favor of the MVEE method followed by the splines approach. The Delaunay triangulation performs worst in most tested scenarios. This statement is supported by evaluation of the ground truth reconstruction which simulates a perfect input. Here, the Delaunay triangulation achieves a maximum of 0.88±0.02, the splines of 0.92±m0.01 and the MVEE of 0.95±0.01. For the purpose of further testing, the median threshold will be used, as it best reflects the real clinical conditions.

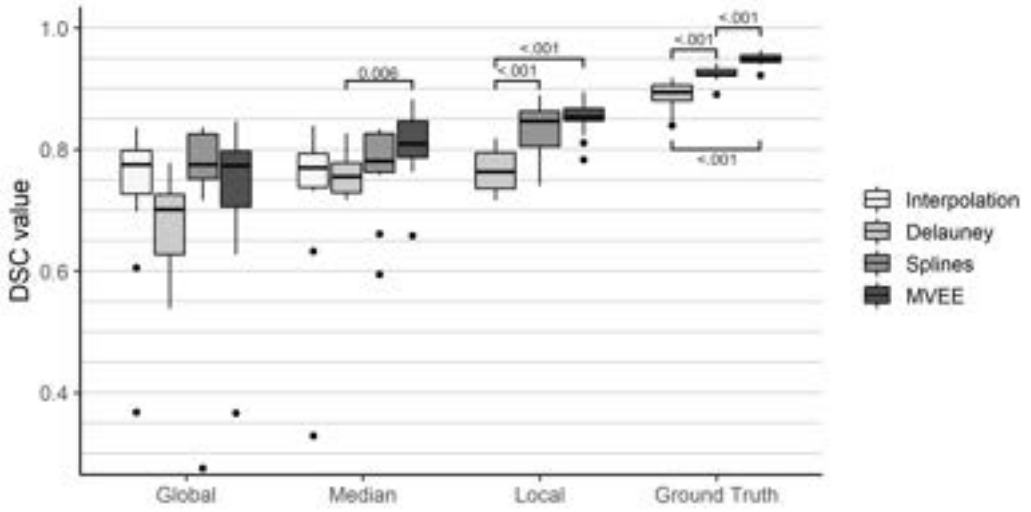

Fig. 4.7: Results of the accuracy tests for all 13 phantoms. DSC measurements are separated for each method and each tested threshold with: Global = Threshold used in the previous interpolation method. Median = Median threshold from all eight orientations. Local = Individual threshold for each orientation. Ground Truth = Resliced input data from the ground truth. Horizontal lines indicate statistically significant post-hoc pairwise t-test results.

4.5.2 Robustness

A graphical overview about the results regarding the robustness test can be seen in Figure 4.8. After removing the corrupted perfusion phantoms number 1 and 4, the mean DSC of the interpolation method is improved by 0.05, while the standard deviation decreases by 73.61% from ∼0.07 to ∼0.02. The Delaunay triangulation improves by just 0.01 with a nearly identical standard deviation. The spline method shows a 0.04 higher DSC after outlier removal, whereas the MVEE method shows an improvement of 0.02. Regarding the standard deviation, the splines method improves by 53.87% from ∼0.04 to ∼0.02 and the MVEE method by 32.07% from ∼0.03 to ∼0.02. Two sample t-tests between the groups "With Outliers" and "Without Outliers" for the algorithms temperature interpolation (p=0.27), Delauney (p=0.75), Splines (p=0.27) and MVEE (p=0.40) were performed. No significant differences could be observed.

Overall, it can be observed that the new methods show less variation in the standard deviation, including the corrupted data sets than the original temperature interpolation method. Nonetheless, no significance could be observed. Between the new approaches, no trend can be observed.

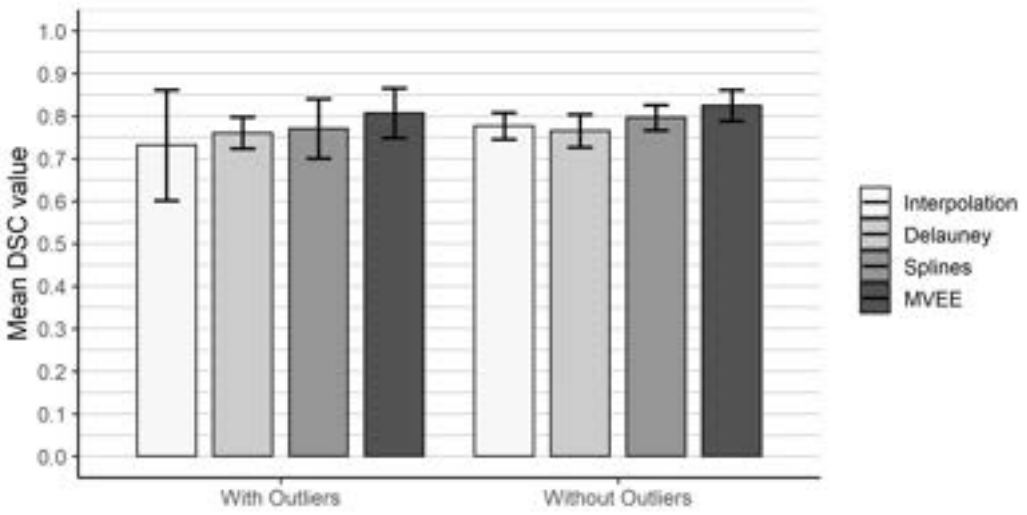

Fig. 4.8: Results of the robustness tests. The median threshold was used for necrosis estimation and the error bars correspond to the standard deviation. With outliers = All data sets were taken into account including the highly corrupted data sets. Without outliers = Perfusion phantom 1 and 4 were left out of the evaluation. No statistical significance was found.

4.5.3 Adaptability

An overview of the adaptability test can be observed in Figure 4.9. The original interpolation method shows a mean volume of 0.21±0.10ml incorrectly classified voxels, closely followed by the splines and MVEE method with 0.52±0.10ml and 1.18±0.30ml, respectively. The Delaunay triangulation offers the worst result regarding the adaptability with a mean volume of 2.12±0.53ml false positive classification regarding the vessels. The maximum vessel volume affected by the coagulation necrosis was computed at 1.5±0.42ml.

Overall, it can be said that the original interpolation method shows the least false positive classification of vessel voxels whereas the Delaunay triangulation performs the worst regarding the vessels even exceeding the maximum vessel intersection due to overestimation of the coagulation necrosis. While comparing the splines and the MVEE method, it can be noticed that the splines not only showed a lower mean for false positive classification, but also provided a much lower standard deviation over all six perfusion phantoms. Regarding the robustness there is a trend towards the temperature interpolation and the splines.

With respect to the reconstruction times, the temperature interpolation (C++) method shows 8.02±5.91ms, the Delauney trinagulation (Python) 1.57±0.3s, the MVEE method (Python) 4.5±0.6s and the Spline method (Python) 6.2±0.55s.

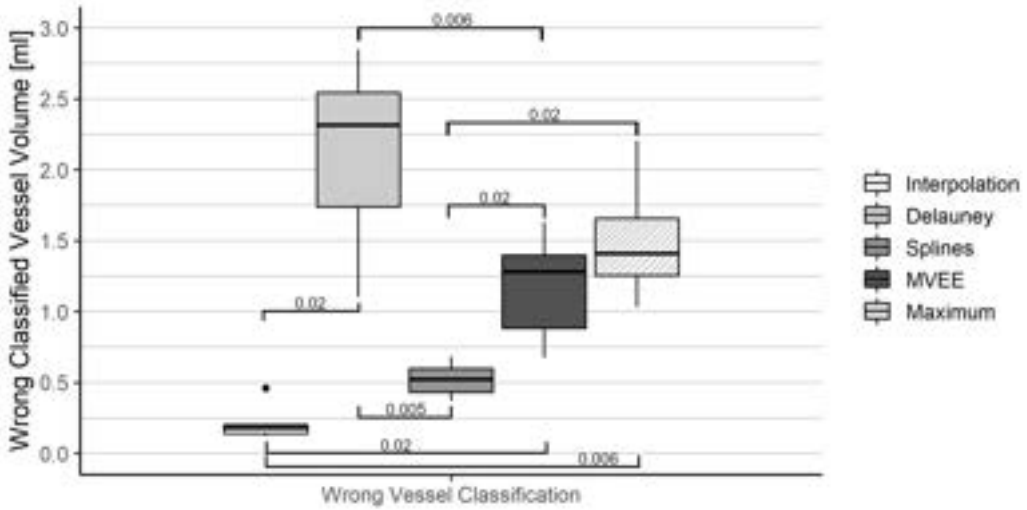

Fig. 4.9: Results of the adaptability tests. The volume of the wrongly classified voxels can be seen for each of the four algorithms. In addition, the boxplot "Maximum" indicates the true vessel volume affected by the coagulation necrosis over all six perfusion phantoms. Horizontal lines indicate statistically significant post-hoc pairwise t-test results.

4.6 Discussion and Conclusion

Regarding accuracy, the results show a strong trend in favor of the MVEE method. Apparently, MR inhomogeneities and other artifacts cause the data to frequently underestimate the coagulation necrosis when computed through a simple threshold. In these cases, the MVEE method is able to compensate for this loss of information and provide a proper reconstruction. The big disadvantage of the MVEE approach, on the other hand, can be observed during experiments with the perfusion phantoms. The compensation of the underestimation of the coagulation necrosis also causes the vessels to vanish to an extent, which is not considered negligible. The splines method was shown to be more capable of dealing with vessel structures, but on the other hand shows a lower DSC similarity overall. The Delaunay triangulation shows an even worse performance than the temperature interpolation method, which is caused by the approach itself. Fitting a triangulation mesh to a set of points completely neglects any deformation caused by vessels and others. Even though this approach is well suited for homogeneous heat distributions without any anomalies, it is far from a real-life scenario. Therefore, the Delaunay triangulation will not be investigated further.

The differences regarding the similarity are mainly caused by a continuous underestimation of the coagulation necrosis. This underestimation is not only caused by

the approach used to recompute the heat maps, the noise, and other artifacts in the images, but also by the partially strong pH value variations within the phantom. Here, it would be suitable to conduct more studies with ex vivo organs to see if these variations have an impact on the overall similarity of reconstruction. In a later step, the image acquisition protocol should also be tested in a real clinical setup, e.g., with the use of in vivo animal experiments. In addition, the adaptability of the presented approach may be increased by a dynamic framework which does not need predefined reference images for heat map reconstruction. To achieve this reference-free thermometry, approaches as introduced by Salomir et al. (2011) can be combined with framework presented in the present thesis. A reference-free thermometry would allow for a life adaptation and change of the region of interest, e.g., when a vessel or organ boundary was automatically detected during the intervention (e.g., through deep-learning approaches). To overcome the temporal heat variation in single voxels caused by local MR inhomogeneities or artifacts, it might be suitable to combine the presented approach with real-time simulations of the heat transfer. A first approach would be the use of the Pennes' Bioheat Equation (Wissler, 1998) while optimizing the simulation parameters based on the live data for different orientations. This approach could result in an even higher accuracy while providing a visually more appealing result, which can be easier to use by a clinical end user. Furthermore, this approach may also be extended by using a Kalman Filtering to achieve a self-adaptive hybrid magnetic resonance thermometry as introduced by Zhang et al. (2016). Their method offers the possibility to follow temperature changes in presence of motion and adapt the temporal and spatial resolution of the thermometry. Using Kalman filters the acquired data can be corrected, and corrupted data points within the images can be removed. Therefore, this approach may be beneficial to better spot heat sinks (e.g. caused by vessels) and get a better understanding of their effects during ablation.

Using the resliced ground truth, it was shown that the proposed methods work well with appropriate initial input, which is mainly dependent on the used 2D GRE sequence. Because the setup is able to take any 2D phase or temperature input with any number of orientation, it can directly utilize new image sequences as soon as they are published. This allows the presented setup to be applicable to a wide range clinical setups as well as providing an improved reconstruction along with the improvement of the MR sequences.

Conclusion. In this Chapter, three approaches for the reconstruction of a volumetric coagulation necrosis for the monitoring of MWA procedures were compared and analyzed. All methods are able to utilize any 2D MR sequence, as long as the sequence provides phase images for heat map reconstruction. It can be observed that

the spline and MVEE approach have the potential for highly accurate reconstruction of the volume while outperforming the previously proposed interpolation method in a more realistic setup regarding accuracy and robustness. To overcome local inhomogeneities caused by noise or MR dependent artifacts, the use of adaptive simulations should be considered in the future to compute a more homogeneous volumetric map. Future work should also conduct studies in ex vivo and in vivo animal experiments to verify transferability from the phantoms to a more realistic environment.

5 Probabilistic CEM43 Thermal Dose Model

About this chapter

Parts of this chapter are currently under peer-review in: Simon Schröer and Julian Alpers, Marcel Gutberlet, Inga Büsch, Regina Rumpel, Frank Wacker, Bennet Hensen, and Christian Hansen. “A Probabilistic Thermal Dose Model for the Estimation of Necrosis in MR-guided Tumor Ablations”. In: Medical Physics. Significant medical input was provided by Dr. Bennet Hensen. The methods described in this Chapter are developed and implemented by Simon Schröer as part of a Master’s Thesis supervised by the author of this thesis. The author of this thesis does not take any credit for the derivation of the mathematical models developed by Simon Schröer as described in Section 5.3.

5.1 Introduction

> *Medicine is a science of uncertainty and an art of probability.*
>
> — **William Osler**
> Former professor at John Hopkins Hospital

For a successful outcome of a thermal ablation procedureit is important that the tumor cells are fully destroyed within a certain minimal ablative margin (Laimer et al., 2020). Not fully destroying the tumor cells within this minimal ablative margin due to a premature termination of the procedure will increase the risk of a local recurrence (Laimer et al., 2020). This can happen when the imaging modality is not sufficiently precise or external influences such as electromagnetic interferences cause the acquired images to become inaccurate. Subsequently, the necrosis maps computed from these images may provide false information to the radiologist. They could for example show pixels falsely classified as necrotic which would then cause the radiologist to prematurely stop the treatment if they think the entire tumor is destroyed. Therefore, a precise measurement is important if the ablation is to be successful. Furthermore, an estimation of the uncertainty with which the pixels are classified as necrotic or not necrotic does not yet exist but could provide additional information to help surgeons to successfully destroy the tumor. The causes of the errors and uncertainty in imaging are manifold. Some uncertainty is introduced by the imprecision with which an MRI device conducts its measurements. Some errors are introduced by imaging artifacts due to electromagnetic interference or metal objects within the patients body. Others are in turn caused by numerical approximations in the mathematical models computing the thermal dose. Current state-of-the-art thermal dose models such as the CEM_{43} model and the Arrhenius model use deterministic equations to classify pixels as necrotic. The character of the MRI measurement error, however, is probabilistic in nature. To sensibly incorporate the error into the thermal dose estimation, a new model therefore needs to work with random variables instead of scalar values. A mathematical framework based on stochastic instead of deterministic equations will subsequently have the advantage of being able to take different uncertainties and errors into account. Evidently, there is a need for a mathematical framework that helps estimate the uncertainty of the necrosis map classification and accounts for these sources of errors within the thermal dose computation.

This chapter will introduce a mathematical framework based on the CEM_{43}, which is able to estimate the thermal dose applied to tissue during a thermal ablation. PDFs

describing the distribution of measured quantities are derived. These PDFs are able to provide a probabilistic estimation of the variables as opposed to the typical scalar representation in other thermal dose models. As a result a novel way of computing necrosis maps , which are potentially more accurate and robust than the conventional CEM_{43} model and can still be computed in real time.

5.2 Related Work - Probabilistic CEM43 Thermal Dose Model

The major novelty in the present chapter is the analysis of the MR measurement error and the impact to the computation of the conventional CEM_{43} necrosis model. Focus lies on the probabilistic behaviour of the error and how to propagate this error from the image acquisition to through the PRFS thermometry up to the computation of the necrosis. To get a proper overview of the existing methods an initial unstructured literature research was conducted. Based on the results, frequently used phrases and synonyms where identified and collected to define a proper search term. Regarding the topic of probabilistic error propagation, the term was divided into three major categories, also observable in Table 5.1:

1. The first category describes the factor of uncertainty or probability
2. This chapter is focusing on the influence of the MR measurement error on the necrosis estimation. Here, all three state-of-the-art methods should be used, namely the CEM_{43} model, the Arrhenius model and the critical temperature (threshold) model.
3. To reduce the number of unrelated papers the focus in category three lies on the medical part. Here, the points of interest focus on thermal ablation procedures for any image guidance approach.

After definition of the presented categories a structured literature research was performed for the last ten years from 01.01.2012 to 31.07.2022 on PubMed. Connecting the columns in Table 4.1 with logical AND operations and including the date range the following search term was created:

((Probabilistic[Title/Abstract] OR Probability[Title/Abstract] OR Uncertainty[Title/Abstract])

AND

(CEM43[Title/Abstract] OR CEM 43[Title/Abstract] OR Arrhenius[Title/Abstract] OR Critical temperature[Title/Abstract] OR necrosis[Title/Abstract] OR necrotic[Title/Abstract] OR denaturation[Title/Abstract])

AND

(ablation[Title/Abstract] OR thermal[Title/Abstract] OR hyperthermia[Title/Abstract])

AND

(2012/1/1:2022/7/31[pdat]))

Tab. 5.1: Synonyms for the literature research regarding 2D to 3D reconstruction approaches. The categories can be divided into "Dimensionality", the used "Approach" and "Others".

Synonym	Probability	Necrosis Model	Procedure
1	probabilistic	CEM43	ablation
2	probability	CEM 43	thermal
3	uncertainty	Arrhenius	hyperthermia
4	—	critical temperature	—
5	—	necrosis	—
6	—	necrotic	—
7	—	denaturation	—

This search term yields 54 results, which are analysed in a first title/abstract research. Considered for a more detailed analysis where 13 papers dealing with the topic of uncertainty estimation in any kind. Those papers were analysed in more detail performing a full paper research. All papers describing a probabilistic approach to measure the outcome of an error prone algorithm where included resulting in one relevant paper for the last ten years from McDannold et al. (McDannold et al., 2020), which will be explained in more detail later. Because the literature research was not providing a sufficient amount of papers another unstructured literature research was conducted expanding the search to other related fields: The uncertainty propagation in ablation simulation, thermal dose and thermometry error analysis and correction and a more general analysis of the CEM_{43} model. It can be seen that these areas of research use similar approaches with a different scope or aim.

Regarding the uncertainty propagation in ablation simulation, Ristovski et al. (2019) analyzed the uncertainty of thermal ablation based on the variability of biological tissue parameters with radiofrequency ablation simulations. The simulation at the core of their work uses a set of partial differential equations describing the heat diffusion

through the tissue. Introducing the uncertainty of the biological tissue parameters as random variables the propagation of this uncertainty is then investigated. For this purpose the partial differential equations are rewritten as stochastic differential equations. The simulation is executed with a stochastic finite element method to obtain a per pixel PDF for the ablation of the underlying tissue. The biggest differences to the presented Chapter are the data input and the error observed. Ristovski et al. (2019) make use of simulated data not considering live data input and their uncertainty stems from the variability of biological tissue parameters, while the presented approach investigates the uncertainty due to imprecise measurement of the MR image acquisition and numerical errors. Labarbera (2017) analyzed the uncertainty of tumor ablation by irreversible electroporation caused by a varying conductivity in the tumor and the surrounding tissue. The tumor and tissue conductivity are treated as random variables with PDFs which were taken from the literature. A Monte Carlo simulation was used to determine the volume of the ablation zone as well as the mean and the standard deviation of the electrical field experienced by the tumor. Similar to the framework presented in this Chapter, their work computes the uncertainty of the ablation zone based on randomly distributed parameters. As with the approach presented by Ristovski et al. (2019), however, this method describes uncertainties within a simulation and can therefore not necessarily be applied to real ablation procedures. Furthermore, Labarbera (2017) investigate the uncertainty caused by the tumor and tissue conductivity and not the uncertainties including MR image acquisition and numerical errors. Further similarities to the present Chapter can be seen in the works of Jiang et al. (2021) and Dos Santos et al. (2009). These publications investigate the effects of the uncertainty of multiple parameters on the outcome of irreversible electroporation and radiofrequency ablation, respectively. Jiang et al. (2021) observed the parameters pulse intensity, electrode diameter, the location of the electrode from the center of the tumor, electrode length, and number of electrode. Dos Santos et al. (2009) observed the parameters thermal conductivity, specific heat, blood perfusion, and electrical conductivity. Both works investigate the influence of the uncertainty of parameters on the outcome of the respective procedure similar to the approach presented in this Chapter. The purpose of both works, however, is to find out what factors the outcome of the respective procedure is most sensitive to, which differs from the overall purpose of this Chapter. Furthermore, the area of application is again restricted to simulations.

With respect to thermometry and thermal dose error analysis and correction, Zucconi et al. (2014) analyzed the errors in PRFS-based MR thermometry and their effects on the thermal dose during a HIFU ablation. They additionally proposed a low-pass filtering on temperature maps to reduce errors in the thermal dose. This method was

evaluated through a Monte Carlo simulation and showed promising results reducing the overestimation factor of the thermal dose from 2.62 without the filter to 1.11 with the filter. While their work analyzes the error of PRFS-based MR thermometry and its influence on the thermal dose similar to the presented method, it differs in its scope and methodology. The work of Zucconi et al. (2014) conducts a statistical analysis of the thermometry error and does not provide a solid theoretical background to allow the derivation of general principles for describing the thermal dose error. Additionally, it only focuses on the error at the stage of the thermometry while the present Chapter considers the error at an earlier stage in the MRI processing pipeline. Baron et al. (2014) created a model-based approach for correcting PRFS-based thermometry influenced by heat-induced magnetic susceptibility changes during HIFU ablation. A 3D model was created by monitoring an ablation in breast fat and recording the changes in magnetic susceptibility. Subsequently, a second ablation procedure was conducted and monitored for which the temperature profile was then corrected based on the 3D model recorded before. However, Baron et al. (2014) do not provide any tools to estimate uncertainty or predict the influence of errors on the final ablation result. Furthermore, their approach does not provide any insight into the theoretical character of the error as the model used is utilized as a black box to correct existing errors. Viallon et al. (2010) observed PRFS-based MR thermometry artifacts caused by the formation of gas-bubbles at high voltages influencing the magnetic susceptibility during radio frequency ablation. Additional factors correlating with the severity of the errors caused by the artifacts were investigated. A model assuming a Gaussian dynamic source of susceptibility was used to successfully correct the artifacts. Similar to the present Chapter, their work investigates the influence of specific factors on the accuracy of MR thermometry. However, the scope of the approach is limited to the investigation of the errors caused by cavitation-induced artifacts. Additionally, it does not consider the influence of these artifacts on the thermal dose. It also does not provide any theoretical description for the errors, which could be used to mathematically predict or estimate the influence of these artifacts more generally.

Regarding the mathematical foundation of the CEM_{43} model Sapareto et al. (1984) described the accumulated thermal dose in equivalent-minutes. With the values computed by the proposed equation effects of thermal exposure can be compared regardless of the specific temperature profile or the exposure time. The presented method utilizes the work of Sapareto et al. (1984) as its mathematical foundation for the proposition of a probabilistic framework. Pearce (2009) described a conversion of a thermal dose computed by the CEM_{43} model to a probability of cell death by taking into account the reaction rates described by the Arrhenius equation. Additionally,

a method was proposed that allows the derivation of Arrhenius model constants from CEM_{43} model data, effectively converting equivalent-minutes into the damage parameter of the Arrhenius model. Their work shows a probabilistic interpretation of the CEM_{43} model similar to the thermal dose model presented in this Chapter. However, it does not take into account any errors or uncertainties caused by MRI measurements imprecision. It only provides a probabilistic representation of the CEM_{43} model without basing the computed probabilities in real influencing factors. Lately, McDannold et al. (McDannold et al., 2020) computed the thermal threshold for the CEM_{43} including the computation of the probability for thermal damage. Even though their work is not computing the probabilistic error of the MR image acquisition it is one of the few attempts to include a probabilistic approach during necrosis estimation.

5.3 Material and Methods

The original CEM_{43} model was derived from the Arrhenius model (Sapareto et al., 1984). In order to solve a continuous integral in real time a numerical integration was used that introduces an error omitted in the final formulation of the CEM_{43} model. This error has to be included in the probabilistic formulation for this potential source of errors to be considered. Rewriting the equation to include this numerical integration error yields the following expression:

$$\tau = \int_0^{t_{final}} \beta^{T(t)-43} dt = \Delta t \sum_{t=0}^{t_{final}} \beta^{\overline{T}_t - 43} + \sum_{t=0}^{t_{final}} \epsilon_t \tag{5.1}$$

where ϵ_t is the error due to numerical integration at time step t. As $\overline{T}_t = \frac{T_{t-1}+T_t}{2}$ is used in practice for two temperature measurements at times $t-1$ and t, the numerical integration shown in Equation 5.1 utilizes a variation of the trapezoidal quadrature rule that averages the temperature over time. Because of this, the quantities $\overline{T}_t = \frac{T_{t-1}+T_t}{2}$ and $\overline{T}_{t+1} = \frac{T_t+T_{t+1}}{2}$ are correlated with each other through the shared temperature measurement T_t. This correlation causes a probabilistic formulation of the CEM_{43} model to become difficult as combinations of correlated stochastic quantities generally have more complex PDFs than independent ones. To prevent these difficulties the numerical integration of the probabilistic formulation will use a variation of the rectangular quadrature rule which uses $\overline{T}_t = T_t$. Even though this quadrature rule has a bigger numerical integration error than the trapezoidal

rule for finite intervals it still converges to the exact solution of the integration as $\Delta t \to 0$. The final probabilistic formulation of the CEM_{43} model can be written as:

$$\tau = \Delta t \sum_{t=0}^{t_{final}} \beta^{T_t - 43} + \sum_{t=0}^{t_{final}} \epsilon_t \tag{5.2}$$

where T_t is the temperature measurement at time t. Observing the formula it is noticeable that all values except T_t and ϵ_t are constants. This leads to the conclusion that these two quantities have to be the source of any non-constant error regarding τ. Indeed, T_t is affected by the measurement error from the MRI device and ϵ_t is the error caused by the numerical integration.

The computation of thermal doses within MR-guided tumor ablation is done in four steps according to the MR thermometry pipeline shown in Figure 5.1. The first step

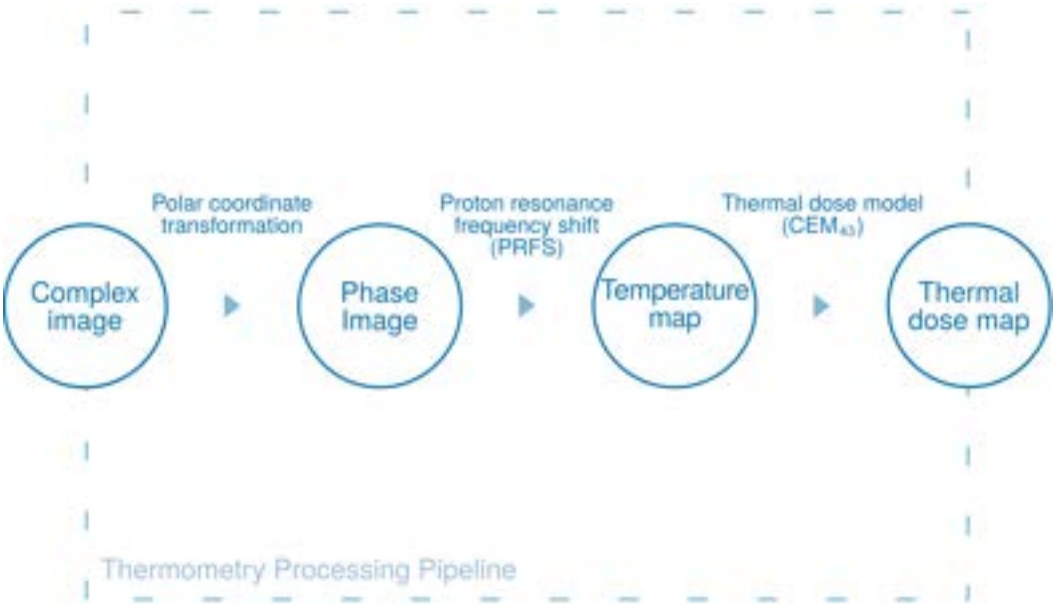

Fig. 5.1: Schematic diagram depicting the mathematical processing pipeline from the complex image acquired by the MRI device to the thermal dose map used for later information extraction.

is the acquisition of complex-valued k-Space data, which is reconstructed into a sequence of complex images via Fourier-Transform. In the second step, phase images are computed from these complex images by means of a polar coordinate transformation. During the third step, the PRFS method as described in Chapter 2.2 can be used to compute temperature maps from the phase images. In the last step, the temperature maps at different points in time are accumulated using the CEM_{43} model to compute the thermal dose maps. Thresholding these thermal dose

maps yields the necrosis maps. The goal of considering the uncertainty introduced by the MRI measurement error is to predict its effects on the final distribution of the thermal dose. This is done by introducing the measurement error at the start of the pipeline and observing its transformation throughout. In the following sections, the MR thermometry pipeline is converted into a probabilistic model, which is used to compute probabilistic necrosis maps.

5.3.1 Complex Image PDF

The first step in the MR thermometry pipeline is the acquisition and Fourier-Transform of complex-valued k-Space data yielding a set of complex images. These raw images contain a complex number for every single pixel consisting of a real component $\hat{R}$ and an imaginary component $\hat{I}$. All following equations will be given with respect to a single pixel unless explicitly mentioned otherwise. As has been found by McVeigh et al. (1985), the measurement error and therefore the distribution of $\hat{R}$ and $\hat{I}$ at this stage has the character of a normal distribution assuming a linear transformation such as the Fourier-Transform is used for reconstruction. For this reason, it can be shown that the underlying values R and I (unaffected by the measurement error) are random variables distributed according to the normal PDF $p_R(x) = \mathcal{N}(\mu_R, \sigma_R^2)$ and $p_I(x) = \mathcal{N}(\mu_I, \sigma_I^2)$, respectively, where μ_R and μ_I are the real and imaginary components as measured by the MRI device. The normal PDF is given by:

$$\mathcal{N}(\mu, \sigma^2) = \frac{1}{\sigma\sqrt{2\pi}} e^{-\frac{(x-\mu)^2}{2\sigma^2}} \tag{5.3}$$

Assuming time-invariant noise the standard deviations of these PDFs can be determined by utilizing reference images that have been recorded pre-operatively. σ_R^2 and σ_I^2 are therefore approximated by the sample variance of the real and imaginary components of the reference images.

5.3.2 Phase PDF

The second step consists of the computation of the phase image by means of a polar coordinate transformation. The phase ϕ can be computed by:

$$\phi = \tan^{-1}\left(\frac{I}{R}\right). \tag{5.4}$$

Taking into account that I and R are normally distributed, the PDF of ϕ can be derived. This can be split into two steps: First, the ratio distribution of $\frac{I}{R}$ is computed. Second, the PDF of ϕ is calculated by transforming the ratio distribution according to tan^{-1}. The ratio distribution of two uncorrelated normally distributed random variables can be computed analytically and Hinkley (1969) stated an equation for the ratio of two correlated normally distributed random variables. Due to the independence of R and I, this equation can be further simplified by setting the correlation factor $\rho = 0$. This allows the PDF of $Z = \frac{I}{R}$ to be written as:

$$p_\phi(x) = \frac{b(x)d(x)}{a^3(x)} \frac{1}{\sqrt{2\pi}\sigma_I\sigma_R} \left[\Phi\left(\frac{b(x)}{a(x)}\right) - \Phi\left(-\frac{b(x)}{a(x)}\right)\right] + \frac{1}{a^2(x)\pi\sigma_I\sigma_R} e^{-\frac{c}{2}} \quad (5.5)$$

where

$$\begin{aligned} a(x) &= \sqrt{\frac{1}{\sigma_I^2}x^2 + \frac{1}{\sigma_R^2}} \\ b(x) &= \frac{\mu_I}{\sigma_I^2} + \frac{\mu_R}{\sigma_R^2} \\ c &= \frac{\mu_I^2}{\sigma_I^2} + \frac{\mu_R^2}{\sigma_R^2} \\ d(x) &= e^{\frac{b^2(x) - ca^2(x)}{2a^2(x)}} \end{aligned}$$

and Φ is the standard normal cumulative distribution function:

$$\Phi(x) = \int_{-\infty}^{x} N(0,1)dx = \frac{1}{2}\left[1 + erf\left(\frac{x}{\sqrt{2}}\right)\right] \quad (5.6)$$

The ratio distribution is transformed by $tan^{-1}\left(\frac{I}{R}\right)$ according to the general transformation rule of random variables. Assuming that the random variable $X \sim f(x)$ is transformed into $Y \sim g(y)$, the new PDF can be written as:

$$g(y) = f(x)\left|\frac{dx}{dy}\right| \quad (5.7)$$

With $p_Z(z)$ being the PDF of $Z = \frac{I}{R}$ it can be utilized that due to $Z = tan(\phi)$ and $x = tan(y)$, the new PDF $p_\phi(y)$ is given by:

$$p_\phi(y) = p_Z(x)\left|\frac{dz}{dy}\right| = p_Z(\tan(y))\left|\frac{dtan(y)}{dy}\right| = p_Z(\tan(y))\frac{1}{\cos^2(y)} \quad (5.8)$$

With this in mind Equation 5.5 can now be substituted into $p_\phi(y)$ yielding the final formula:

$$p_\phi(x) = \left(\frac{b(x)d(x)}{a^3(x)} \frac{1}{\sqrt{2\pi}\sigma_I\sigma_R} \left[\Phi\left(\frac{b(x)}{a(x)}\right) - \Phi\left(-\frac{b(x)}{a(x)}\right) \right] + \frac{1}{a^2(x)\pi\sigma_I\sigma_R} e^{-\frac{c}{2}} \right) \frac{1}{\cos^2(x)}, \tag{5.9}$$

where

$$\begin{aligned} a(x) &= \sqrt{\frac{1}{\sigma_I^2}\tan^2(x) + \frac{1}{\sigma_R^2}}, \\ b(x) &= \frac{\mu_I}{\sigma_I^2}\tan(x) + \frac{\mu_R}{\sigma_R^2}, \\ c &= \frac{\mu_I^2}{\sigma_I^2} + \frac{\mu_R^2}{\sigma_R^2}, \\ d(x) &= e^{\frac{b^2(x) - ca^2(x)}{2a^2(x)}}. \end{aligned}$$

and $\Phi(x)$ is the cumulative distribution function of the standard normal distribution.

5.3.3 Temperature PDF

After deriving the phase PDF it now has to be transformed into a temperature PDF by utilizing the PRFS method and its linear correlation between phase and temperature. The variables T_0 and $\phi(t_0)$ will be assumed to be scalars without any intrinsic uncertainty because of the following reasons:

1. It is presumed that T_0, as the baseline temperature, is determined prior to the intervention with adequate precision.

2. Because $\phi(t_0)$ is not a single image but the mean of all baseline images acquired the error information omitted by assuming this quantity to be exact is negligible.

Analogous to the Subsection 5.3.2 Equation 5.7 can be utilized to transform the PDF of ϕ into the PDF of the temperature T. By solving the PRFS Equation 2.7 for ϕ and substituting it into Equation 5.7, the PDF $p_t(x)$ can be written as:

$$\begin{aligned} p_T(y) =& p_\phi(x) \left| \frac{dx}{dy} \right| \\ =& p_\phi((y - T_0)\gamma\alpha B_0 TE + \phi(t_0)) \left| \frac{d((y - T_0)\gamma\alpha B_0 TE + \phi(t_0))}{dy} \right| \\ =& p_\phi((y - T_0)\gamma\alpha B_0 TE + \phi(t_0)) |\gamma\alpha B_0 TE + \phi(t_0)| \end{aligned} \tag{5.10}$$

This equation yields an exact description of the temperature uncertainty but due its complexity it is difficult to further transform this PDF in the next steps. Empirical observation of the given test data described in Section 5.4 indicates that the shape of $p_\phi(x)$ for small values of $\sigma(R)$ and $\sigma(I)$ can be adequately approximated by a normal distribution. Testing several configurations of μ_R, μ_I, $\sigma(R)$ and $\sigma(I)$ no configuration could be found where $\mu_R > 10\sigma_R$ and $\mu_I > 10\sigma_I$ while $p_\phi(x)$ is not similar to a normal distribution. This indicates that the similarity of $p_\phi(x)$ and a normal distribution holds true more generally. Under this assumption $p_T(x)$ can be similarly approximated because the family of normal distributions is closed under linear transformations. This characteristics allows for the following assumption: If $\tilde{p}_\phi(x) \approx p_\phi(x)$ is a normal distribution $\tilde{p}_T(x) \approx p_T(x)$ because of the linear transformation from ϕ to T described in Equation 2.7. Taking into account the normal PDF Equation 5.3 the parameters of the function $\tilde{p}_T(x) = \mathcal{N}(\mu_T, \sigma_T^2)$ such that the error between the original function $p_T(x)$ and the normal approximation is minimized. According to empirical observation, this seems to be the case when μ_T is equal to the temperature computed by the PRFS method from the measured quantities μ_R and μ_I. σ_T is determined by asserting that $p_T(\mu_T) = \tilde{p}_T(\mu_T)$ and solving for σ_T:

$$\begin{aligned} \mu_T =& T_0 + \frac{tan^{-1}\left(\frac{\mu_I}{\mu_R} - \phi(t_0)\right)}{\gamma\alpha B_0 TE} \\ \sigma_T =& \frac{1}{\sqrt{2\pi} p_T(\mu_T)} \end{aligned} \tag{5.11}$$

5.3.4 Thermal Dose PDF

After deriving the PDF $p_T(x)$ describing the distribution of the temperature T the final thermal dose distribution $p_\tau(x)$ can be derived. In terms of the processing

pipeline shown in Figure 5.1 this includes the transformation of the temperature map into a thermal dose map using the CEM_{43} model.

$$\tau = \sum_{t=0}^{t_{final}} \Delta t \, \beta^{T_t - 43} \tag{5.12}$$

Deriving the thermal dose PDF will be described in two parts. The first part will focus on the derivation of the PDF of a single exponential term of the CEM_{43} model. Afterwards, the sum of the single terms will be used to derive the final thermal dose PDF.

The derivation of the single term PDF is focused on a single exponential term in the sum of probabilistic CEM_{43} given by Equation 5.2. This term can be written as:

$$E = \Delta t \beta^{T-43} \tag{5.13}$$

The derivation is based on the approximated normal distribution described by Equation 5.11 and can be simplified by taking into account the previous assumption that the temperature measurement T is a normally distributed random variable. This causes the otherwise complex formula to become a less complex lognormal distribution because the term $e^{\mu+\sigma X}$ for a standard normal random variable $X \sim \mathcal{N}(0,1)$ is lognormally distributed with its PDF being:

$$\mathcal{LN}(\mu, \sigma^2) = \frac{1}{x\sigma\sqrt{2\pi}} e^{-\frac{(\ln x - \mu)^2}{2\sigma^2}} \tag{5.14}$$

For the derivation of μ_E and σ_E it is necessary to rearrange the exponential term E from the CEM_{43} model into the form $e^{\mu_E + \sigma_E X}$ as explained above. Distributing the leading Δt factor accross the sum to reduce the complexity, the resulting rearranged exponential term E can be written as:

$$\begin{aligned} \Delta t \beta^{T-43} =& \Delta t \beta^{\mu_T + \sigma_T X - 43} \\ =& e^{ln(\Delta t)} e^{ln(\beta)(\mu_T + \sigma_T X - 43)} \\ =& e^{ln(\Delta t) + ln(\beta)(\mu_T - 43) + ln(\beta)\sigma_T X} \end{aligned} \tag{5.15}$$

Taking this rearrangement into account and solving it for μ_E and σ_E it can be concluded that

$$\mu_E = ln(\Delta t) + ln(\beta)(\mu_T - 43) \tag{5.16}$$

$$\sigma_E = ln(\beta)\sigma_T \tag{5.17}$$

which allows the computation of the single exponential term PDF $p_E(x) \approx LN(\mu_E, \sigma_E^2)$.

The final thermal dose PDF $p_\tau(x)$ is obtained by computing the PDF of the sum of all E_t. This is typically done by a chain of convolutions over all $p_{E_t}(x)$. Due to the high computational effort of a convolution, however, this step is approximated to ensure real-time capability. The PDF of the sum of lognormally distributed independent random variables generally resembles a lognormal distribution (Mitchell, 1968). For this reason, the final thermal dose PDF is approximated by $p_\tau(x) = \mathcal{LN}(\mu_\tau, \sigma_\tau^2)$. The parameters μ_τ and σ_τ are obtained using an approach inspired by Wilkinson's cumulative distribution function (Beaulieu et al., 1995). For example, the first two moments m_1, m_2 of the convolution of two PDFs $p_{E_t} * p_{E_{t+1}}$ are computed by:

$$m_1[p_{E_t} * p_{E_{t+1}}] = m_1[p_{E_t}]\, m_1[p_{E_{t+1}}], \tag{5.18}$$

$$m_2[p_{E_t} * p_{E_{t+1}}] = m_2[p_{E_t}] + 2\, m_1[p_{E_t}]\, m_1[p_{E_{t+1}}] + m_2[p_{E_{t+1}}]. \tag{5.19}$$

Analogously, the moments for the convolution of all E_t can be computed. After matching the first moments according to:

$$m_1[p_\tau] = m_1[p_{E_0} * ... * p_{E_{t_{final}}}],$$
$$m_2[p_\tau] = m_2[p_{E_0} * ... * p_{E_{t_{final}}}],$$

the parameters of the thermal dose PDF are computed by:

$$\mu_\tau = 2\, ln(m_1[p_\tau]) - \frac{1}{2}\, ln(m_2[p_\tau]) \tag{5.20}$$

$$\sigma_\tau = \sqrt{ln(m_2[p_\tau]) - 2\, ln(m_1[p_\tau])}, \tag{5.21}$$

5.3.5 Probabilistic Necrosis Map Computation

In conventional necrosis maps derived from the CEM_{43} model, a necrosis threshold θ is applied to the thermal dose to determine if the underlying tissue is necrotic. This yields a binary necrosis map.

In the probabilistic case, the same threshold θ can be applied to the thermal dose PDF in order to determine the probability of necrosis. This yields a necrosis map

with real values between 0 and 1. The probability of necrosis $P(N)$ is computed as the integral over $p_\tau(x)$ from θ to infinity written as:

$$P(N) = \int_{\theta}^{\infty} p_\tau(x) dx. \tag{5.22}$$

$P(N)$ is computed for every pixel. The resulting probabilistic necrosis map can be visualized to provide information about the current ablation zone. An example of a probabilistic necrosis map is shown in Figure 5.2.

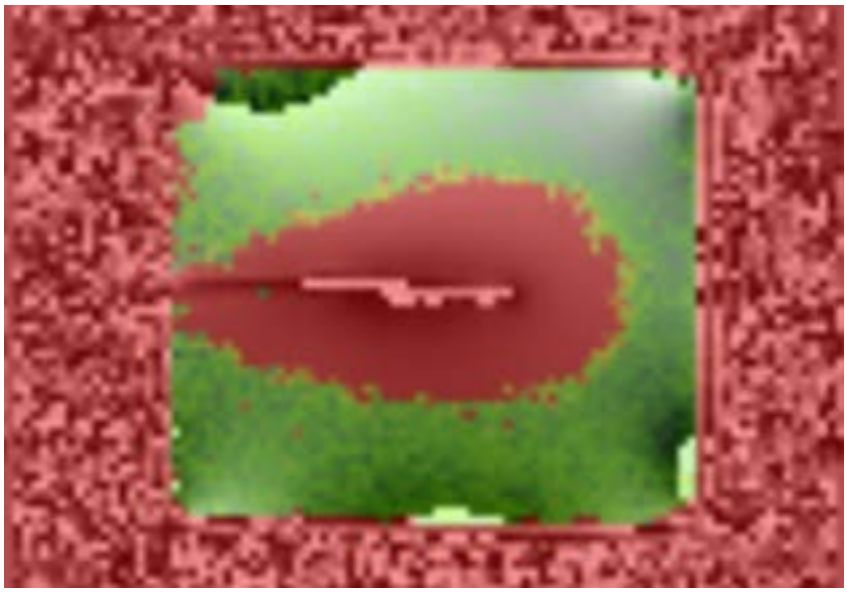

Fig. 5.2: Exemplary visualization of a probabilistic necrosis map. The data was acquired in a bioprotein phantom without motion. The resulting probabilities are color coded using a traffic light color scheme from 0 (green) to 1 (red).

To quantitatively compare the introduced necrosis map to the conventional one, another threshold ξ is applied. This threshold describes a probability above which necrosis is considered to be certain. It converts the probabilistic necrosis map into a binary form. The optimal value for ξ depends on the MRI parameters and the specific setup of the procedure.

5.4 Experimental Setup

5.4.1 Data Sets

The evaluation was conducted using four data sets. MWA using a MedWaves Avecure (Medwaves, San Diego, CA, USA, 14G) of a polyacrilamide gel phantom was monitored with PRFS-based MR thermometry on a 1.5 Tesla scanner (Siemens Avanto, Siemens Healthineers, Germany) using a single-echo single slice 2D spoiled GRE sequence (TE = 9.56ms, TR = 20ms, slice thickness = 4mm, bandwidth = 260Hz/Px, flip angle = 12°, FOV = 192x192mm^2, matrix size = 96x96). 30 reference images were recorded before the start of the treatment. All 140 subsequent images record the emulated ablation procedure.

3D T2-weighted imaging (TE = 385ms, TR = 3200ms, slice thickness = 2.5mm, bandwidth = 780Hz/Px, flip angle = 120°, FOV = 250x250mm^2, matrix size = 256x256, turbo factor = 242), manually segmented by a medical expert, was used as ground truth for the assessment of the ablation zone. This ground truth was scaled down to a size of 96x96 pixel via a Lanczos-Filter with $a = 3$ in order to match the intra-operative data. Finally, the ground truth was cropped to a rectangle as shown in Figure 5.3. This avoids the inclusion of any background noise, allowing for a more meaningful evaluation. Additionally, PRFS-based MR thermometry was performed

Fig. 5.3: A phase image of the phantom data set with the ground truth of the ablation zone (green) and the cropped area to avoid background noise (red).

on a 1.5 Tesla scanner (Siemens Aera, Siemens Healthineers, Germany) in hepatic

MWA of three in-vivo swine using a single-echo single slice spoiled GRE sequence (TE = 9.6ms, TR = 20ms, slice thickness = 3mm, bandwidth = 260Hz/Px, flip angle = 12°, FOV = 512x512mm^2, matrix size: 256x256). 10 reference images were recorded before heat application and subsequently 30 to 49 images were recorded during MWA.

Post-ablative contrast-enhanced (intravenous injection of 0.025 mmol/kg gadolinium ethoxybenzyl diethylenetriamine pentaacetic acid, Primovist, Bayer-Schering Pharma, Berlin, Germany) 3D T1-weighted imaging (TE = 1.2ms, TR = 3.4ms, slice thickness = 2mm, bandwidth = 475 Hz/Px, flip angle = 12°, FOV = 320x240mm^2, matrix: 160x120), manually segmented by a medical expert, was used as ground truth for the assessment of the ablation zone. The images were scaled down to the size 128x128 pixels via a Lanczos-Filter with $a = 3$ to match the intra-operative image data. The final ground truth is then cropped to exclude any background noise while still containing the greatest possible area.

The study was conducted in accordance with the German law for animal protection (TierSchG) and the European Directive 2010/63/EU. All experiments were approved by the local animal ethic committee (Lower Saxony State Office for Consumer Protection and Food Safety, LAVES). The reuse of animals from study 16/2374 was permitted after veterinary examination and demonstration that the animal's general state of health and well-being had been fully restored (18/2987). One female and two male LEWE minipigs (body weight 39.6 kg$\pm$1.7kg, body length 108$\pm$6cm) were used. Anesthesia was induced by intravenous injection of 10mg/kg propofol (Narcofol®, CP Pharma, Germany) via a central line to enable endotracheal intubation. Animals were maintained under general anesthesia using an isoflurane precision vaporizer and mechanically ventilated (air-oxygen mixture 1:1, pIso >1.8 mmHg). The breathing rate was set to 12 breaths per minute and a ventilation volume of 8-10 ml/kg per breath was chosen, based on the EtCO2 (35-45 mmHg) concentration. The depth of anesthesia was continuously monitored and animals received continuous fluid therapy (Ringer's lactate, 10 ml/kg/h). Analgesia was achieved by an initial systemic intravenous dose of 4 mg/kg carprofen (Rimadyl®, Zoetis, US). For liver ablation, 1mg/kg Lidocaine (Xylocain, Aspen, Germany) was locally infiltrated at the needle insertion sites. At the end of the experiment, pigs were euthanized under deep anesthesia by intravenous injection of 15-25 ml/animal of T61 until heart arrest was confirmed.

5.4.2 Statistical Evaluation

The probabilistic model i evaluated by comparing its necrosis maps to the necrosis maps produced by the conventional CEM_{43} model. The goal of this evaluation is less to obtain results that statistically show the superiority of the probabilistic model and more to indicate its feasibility compared to the state-of-the-art. This comparison is done according to the criteria accuracy, robustness, and efficiency.

Accuracy

To compare the two approaches, the probabilistic necrosis map is converted into a binary map by applying a threshold $\xi \in [0, 1]$ to every pixel. Every pixel is classified as either necrotic if its probability of necrosis is bigger than or equal to ξ, or as not necrotic otherwise. The ablation zones predicted by either approach are compared to the ground truth to determine the accuracy. To find the most suitable threshold for the prediction of the ablation zone, this comparison is done for different values of ξ on the phantom data set. The best ξ is used for all subsequent pig liver data sets. To quantify the accuracy, the sensitivity and DSC are used. Furthermore, in order to evaluate the amount of false positives relative to the size of the ablation zone, the false positive rate (FPR) is taken into account. It is computed as the ratio of the amount of false positives and the amount of pixels composing the ablation zone in the ground truth. This measure has the advantage of not depending on the absolute amount of negatives, i.e. the size of the background, contrary to the measure of specificity.

Robustness

Unfavorable measurement circumstances can have a variety of causes. In this evaluation the quantity considered to represent random uncertainties is the SNR. The SNR of R and I correlates with the overall precision of the MRI measurements that are the foundation of the thermal dose model. It is computed as:

$$\text{SNR}_R = \left(\sum_{x,y}^{WH} \bar{r}_{x,y} \right) / \left(\sum_{x,y}^{WH} \sigma_{Rx,y} \right) \tag{5.23}$$

$$\text{SNR}_I = \left(\sum_{x,y}^{WH} \bar{\imath}_{x,y} \right) / \left(\sum_{x,y}^{WH} \sigma_{Ix,y} \right), \tag{5.24}$$

where W and H are the width and the height, respectively, $\bar{r}_{x,y}$ and $\bar{\imath}_{x,y}$ are the sample mean of the real and the imaginary value for each pixel, and $\sigma_{Rx,y}$ and $\sigma_{Ix,y}$ are the standard deviations for each pixel. To determine the overall robustness, the accuracy of the conventional and probabilistic necrosis maps is measured while varying the SNR. For this purpose, increasingly intense Gaussian noise is introduced into the complex images. The accuracy is measured as described in the previous paragraph, with ξ set to the value giving the best possible accuracy for the first data set. This includes the comparison of the ablation zones predicted by both necrosis maps to the ground truths with respect to the sensitivity, the FPR, and the DSC. As artificially lowering the SNR renders the pig liver data sets unusable due to their comparatively low initial quality, the overall computation of the robustness is, as opposed to the computation of the accuracy, only performed for the phantom data set. The introduction of Gaussian noise only mimics the effects of a decreasing SNR. Therefore, this study does not evaluate the model's robustness for a varying MRI measurement error realistically. Still, due to the MRI measurement error for the real and imaginary image being Gaussian in nature (Gudbjartsson et al., 1995), it can be expected that the results of this study closely resemble those obtained by a more realistic evaluation.

Efficiency

The duration of the computation of a probabilistic necrosis map is measured. This duration does not include the time it takes to compute σ_R and σ_I nor the time it takes to obtain a new image from the MR apparatus and load it into the RAM of the computer. These are equal for any PRFS-based MR thermometry and thus do not allow any conclusions about the real-time capability of the probabilistic CEM_{43} model. As the computations made for every pixel are the same regardless of the data set, the performance is, similar to the robustness, only evaluated for the phantom data set.

5.5 Results

5.5.1 Accuracy

First, the accuracy of the CEM_{43} necrosis map was measured with respect to the phantom data set. The ablation zone was predicted with a sensitivity of 1, an FPR

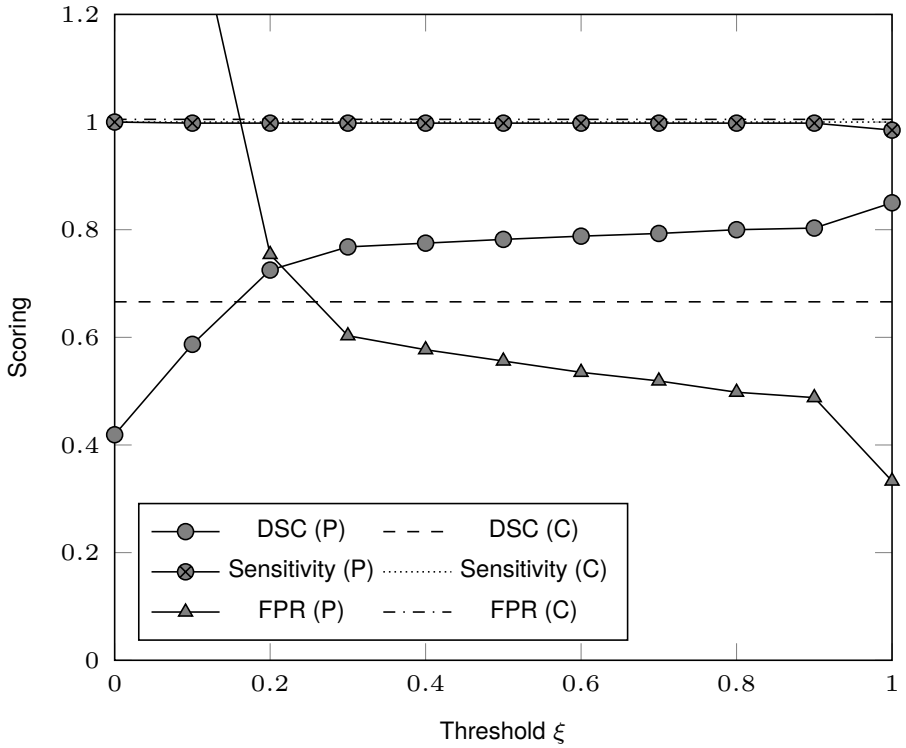

Fig. 5.4: The DSC, the sensitivity, and the FPR of the probabilistic necrosis map (P) for different ξ compared to the conventional necrosis map (C) applied to the phantom data set. The graph of the sensitivity of the conventional model is hidden behind the graph of the sensitivity of the probabilistic model and has a constant value of 1.

of 1.005 and a DSC of 0.666. The same measurement was then performed multiple times for the probabilistic necrosis map for different ξ. The results show a DSC bigger than 0.666 for $\xi \gtrsim 0.16$, with a maximum of 0.85 at $\xi = 1$; a sensitivity being close to 1 for all ξ with a minimum of 0.985 for $\xi = 1$; and a FPR being smaller than 1.005 for $\xi \gtrsim 0.18$ with a minimum of 0.333 for $\xi = 1$. These results can be seen in Figure 5.5. The dashed lines represent the DSC, the sensitivity, and the FPR of the conventional necrosis map. The one representing the sensitivity of the conventional necrosis map is occluded by the solid line representing the sensitivity of the probabilistic necrosis map and has a constant value of 1. Evidently, the lowest FPR (0.333) and the maximum DSC (0.85) are obtained for $\xi = 1$. The ablation zones predicted by the conventional and probabilistic model are shown in Figure 5.5. Note, that here $\xi = 1$ is equivalent to $\xi > 1 - \mathrm{MP}$, where MP is the machine precision limit for a 32-bit floating point number, i.e. 1.175494×10^{-38}.

Furthermore, the accuracy was determined with respect to the pig livers. As $\xi = 1$ has been determined to yield the best results, this value was used to compute the

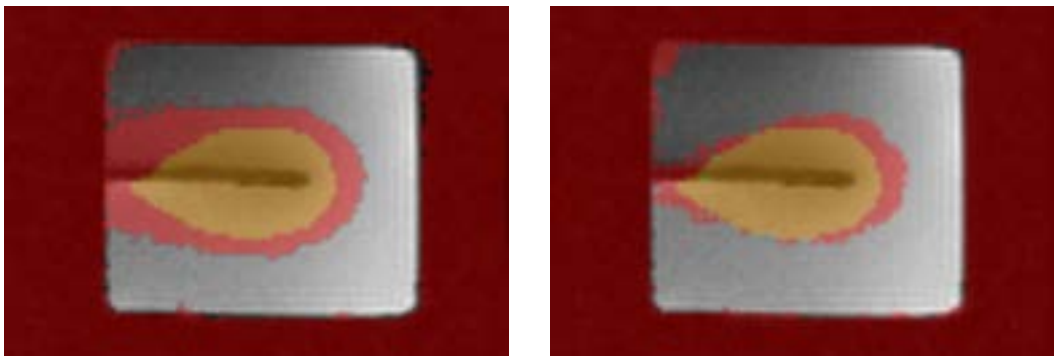

(a) Conventional CEM_{43} model. **(b)** Probabilistic CEM_{43} model.

Fig. 5.5: Magnitude images of the phantom data set with the ablation zones predicted in red and the groundtruth in yellow / green.

probabilistic necrosis maps for the other three data sets. The results for the pig livers showed a higher DSC for the probabilistic necrosis map compared to the conventional model: The differences between the scores of the probabilistic and the conventional necrosis maps are ~ 0.1, ~ 0.04, and ~ 0.072 for data sets two, three, and four, respectively. Additionally, the conventional necrosis maps provided a higher sensitivity than the probabilistic approach: The differences between the scores of the probabilistic and the conventional necrosis maps are ~ -0.023, ~ -0.128, and ~ -0.141 for data sets two, three, and four, respectively. Also, the results for the pig livers showed a lower FPR for the probabilistic necrosis map compared to the conventional model: The differences between the scores of the probabilistic and the conventional necrosis maps are ~ -0.256, ~ -0.692, and ~ -1.422 for data sets two, three, and four, respectively. The ablation zones predicted by the conventional and probabilistic model for dataset three are shown in Figure 5.6. All results regarding the differences in DSC, sensitivity, and FPR can be seen in Figure 5.7.

5.5.2 Robustness

The robustness of the conventional and probabilistic necrosis map was evaluated by measuring the dependency of their accuracy on the SNR.

Both the conventional and the probabilistic necrosis map were evaluated. A baseline SNR of 6.214 for the real and 6.501 for the imaginary components of the complex image acquired by the MRI apparatus was measured. The SNR was evenly decreased in steps of 0.5 by introducing Gaussian noise to measure the influence on the accuracy. For the conventional necrosis map, the accuracy of the ablation zone prediction varies according to Figure 5.8. In general, the DSC decreases with

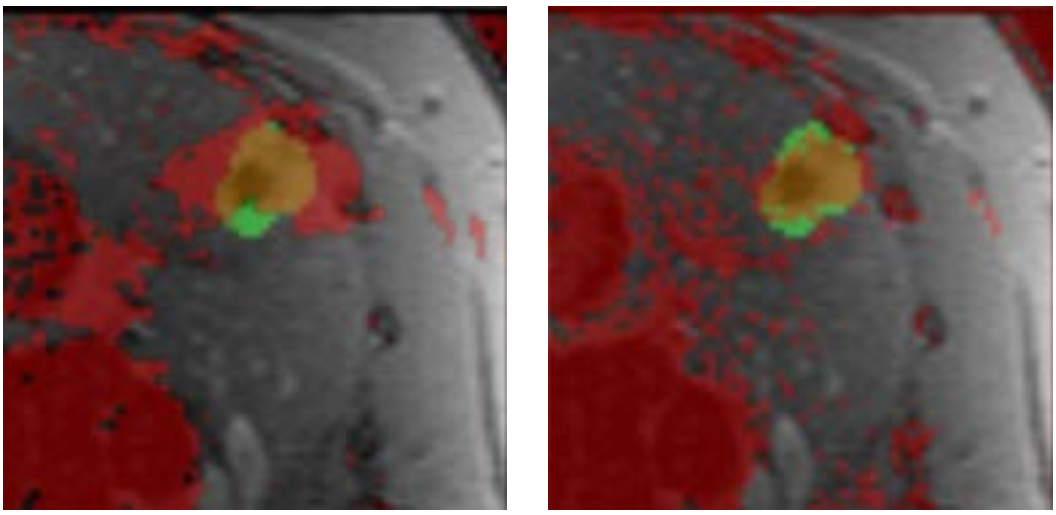

(a) Conventional CEM_{43} model. **(b)** Probabilistic CEM_{43} model.

Fig. 5.6: Magnitude images of the second pig liver data set with the ablation zones predicted in red and the groundtruth in yellow / green.

decreasing SNR showing a maximum value of 0.666 for the original data and a minimum value of 0.419 for an SNR decrease of 6.0. The sensitivity has a value of 1.0 for any change in SNR. The FPR increases with a decreasing SNR having a minimum of 1.005 for the original data and a maximum of 2.771 for an SNR decrease of 6.0.

The change in accuracy for the prediction of the ablation zone by the probabilistic necrosis map was evaluated similarly. The measurements show a decrease in accuracy, as can be seen in Figure 5.8. The DSC with decreasing SNR having a maximum of 0.85 for the original data and a minimum of 0.428 for an SNR decrease of 6.0. The sensitivity was measured to be close to 1.0 for any decrease of the SNR with its minimum being 0.96 for an SNR decrease of 5.0. The FPR increases with a decreasing SNR having a minimum of 0.333 for the original data and a maximum of 2.673 for an SNR decrease of 6.0.

5.5.3 Efficiency

The performance was measured in terms of the duration for computing the probabilistic necrosis map. This duration only includes the computations from the complex image to the probabilistic necrosis map, as loading times of the images are the same for any thermal dose estimation algorithm and are thus not characteristic for this model. The computation of 140 necrosis maps for images with a resolution

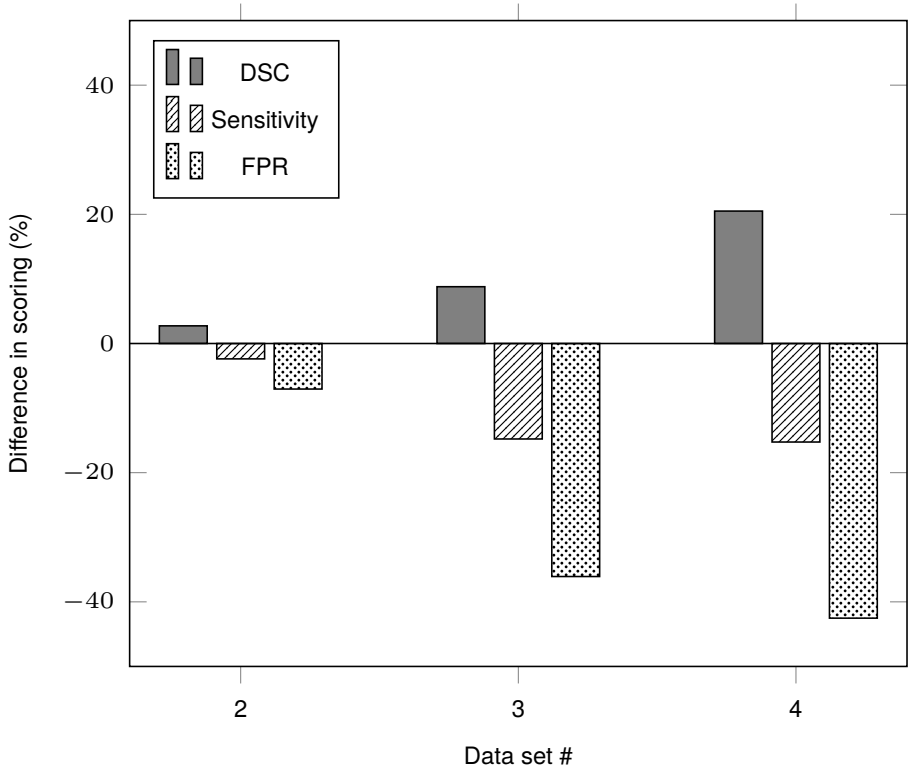

Fig. 5.7: The relative differences in scoring for the three pig data sets when comparing the probabilistic with the conventional approach. Scores displayed are the DSC, the sensitivity, and the FPR

of 96x96 pixels was performed in 89.215s. Therefore, the mean duration for the computation of a probabilistic necrosis map is 0.637s per image with a standard deviation of 0.0002s.

5.6 Discussion and Conclusion

As can be concluded from the results and existing results (Yung et al., 2010), CEM_{43} necrosis maps often overestimate the size of the ablation zone. A more accurate estimate would therefore necessitate a higher threshold for classifying a pixel as necrotic to make the ablation zone smaller. For this reason, a probabilistic necrosis map with a large probabilistic threshold ξ would produce better results compared to the conventional approach. Correspondingly, a threshold of $\xi = 1$ results in the highest accuracy for the probabilistic necrosis. Next to the intersection of union, the DSC is an established measure for determining the overlap of the predicted and the true ablation zone. As this measure scores higher for all four data sets,

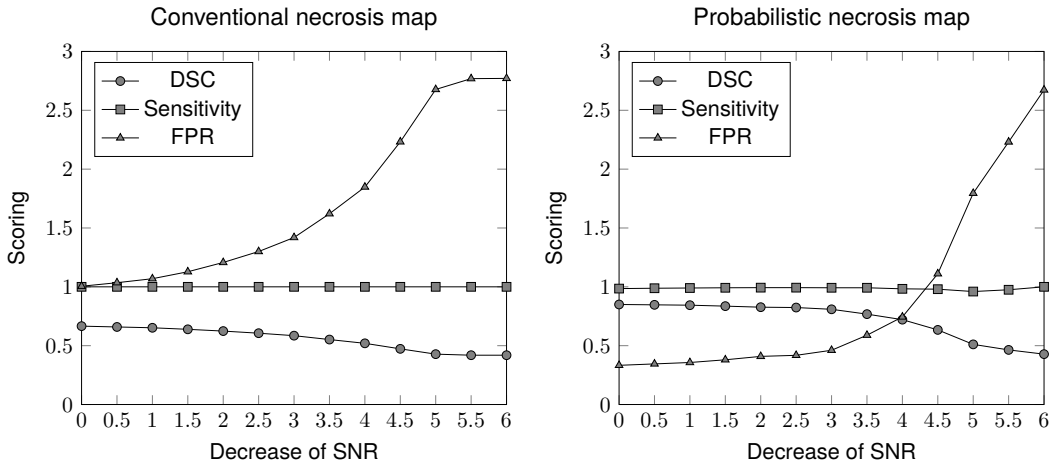

(a) Conventional CEM_{43} model. **(b)** Probabilistic CEM_{43} model.

Fig. 5.8: The DSC, the sensitivity, and the FPR for the conventional necrosis map and the probabilistic approach in comparison. The results are observed with respect to changes in the SNRs.

the probabilistic ablation zone seems to generally perform better in predicting the ablation zone than the conventional necrosis map. The difference in the scoring is largest in the first data set (phantom), which has the best acquisition conditions out of all four data sets. More investigation could give an indication as to whether this difference in scoring is related to the image quality. The sensitivity of the probabilistic necrosis map is lower throughout all data sets, even if it gets close to the sensitivity of the conventional necrosis map (difference smaller than 0.1) for the phantom and first pig data set. This can be explained by the overestimation of the ablation zone by the conventional model. A larger ablation zone has less false negatives and therefore a higher sensitivity. This, however, comes at the cost of more false positives. With the main issue in the conventional approach being too many false positives resulting in premature abortion of the treatment, the underestimation by the probabilistic approach as indicated by the lower sensitivity is usually less harmful. Too many false negatives only become an issue close to risk structures as pixels might not be classified as necrotic even if they are, which could result in unintentional damage to healthy tissue. Utilizing the standard deviation of the thermal dose PDF, the uncertainty close to these structures could be evaluated. This would allow the indication of possible false negatives close to risk structures. The FPR of the probabilistic necrosis map is better than the conventional necrosis map for all data sets. This score is arguably more important than the sensitivity, as the false positives are the reason for incomplete tumor treatment. The lower sensitivity and lower FPR indicate that the probabilistic necrosis map with $\xi = 1$ estimates a smaller ablation zone compared to the conventional necrosis map. As

the conventional model generally tends to overestimate ablation zones, this might yield a more accurate estimate. A smaller predicted ablation zone can also help prevent premature ablation terminations. Furthermore, ξ can be set to a smaller value to increase the size of the ablation zone and subsequently increase the sensitivity, if necessary. The parameter could also be adjusted dynamically based on the operators experience or by machine learning algorithms based on training data.

The sensitivity of both necrosis maps is close to 1.0 for any SNR indicating an overestimation of the ablation zone due to noise pushing the thermal dose values above the necrosis threshold. Random fluctuations observed for the probabilistic necrosis map can be traced back to an inaccurate estimation of σ_R and σ_I. Additional Gaussian noise is applied to all images except for the reference images, which determine the estimate of the standard deviations. Therefore, the estimate of the standard deviations is lower than their true value as additional noise increases the variance of the data. This inaccuracy results in inaccurate PDFs and thus results in an inaccurate prediction of the ablation zone. The FPR of both necrosis maps increases as the SNR decreases. This is caused by the Gaussian noise randomly pushing the thermal dose in pixels over the necrosis threshold, which then results in false positives. Again, the probabilistic necrosis map has better FPR values for any SNR decrease when compared to the conventional necrosis map. This can be explained by the different types of necrosis thresholds for the two methods. The conventional necrosis map computes scalar thermal dose values for each pixel, which have to exceed the necrosis threshold in order to be classified as necrotic. Therefore, a single time step with a random spike in the temperature is enough to classify a pixel as necrotic. The probabilistic necrosis map, however, classifies pixels as necrotic only if the probability of the underlying tissue being necrotic exceeds a certain threshold. As this threshold was chosen to be $\xi = 1$, almost 100% of the area under the thermal dose PDF must be right of the necrosis threshold for a positive classification. Having a thermal dose high enough for this to happen is more unlikely than having a thermal dose above the necrosis threshold. Therefore, the probabilistic necrosis map classifies less pixels as necrotic and thus contains less false positives. All in all, the probabilistic necrosis map predicts the ablation zone more accurately than the conventional necrosis map for any SNR decrease. This indicates a higher robustness of the probabilistic approach to random noise when compared to the conventional CEM_{43} model, which may be of additional advantage in interventional MRI where noise may be increased by electromagnetic interference of the interventional devices. To conclusively show an overall higher

robustness, however, more research with different types of noise and artifacts needs to be conducted.

According to the results the computation of the probabilistic necrosis map can be performed in real-time and is thus practically feasible during ablation procedures. Still, the current means used to compute the necrosis map are not optimized in terms of memory management and GPU shaders. Re-implementing the algorithms in C++ instead of the current C# language would allow for faster overall memory management. Furthermore, in the current implementation, large chunks of the software, which could be run on the GPU, are still executed on the CPU. Offloading this code to the GPU would yield a performance increase and could allow the algorithms to run in real-time especially for high resolution images. Even though the model derived and evaluated in this Chapter shows promising results, many features could still be implemented to further increase the predictive power with respect to accuracy, robustness, and efficiency. One example of this is the integration of other sources of errors, which can be considered by the probabilistic nature of the model. This includes, for instance, the consideration of known MRI artifacts that can be detected with image processing software. A subsequent adjustment of σ_R and σ_I according to the character of these artifacts could further improve the robustness of the model.

Also, as the sample size of the presented evaluation was too low, the results of this method need to be validated in a larger cohort. A real time evaluation during an ablation procedure could be the next step towards a general deployment of this model during MR-guided ablation surgeries. Even though the present Chapter is focusing on the prediction of ablation zones and the probability distribution of the thermal dose, other quantities such as the magnitude could also be investigated through a similar probabilistic approach, extending this model to more than only temperature-related quantities. The same mathematical tools used for the estimation of the thermal dose distribution can be used to estimate other randomly distributed quantities. An extension of this model to other unrelated MR-imaging tasks is therefore possible. Furthermore, an empirical investigation of relationships between error distribution character and quantities like blood perfusion and attenuation coefficients can be conducted through simulations. This allows the derivation of probability density functions without a priori knowledge about the error source. Simulations of Penne's bioheat transfer equation (Pennes, 1948) could be used for this task. Moreover, adding the probabilistic methodology of this model to current real-time simulation approaches (J. Zhang et al., 2021; Mariappan et al., 2017; He et al., 2016; Carluccio et al., 2013) could give additional information about error bounds and confidence intervals of the ablation zone.

In the evaluation, ξ was determined by the ablation zone prediction with the best accuracy for the phantom data set. However, as this ξ is a parameter that represents all hidden parameters specific to any MRI setup, applying the same ξ to data sets acquired under different conditions will likely yield less-than-ideal results. Optimal calibration of ξ would therefore require the evaluation of a pre-operative data set with a pre-operative ground truth. This would be a time-consuming and cumbersome task. Alternatively, the empirical relationships between ξ and parameters, such as the magnetic field strength, and the ablation temperature could be investigated to derive mathematical models for an optimal calibration.

In conclusion, this Chapter derives a probabilistic thermal dose model for the prediction of ablation zones during thermal ablation procedures based on the CEM_{43} thermal dose model. The model estimates the probability distribution of different quantities within the MRI processing pipeline and the probability of ablation. A subsequent empirical evaluation of this model with a polyacrylamide gel phantom and three in-vivo pig livers indicates a more accurate prediction of ablation zones compared to the conventional CEM_{43} model in the majority of cases. The ablation zones predicted by the probabilistic necrosis maps are smaller than the ablation zones predicted by the conventional approach. As the probabilistic necrosis map generally has a lower rate of false positives it can help prevent premature ablation termination. Furthermore, the results show a higher accuracy of the probabilistic necrosis map independent of the intensity of random noise. This indicates a higher robustness against noise. Also, the new probabilistic model is feasible for real-time application during ablation procedures.

6 Adaptive Bio Heat Transfer Simulation

About this chapter

Parts of this chapter have been published in: Julian Alpers, Maximilian Rötzer, Marcel Gutberlet, Frank Wacker, Bennet Hensen, and Christian Hansen (2022). “Adaptive Simulation of 3D Thermometry Maps for Interventional MR-guided Tumor Ablation using Pennes’ Bioheat Equation and Isotherms”. In: Scientific reports, 12.1 (2022): 1-11. The methods described were implemented by Maximilian Rötzer as part of a Master’s Thesis project supervised by the author of this thesis.

6.1 Introduction

> *Theory provides the maps that turn an uncoordinated set of experiments or computer simulations into a cumulative exploration.*
>
> — **David E. Goldberg**
> Computer scientist and former professor

In both hypothermic and hyperthermic treatment methods, the severe deviation from the normal range of body temperature can induce coagulation necrosis or apoptotic cell death. Successful clinical treatment requires complete destruction of tumor tissue while sparing healthy tissues and risk structures (e.g., vessels). Precise adherence to the planned ablation zone plus safety margin is essential, also to prevent re-growth of the tumor locally. A disadvantage of minimally invasive treatment is the lack of a line of sight to monitor ablation progress. During the intervention, MRI offers the possibility to measure the temperature changes inside the tissue. Using a volumetric thermometry map, which provides real-time information about the temperature distribution in the target tissue, radiologists could estimate the extent of the necrosis zone and then schedule the ablation process in a timely manner. Unfortunately, the direct development of an MRI thermometry map that fully covers the required 3D space is accompanied by complex problems, such as an inhomogeneous magnetic field or the time required. One approach to overcome these problems is to use an interventional simulation of the ablation process. A simulation, which is adapted to patient- and intervention-specific and intervention-specific conditions, can be achieved by optimizing the underlying model with data measured in real time.

Contribution. In this Chapter, a new method for volumetric heat map generation is introduced, which can be applied during minimally invasive tumor ablation. Pennes' BHTE is updated based on 2D thermometry maps acquired during ablation. Because these maps are rotated around the applicator's main axis, the full heat profile is always visible, and the simulation is not restricted to a specific heat source term and can be applied to all ablation techniques. The initial setting chosen for the fitted parameters is of little to no consequence as they subsequentially get optimized by minimizing the sum squared error between isotherms extracted from the 2D maps and the current 3D simulation. Evaluation shows promising results of up to 0.88 ± 0.04 similarity to a manually extracted ground truth, while also being robust towards outliers and applicable to a wide range of clinical setups.

6.2 Related Work - Bio Heat Transfer Simulation

Johnson and Saidel (2002) began research in the field of interventional and adaptive simulation in 2002 by analyzing 3D simulation for thermal processes and conducting one of the first theoretical studies. Based on their work, they and other researchers (Roujol et al., 2011; Todd et al., 2010) came to the same two conclusions. First, a continuous simulation of the heat distribution is able to increase the spatial resolution of a volumetric ablation monitoring. Second, a biological heat model is capable of aiding the real-time process of interventional radiology.

The major novelty in the present chapter is the development of an adaptive simulation utilizing the easy to compute Pennes' BHTE. This equation, while easy to compute, is very prone to measurement errors. By utilizing the sequence protocol introduced in Chapter 3 the live data can be fed to the algorithm to adapt the simulation parameters live during the procedure. Hence, the accumulated error can be minimized and the overall accuracy of the simulation can be improved. To get a proper overview of the existing methods an initial unstructured literature research was conducted focusing on thermal simulation procedures in general. Based on the results, frequently used phrases and synonyms where identified and collected to define a proper search term. Regarding the topic of adaptive simulation, the term was divided into four major categories, also observable in Table 6.1:

1. Again the dimensionality of the simulation is meant to be volumetric. Therefore, the search term should yield as few as possible results regarding pure 2D simulations.

2. The approach used for simulation of the thermal distribution. This can either be a bio heat transfer like Penne's BHTE or other approaches like (extended) Kalman filters.

3. The continuity is one of the major factors in this chapter. The simulation shall be performed in real time to ensure that the information is available during treatment with as less as possible delay after image acquisition.

4. Only heat maps of any kind will be considered during the literature research.

After definition of the presented categories a structured literature research was performed for the last ten years from 01.01.2012 to 31.07.2022 on PubMed. Connecting the columns in Table 6.1 with logical AND operations and including the date range the following search term was created:

((3D[Title/Abstract] OR volumetric[Title/Abstract] OR volume[Title/Abstract] OR three dimensional[Title/Abstract] OR 3 dimensional[Title/Abstract] OR three-dimensional[Title/Abstract])

AND

(simulation[Title/Abstract] OR bio heat transfer[Title/Abstract] OR Penne's[Title/Abstract] OR Pennes[Title/Abstract] OR BHTE[Title/Abstract] OR Kalman[Title/Abstract] OR EKF[Title/Abstract])

AND

(live[Title/Abstract] OR adaptive[Title/Abstract] OR realtime[Title/Abstract] OR real-time[Title/Abstract] OR real time[Title/Abstract] OR interventional[Title/Abstract] OR intra-operative[Title/Abstract] OR intraoperative[Title/Abstract] OR continous[Title/Abstract])

AND

(heat[Title/Abstract] OR heat map[Title/Abstract] OR heatmap[Title/Abstract] OR thermometry[Title/Abstract] OR heat distribution[Title/Abstract])

AND

(2012/1/1:2022/7/31[pdat]))

Tab. 6.1: Synonyms for the literature research regarding adaptive simulation approaches. The categories can be divided into "Dimensionality", the used "Approach", the "Continuity" of the approach and the "Type of Map".

Synonym	Dimensionality	Approach	Continuity	Type of Map
1	3D	simulation	adaptive	heat map
2	volumetric	bio heat transfer	realtime	heatmap
3	volume	Penne's	real-time	thermometry
4	three dimensional	Pennes	real time	heat distribution
5	three-dimensional	BHTE	interventional	—
6	—	kalman	intra-operative	—
7	—	EKF	intraoperative	—
8	—	—	continuous	—

This search term yields 56 results, which are analysed in a first title/abstract research. Considered for a more detailed analysis where 21 papers dealing with the topic of simulation of thermal distributions. Those papers were analysed in more detail

performing a full paper research. All papers describing a simulation of the heat distribution during the a thermal procedure where included resulting in just two relevant papers. Excluded from this literature research are all additional papers, which only address simulations used for planning without the use of live data input during the intervention. In the last step, additional relevant papers not appearing in the search term but already known by the author of the present thesis where included in this chapter. The majority of those papers describe basic simulation approaches, which highly influenced the design of the method presented in this chapter. Therefore, these papers may also describe simulation for planning purpose.

Another way to tackle this problem is through the use of control algorithms to determine the value of one parameter. A rather simple control algorithm has been developed by Enholm et. al (2009). Their aim was to adjust the duration of irradiation during a HIFU intervention. Orthogonal to a focused ultrasound beam, concentric circles were used to set temperature limits to which the ablation could maximally reach. These values were determined by a pre-interventional simulation in which the optimal irradiation was calculated. Temperature-sensitive MRI data using the PRFS method provide feedback on whether the voxels lying on the circle have reached the target temperature or thermal dose. If so, irradiation continues in a different area. Quesson et. al (2002), on the other hand, did not focus on the duration, but rather on the intensity of the focused ultrasound irradiation. In addition, they aimed at maintaining a predefined temperature profile. In contrast to Enholm et al. (2009), the calculation of the simulation is performed in real time during the intervention. This is possible by a simplified description of the equation in frequency space. The Fourier transformed equation can be thereby solved with an algebraic expression and the heat radiation amplitude can be found. Together with the MRI-generated heat maps, a control loop can again be implemented. The position of the applicator and tissue or perfusion parameters are determined prior to ablation using reference images and then assumed to be constant during the whole intervention. Nonetheless, control algorithms are also capable of adjusting more than one parameter at a time. Mougenot et. al. (2009) transferred the problem of coefficient determination for BHTE to the field of control engineering. They compared the temperature distribution of a HIFU simulation θ with a sequence of MRI heat maps T in a dynamic control loop. The difference between the target temperature T and the actual measured temperature θ was minimized based on the design of a PID controller. This control algorithm takes into account both the current temperature difference and its time derivative, as well as the accumulation of the error over the past time steps. By coupling the controller with the solution of the heat equation in Fourier space, they were able to determine the values of ultrasound absorption, heat diffusion, and

perfusion. The optimization with the help of an algorithm for the multidimensional search of the local minimum was carried out by iterative calculation of the heat equation with modified tissue parameters. The evaluation of the approach resulted in a real-time, accurate determination of the parameters with little dependence on noise. These properties lead to a fast termination of the algorithm and therefore to the stability of their method. De Bever et al. (2014) developed another method, where a less complex model is used to describe the heat change. The heat input and removal are described by two simple and flexible exponential equations. Their parameters are immediately updated for targeted voxels based on each new MRI measurement. Thus, any change, no matter the physical background, is taken into account. Because of the constant updating, the predictions of heat distribution need to be accurate only until the next measurement is obtained and not for the entire ablation period. Finally, methods of inverse problems can be applied to heat propagation and thus to thermal ablation. In the work of Hafid et al. (2017) it was possible to calculate the propagation of temperatures during cryoablation using a few sensors in the tissue. The thermal behavior during the transition from soft to frozen tissue was integrated into the BHTE, which allowed for the prediction of the movement of the cold front. The most relevant thermophysical coefficients of the model could be obtained by inverse evaluation of the temperature sensor data. Verhaart et al. (2015) also worked with point sensor data, two of which are located in different tissue types. Because they developed their approach on patients rather than simulated data, they were able to determine different diffusion and perfusion values for tumor, muscle, and adipose tissue. Their stimulation of an RF ablation could thus be tailored to different patients and sessions. Fuentes et al. (2010) performed in vivo ablations with the support of a BHTE model adapted to MRI temperature data. MRI slices acquired every five seconds made it possible to track the progress of LITT procedures in real time. By optimizing the complex nonlinear perfusion and diffusion terms, the simulation could be adapted to the interventional data.

The following three approaches are the closest to the one presented in this chapter. In 2011, Funetes et al (2011) show that it is possible to reconstruct missing data for volume reconstruction using the Kalman filter. In their work, they removed data from the images of an MRI-assisted thermal therapy, which were replaced by the BHTE modeled values. With consecutive data corruption below 10 sec, successful recovery was possible. Their research shows, that the BHTE simulation is suitable for the problem of thermal heat propagation simulation but unfortunately, their approach was not meant to be used for interventional simulations of ablation. One year later, de Senneville and Roujol's group (2012) where able to introduce an

approach suitable to improve the accuracy and reliability of MRI thermometry data with respect to the influence of stochastic noise. This is because the calculation of the thermal dose for necrosis determination is highly error-prone at low SNR due to the exponential dependence on temperature. They also made use of an extended Kalman filter to solve the optimization problem. Their approach is usable during the intervention by continuous multi-slice MR measurements. They were able to show a computation time for a whole 3D volume of less than 63.5ms but they need to define all parameter estimations prior to the intervention not providing the possibility to adapt the optimization during runtime. Zhang et al. (2019a) describe a neural network, which is able to formulate nonlinear dynamics of the bio-heat transfer process. Their network needs a fully segmented CT image (fat, bone, liver) in order to compute the different simulations based on the tissue type. Again, their approach is not considering the change in simulation parameters during the process and assumes that these are consistent over the period of the intervention.

An overview of the related work can be seen in Table 6.2.

Tab. 6.2: Summary of the related work. AEKF = Adaptive extended Kalman filter. D = Thermal diffusivity, α = Energy absorption rate. ω = Perfusion. k = Thermal conductivity. FEM = Finite elements method. SAR = Specific absorption rate.

	Temperature Measurement	Treatment	Optimization	Parameter	Model	Discretization	Time [s]
(Quesson et al., 2002)	MRI	FUS	Rearrangement of the algebraic expression	D and α	BHTE	Fourier	180-300
(Enholm et al., 2009)	MRI	HIFU	Binary feedback control	—	—	—	—
(Mougenot et al., 2009)	MRI	HIFU	PID controller	—	BHTE	Rayleigh / Fourier	—
(Fuentes et al., 2010)	MRI	LITT	Adjoint-Newton function	ω and k (non-linear)	BHTE	SAR / FEM	9
(Fuentes et al., 2011)	MRI	LITT	EKF	Mean and covariance of the process$Q$	BHTE	SAR / FEM	9
(De Senneville et al., 2012)	MRI	HIFU	AEKF	Covariance of the Process noise Q	BHTE	Galerkin method	—
(J. d. Bever et al., 2014)	MRI	FUS	Method of least squares	Equation parameter	Simple heat model	—	1
(Verhaart et al., 2015)	Sensors	RFA	Limited, nonlinear optimization function	ω and k	BHTE	SAR / CAD-software	—
(Hafid et al., 2017)	Sensors	Cryo	Levenberg-Marquardt	ω and k	BHTE	FEM	30
(J. Zhang et al., 2019a)	Sensors	HIFU	Cellular neural network	—	BHTE	—	<1
This chapter	MRI	MWA	Levenberg-Marquardt	D and T_{max}	BHTE	FDM	1.05±0.26

6.3 Material and Methods

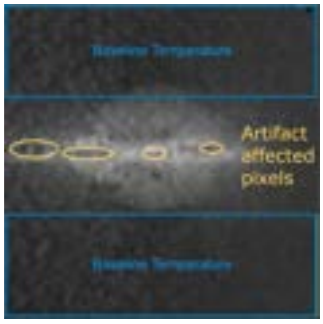

(a) Thermometry map including artifacts and baseline temperature. Gray values correspond to temperature values.

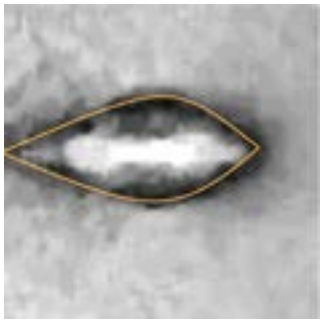

(b) Pathfinding map to determine the path of lowest costs.

(c) Eight extracted isotherms within a range of 24°C color-coded on a grey-scale. The highlighted yellow isotherm corresponds to 21°C.

Fig. 6.1: The thermometry map is converted into a pathfinding map encoding the computed costs of each pixel along the path. Afterwards, the isotherms are extracted by providing the temperature of interest as an input. No color-coding is applied in the thermometry map for better visibility of baseline temperature (background temperature without any heating) and artifact affected pixels (within and around the needle axis caused by signal cancellation and air). For the pathfinding map darker areas depict regions of low cost for the path finding algorithm. Yellow = Extracted isoline.

Many of the related works utilize a mathematical model to simulate the ablation procedures. The prerequisite for clinical use is intervention-specific modeling, which includes both spatial and temporal adjustment of the coefficients. This is because the parameters are not only temperature-dependent and change in the course of the ablation, but different tissue and material types require a separate treatment. In addition, the needle not only acts as an energy source, but its material itself interacts with the emitted heat, which in turn shapes the pattern of heat distribution. Also, more complex geometries of the needle (e.g., in MWA) require special modeling (Deshazer et al., 2017). The consideration of so many physical interactions may lead to complex differential equations with many coefficients. In an interventional setup, these equations must be solved at each time step, and the set of parameters must be optimized regularly. The difficulty here is in reconciling the complexity and the resulting increased accuracy of the computation with a real-time capability.

Therefore, the method aims to reduce the mathematical problem to a diffusion process. Hence, the approach to the modeling of heat distribution shifts from the consideration of a physical optimization problem to the consideration of an optimization problem in computer vision. In the following concept, the goal is not to

describe an internal physical process as best as possible, but to extract suitable information from 2D thermometry data in order to map it to a 3D simulation. The measured data thus only adjust the progress of the ablation, while their values themselves are not included in the simulation.

6.3.1 Isothermal Filter

The data set presented in Chapter 3 is used as an input for the developed adaptive simulation. Because of the uniform distribution around the main axis of the applicator the current heat profile can be observed in every image acquired and the location of the applicator artifact (heat source) is always known. Using this information, no mathematical term for a treatment specific heat source needs to be introduced in the equation because the heat profile directly correlates with the heat source distribution. The thermometry maps are characterized by noise and artifacts caused by the applicator. The inter-dependency between the applicator and MRI magnetic field may result in complete erasure or distortion of thermal information around the applicator. Furthermore, the major part of the measured 2D data consists of the baseline temperature of the non heated parts in the phantom (see Fig. 6.1). To overcome the image corruption problem and to compress the information, the maps are filtered by extracting isotherms. By placing the data in a relative relationship to a reference point, the determination of the isotherm is more robust against noise. This can be done by using Equation 6.1:

$$D_i = |T_i - T_{iso}| \forall i \in N \tag{6.1}$$

with D_i referring to the temperature deviation between the temperature iso-value T_{iso} and the measured temperature T for all pixel N in the image. The idea is that the fluctuations around the isovalue are considered only in the context of the total displacement. By adding up these positive and negative deviations in the calculation of the total distance, the stochastic noise can be eliminated. The global minimization of the Gaussian-distributed noise in the acquired data results in a path that follows temperature of interest. An example of the relative temperature distribution can be seen in Fig. 6.2.

The implementation used in the presented method is based on Dijkstra's algorithm (Dijkstra, 1959). In the case of the isothermal filter the path can be forced only in the direction of the needle axis. In this way, outliers in the data are also robustly removed. Only directly connected pixels with values close to the thermal isovalue generate a path with low cost.

(a) Absolute temperature map.

(b) Relative temperature cost map with a reference value of 25°C.

(c) Relative temperature map with a reference value of 35°C.

Fig. 6.2: The absolute temperature map is color-coded using an iron heat color scale. The relative temperature maps for 25°C and 35°C are gray-scale with the same window/level settings. Note, that by shifting the reference value the corresponding relative temperature values also narrow down.

6.3.2 Adaptive Pennes' Bioheat Simulation

A widely used mathematical model for studying the heat transfer in biological tissue is given by Pennes' BHTE (Pennes, 1948; Wissler, 1998):

$$\rho(T)c(T)\frac{\partial T(t)}{\partial t} = \underbrace{\nabla(k(T)\nabla T(t))}_{\text{Diffusion Term}} + \underbrace{w_b c_b(T_a - T(t))}_{\text{Perfusion Term}} + Q_m(t) + Q_r(t) \tag{6.2}$$

where ρ, c and k are the tissue density, tissue specific heat capacity and tissue thermal conductivity. The perfusion term consists of w_b, the blood perfusion rate, c_b, the blood specific capacity and T_a, the temperature of the arterial blood. Q_m describes the metabolic heat generation rate, Q_r the regional heat source and T represents the temperature at a given time point t. Regarding the density of blood itself ρ_b there are different approaches. Some authors like Bourantas et al. (2019) treat the blood density individually in the simulation term. Other authors like Zhang et al. (2019b) do not report the blood density in their optimization term because it is indirectly included in the blood perfusion rate w_b. In the proposed method the example of Zhang et al. (2019b) is followed and ρ_b is considered to be already included in the perfusion rate.

To utilize the Pennes' BHTE, the position of the heat source must be identified within every acquired 2D image. Because the images are rotated around the applicator's main axis the heat source must be located on this axis as well. In addition, the simulation problem is broken down from a mathematical model to a diffusion process. Therefore, $Q_r(t)$ in Eq. 6.2 can be set to 0 for all voxel outside the applicator's main

axis. The BHTE, a parabolic partial differential equation, can be physically described as a non-homogeneous heat equation. In addition to the homogeneous part of the diffusion, it consists of positive and negative heat sources, which have no spatial or temporal derivative. By combining and rearranging the terms and coefficients, it can be reduced to the following general equation:

$$\begin{aligned} \frac{\partial T(\overrightarrow{\boldsymbol{x}},t)}{\partial t} &= D \cdot \nabla^2 T(\overrightarrow{\boldsymbol{x}},t) + P(\overrightarrow{\boldsymbol{x}},t,T) \\ P(x,t,T) &= \frac{w_b c_b (T_a - T(t) + Q_m(t) + Q_r(t))}{\rho(T) c(T)} \\ D &= \frac{k}{\rho \cdot c} \end{aligned} \tag{6.3}$$

Here, $P(x,t,T)$ describes the local heat sources and sinks and $\overrightarrow{x}$ refers to the three dimensional point within the volume of interest. For each of the N heat sources on a point of the needle axis r_i, the orthogonal distance to each of the M isotherms t_m is determined and summed up. To obtain the relative temperature distribution along the axis, the total distances are divided by the maximum total distance q_{max} of all N points. This results in a relative strength of the heat points q_i in the range [0,1] as given by Equation 6.4:

$$q_i = \frac{1}{q_{max}} \sum_{m=0}^{M} |r_i - t_m| \forall i \in N \tag{6.4}$$

By specifying a factor, an absolute distribution can be obtained from the relative distribution. This factor limits the heat input to a maximum temperature and can thus be understood as a vertical shift of the complete temperature distribution. In the form of a newly introduced ablation parameter, T_{max} assigns an absolute value T_i to each q_i using Equation 6.5

$$T_i = q_i \cdot T_{max} \tag{6.5}$$

The quantitative determination of unknown tissue and ablation parameters can be described by the inverse heat conduction problem. In this approach, the inverse heat transfer for estimating the values of the simulation parameters is performed using a least-square norm estimation procedure.

The Levenberg-Marquardt algorithm, originally developed for nonlinear parameter estimation problems (Levenberg, 1944; Marquardt, 1963), has been successfully applied to the solution of the ill conditioned inverse heat conduction problem (Min et al., 2014; Cui et al., 2017). Its combination of steepest descent and the Gauss-Newton

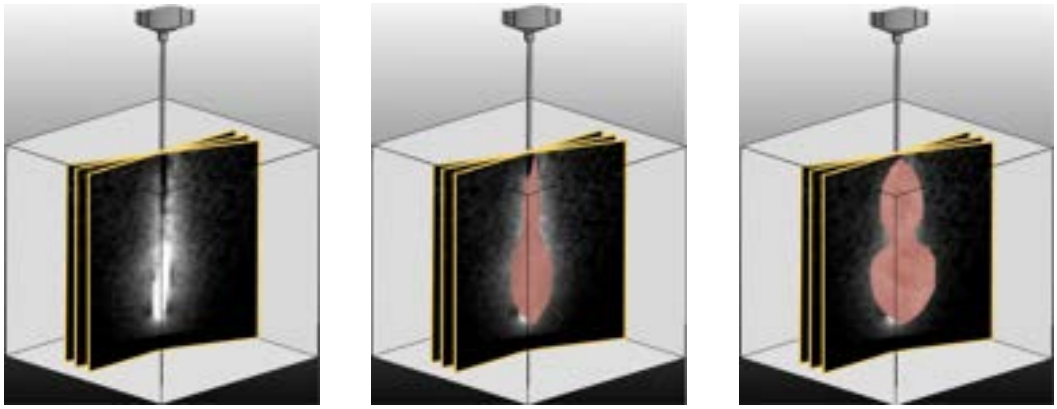

(a) Simulation at time point $t = 0$.

(b) Simulation at time point $t = 66$.

(c) Simulation at time point $t = 112$.

Fig. 6.3: The image slices are uniformly distributed around the applicator's main axis (three slices shown exemplary). Example of the 3D simulation (red volume) fitting using a least-square norm estimation half way through the procedure(t=66). The final simulation and fitting of the 3D simulation (red volume) is performed at the end of procedure (t=112). Note that the deformation on the left and right side of the simulation is caused by heat sink effects.

method increases robustness and the likelihood for convergence. For optimization of the simulation, the following objective function f has to be minimized:

$$f\left(P^i\right) = \sum_{j=0}^{N} \left[\overrightarrow{T_E}_j^i \left(P^i, \overrightarrow{T_E}_j^{i-1}\right) - \overrightarrow{T_R}_j^i\right]^2 \quad \forall t_i \in I_n \tag{6.6}$$

where $\overrightarrow{T_E}$ is the vector of estimated temperatures at the current discrete time step t_i. $\overrightarrow{T_E}$ is obtained by the direct Pennes' BHTE model. The simulation is based on the state of the optimization at time step t_{i-1} and is corrected by the updated unknown parameter set $P = \{D, T_{max}\}$. $\overrightarrow{T_R}$ is the vector of real temperatures extracted from the live 2D thermometry map. The sum squared error between each data point j in the live data and the 3D simulation is reduced for each new acquired thermometry map $I_1 ... I_n$. An example is shown in Fig. 6.3.

For defining the time varying tissue temperature T for every voxel at every time step t, the Crank–Nicolson's scheme for finite differences (Crank et al., 1947) is utilized as in Equation 6.7.

$$\frac{T_j^{i+1} - T_j^i}{\Delta t} = \frac{1}{2}\left(D\frac{T_{j+1}^i - 2T_j^i + T_{j-1}^i}{(\Delta x)^2} + P_j^i + D\frac{T_{j+1}^{i+1} - 2T_j^{i+1} + T_{j-1}^{i+1}}{(\Delta x)^2} + P_j^{i+1}\right) \tag{6.7}$$

This method combines the explicit and implicit Euler method in time and central differences in space. Hence, this scheme is unconditionally stable for diffusion equations and has second order spatial and temporal accuracy. For reducing the computational effort to solve the implicit equations in multiple dimensions, an alternating-direction implicit method (Douglas et al., 1964) is implemented. This allows for solving the linear system by only considering tridiagonal matrices, which can be done by the Thomas algorithm. The presented method was implemented on a GPU architecture using the alternating-direction implicit method for parabolic differential equations to further increase the computational speed. All source code is publicly available via `https://github.com/jalpers/ScientificReports2022_AdaptivePennesSimulation/tree/main`.

6.4 Experimental Setup

The same data set as explained in Chapter 3 is used for evaluation of the proposed adaptive simulation. The images are used as a sequential input for the algorithm to simulate a live fetching from the MR device, e.g., by using the Siemens Healthineers Access-I Framework for direct scanner control. Because the optimization of the simulation parameters is global and not local, heat sinks caused by vessels are not reflected by the simulation alone. Therefore, it is assumed that big vessels have been extracted from the pre-clinical data and can be applied to the final simulation outcome to a certain degree.

6.4.1 Initial Parameter Estimation

The initial condition is determined by the baseline temperature before the ablation, with $\boldsymbol{x} = (x, y, z)$ representing the 3D coordinate in the final output volume:

$$T(\overrightarrow{\boldsymbol{x}}, t) = T_0, \tag{6.8}$$

The huge amount of unaffected tissue in the peripheral boundary and a constant ambient temperature are suitable for using the Dirichlet boundary condition Γ_E:

$$T(\overrightarrow{\boldsymbol{x}}, t) = T_\Gamma, \quad t > t_0, \overrightarrow{\boldsymbol{x}} \in \Gamma_E \tag{6.9}$$

Due to the use of bio protein phantoms, the following parameters are set for the Penne's BHTE:

$$
\begin{aligned}
Q_m &= 0 \text{ (no metabolistic activity)} \\
c_b &= 4182[\frac{J}{Kg \cdot K}] \\
w_b &= \frac{\text{flow rate of pump * density of water}}{r^2\pi \cdot l} \\
T_a &= 25C^\circ
\end{aligned}
\tag{6.10}
$$

The studies summarized by Mohammadi et al (Mohammadi et al., 2021) give a range of thermal diffusivity D from 0.142 to 3.68 $\frac{mm^2}{s}$ at 22°C. Considering the increasing values due to temperature dependence, the optimization range is set to [0.1, 5] $\frac{mm^2}{s}$ with an initial value of 1.5 $\frac{mm^2}{s}$. The second parameter to be optimized, T_{max}, has an optimization range from 80°C to 300°C and starts at the homogeneous and known ambient temperature T_0.

6.4.2 Statistical Evaluation

For statistical evaluation purpose, the simulated heat map has to be converted in a binary coagulation necrosis. To achieve this, the same thresholds as described in Chapter 4 are applied in the range of [50,60]°C for each phantom individually (Global threshold).

Regarding the accuracy, a similarity measurement between the simulation and the ground truth is performed using the DSC computed by Equation 6.11:

$$
DSC = \frac{2 * TP}{2 * TP + FP + FN} \tag{6.11}
$$

taking into account the relation between true positives (TP), false positives (FP) and false negatives (FN). To analyze the error of the results, again the SEM at a confidence interval level of 95% (p = 0.05) is used as seen in Equation 6.12.

$$
\begin{aligned}
\sigma &= \sqrt{\frac{\sum(x_i - \bar{x})^2}{N-1}} \\
SEM &= \frac{\sigma}{\sqrt{N}} * 1.96
\end{aligned}
\tag{6.12}
$$

with σ = standard deviation, x_i = current sample, $\bar{x}$ = mean value, N = sample size and 1.96 = approximated value of the 97.5 percentile of the standard normal distribution. The SEM provides an assumption on how far the sample's mean is likely

to be from the real population mean. In combination with the standard deviation σ, these statistical values are able to give a decent overview of the performance of the proposed method. The initial temperature interpolation method introduced in Chapter 3 is used as both methods need to have a priori knowledge about vessels as an Input.

In addition, tests regarding the robustness of the proposed method are conducted. For this purpose, the optimization is performed, on the one hand, with less real-time data, and, on the other hand, with less a priori knowledge about the expected values of the coefficients. The reduction of data can be achieved by not considering thermometry maps from certain orientations. Thus, an experimental setup is generated in which a modified recording protocol is simulated. Reducing the amount of data results in the following configurations: config. 1 = [0°, 22.5°, 45°, 67.5°], config. 2 = [90°, 112.5°, 135°, 157°], config. 3 = [0°, 22.5°], config. 4 = [90°] and config. 5 = [22.5°]. Additional tests were performed by variation of the optimization parameters initial values and search criteria. Here, the following two configurations were tested: config. 6 = Unrestricted search range with D in the range [0.1,1000] and T_{max} also in the range [0.1,1000] and config. 7 = Unrealistic initial parameters with D = 10 $\frac{mm^2}{s}$ and T_{max} = 500°C. All robustness tests were also conducted with an additional threshold configuration (Median). Instead of using the global threshold as explained in Chapter 4 the best threshold for each individual orientation was identified. Afterwards, the median of these eight thresholds was computed and used for better reflection of the varying conditions inside the tissue.

Finally, an ANOVA test paired with post-hoc pairwise t-tests is performed to analyze the significance of each conducted test scenario. All p-values are adjusted using the Bonferroni correction method and reported as horizontal lines in Fig. 6.4 and Fig. 6.5.

6.5 Results

ANOVA test results can be seen in Table 6.3. Evaluation results regarding the similarity and the corresponding post-hoc results can be observed in Fig. 6.4. Observations show an average overall DSC of 0.89$\pm$0.04 exceeding the original temperature interpolation approach by a total of 0.10 regarding the overall average DSC. With respect to the homogeneous and perfusion phantoms separately, an average DSC of 0.91$\pm$0.02 and 0.86$\pm$0.03 can be observed, respectively. The SEM values are constant at 0.01 for all three groups. Regarding the standard deviation,

Tab. 6.3: ANOVAs' results. Df = degrees of freedom, F = F-value, p = probability of the data given the null hypothesis, Sig. = p-values less than the traditional α <0.05, η^2 = Generalized Eta-Squared measure of effect size.

Variable	df	F	p	Sig.	η^2
Accuracy					
Algorithm for all phantoms (overall)	2	23.97	<0.001	*	0.48
Algorithm for perfusion phantoms	2	6.82	0.001	*	0.43
Algorithm for homogeneous phantoms	2	77.69	<0.001	*	0.89
Robustness					
Local threshold	84	0.96	0.44		0.02
Global threshold	84	1.03	0.42		0.02
Reference configuration	12	10.38	0.007	*	0.21
Test configuration 1	12	7.86	0.016	*	0.14
Test configuration 2	12	5.95	0.031	*	0.15
Test configuration 3	12	8.12	0.015	*	0.07
Test configuration 4	12	10.09	0.008	*	0.23
Test configuration 5	12	11.14	0.006	*	0.12
Test configuration 6	12	7.05	0.021	*	0.16
Test configuration 7	12	5.5	0.037	*	0.13

the initial method presented in Chapter 3 shows values of 0.3 and 0.17 for the homogeneous and perfusion phantoms, respectively. The simulation approach presented in this Chapter shows a standard deviation of 0.02 and 0.03 for the homogeneous and perfusion phantoms, respectively. In conclusion, the proposed method does not only exceed the previous version by a mean DSC of 0.10, but it is also more robust towards corrupted images, which caused the temperature interpolation method to fail. With respect to the robustness tests, slight differences in the overall mean DSC for all phantoms can be seen, but significant changes between the different configurations could be detected. Therefore, it can be assumed that the number of different orientations during image acquisition, as well as the initial parameter values and boundary conditions, do not have an influence on the performance of the proposed method. Regarding the variation of the threshold configuration significant differences between the global and median approach could be detected. All results can be observed in Fig. 6.5 including the post-hoc pairwise t-test results as horizontal lines. All results were generated on a Desktop PC (Intel Core i7-2600K, 16GB RAM, NVIDIA GeForce GTX 1060 with 6GB memory) with

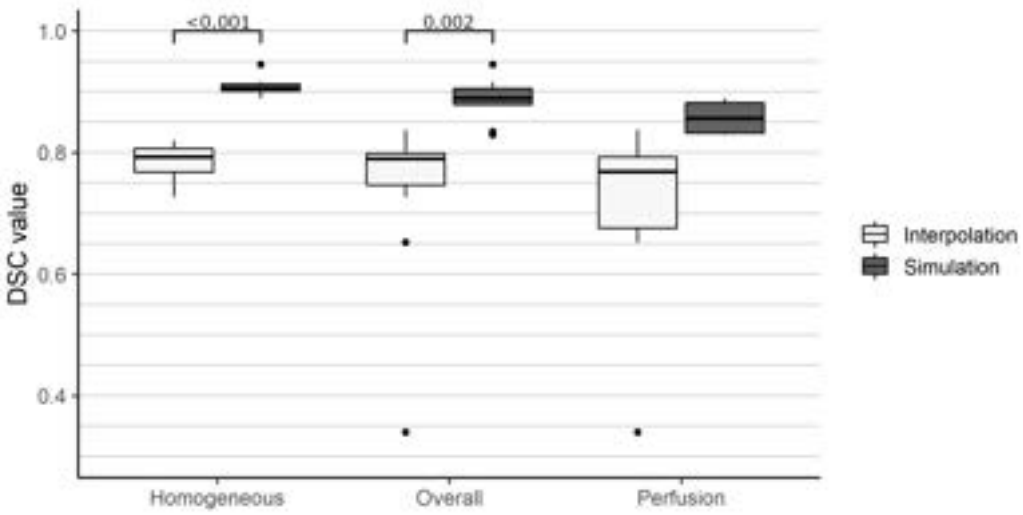

Fig. 6.4: Results of the similarity measurements. The DSC is separated for each phantom category with: Homogeneous = Phantoms without PVC tubes and water perfusion (n=7). Perfusion = Phantoms with PVC tubes and water perfusion (n=6) . Overall = All phantoms (n=13). Horizontal lines indicate statistically significant post-hoc pairwise t-test results. No values are located below a DSC of 0.3.

GPU acceleration and computation of the parameters D and T_{max} took 1.05±0.26 seconds for each newly acquired image. Computation times are based on a volume size of 60x60x60 voxels and 100 repetitions.

6.6 Discussion and Conclusion

One of the advantages of the proposed method is the rotation of the acquired images around the main axis of the applicator. This results in a typical shape of heat propagation, even when vessels causing a heat sink effect are present. Hence, the measurement can be easily verified and corrected. In addition, every image contains the heat source in the form of the elongated artifact of the applicator. This artifact can be detected and traced back to find the source of the heat distribution used for simulation. Nonetheless, the preparation of this sequence protocol can be troublesome for inexperienced MRI users. In order to be as accurate as possible, the rotated images should intersect in the center of the field of view, and this intersection should correspond to the applicator's main axis. Even though this should not be troublesome for an experienced MRI user, it might be cumbersome for new radiologists or medical technical assistants. Another problem may arise from out-of-plane angulation or bending of the needle. The more the needle is away from the intersection of the rotated planes, the less accurate the simulation

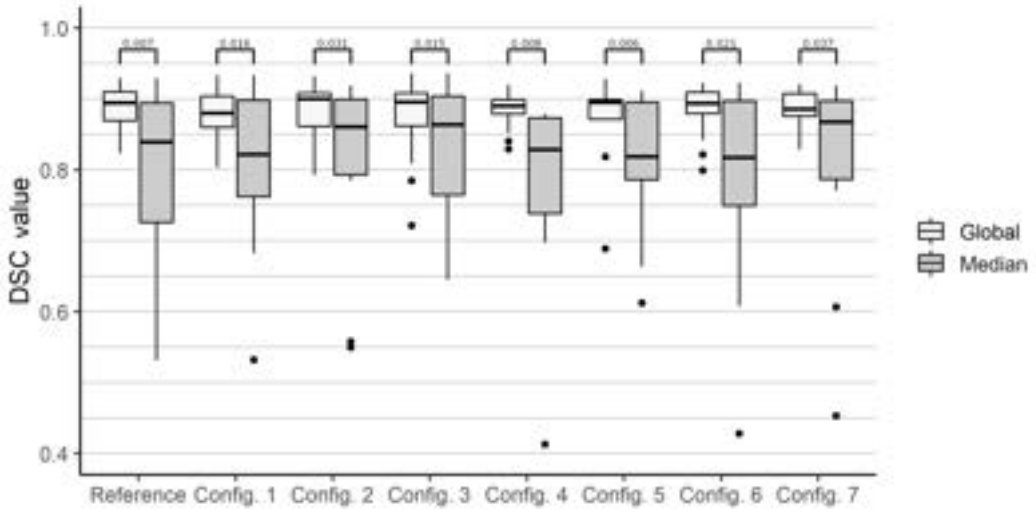

Fig. 6.5: Results of the robustness analysis. Configuration (Config.) 1 - 5 represent the variation of the number of orientations. Configuration 6 and 7 represent the variation of optimization parameters. Global = globally optimized threshold. Median = Median from the optimized thresholds of each of the eight image orientations. Horizontal lines indicate statistically significant post-hoc pairwise t-test results. No values are located below a DSC of 0.4.

method will be because the simulated applicator axis (heat source) is inaccurate. Here, a possible solution could be the inclusion of a priori knowledge about the applicator's position, either from manual annotation or planning. Additionally, an automated slice positioning algorithm can be used to find the optimum positioning of the images during intervention. Van der Kouwe et al. (2005) introduced an atlas-based approach for aligning the MRI plane in the region of interest. This approach may be applied to the simulation by acquisition of a 3D reference volume after needle insertion and prior treatment. The needle artifact can be extracted automatically, and an optimal MRI plane position can be computed and applied. Another problem with the presented approach arises from the used bio protein heat phantoms. According to Bu Lin et al. (2008), the coagulation of the phantom highly depends on the pH-value, which can vary within the phantom itself. For this reason, the computation of the coagulation necrosis using, e.g., a threshold approach, will introduce an error of unknown size. In addition, the used PVC tubes to simulate a heat sink effect do not provide real tissue dependent parameters. Hence, the approximation of the perfusion term does not reflect the real heat distribution. This problem can be addressed by evaluation of the method in a more clinical context. Here, perfused ex vivo porcine livers can be used, as introduced by Becker et al. (D. Becker et al., 2019), to create a more realistic data base. Regarding the algorithm, a global approach for optimization of the parameters was used. This leads to a

more or less homogeneous prediction of the ablation zone, but does not take into account local tissue variation or heat sinks without a priori knowledge based on e.g., segmentation of structures. Here, it would be suitable to look for a computationally efficient solution for local optimization of the parameters. This approach could be combined with the temperature interpolation method presented in Chapter 3. The local parameters could be optimized for one image locally and then interpolated between the other acquired images.

Conclusion. In this Chapter new approach for an adaptive Penne's BHTE for interventional MR-guided tumor ablation was proposed. The approach is robust towards outliers and artifacts and shows promising results of up to 90% similarity to a manually extracted ground truth. Due to the unique image acquisition protocol, it is possible to identify the heat source in every image and therefore are not limited to a specific heat source term. This reduces the computational effort and allows the method to be applicable to a wide range of clinical setups. Future work should focus on a local optimization of the simulation parameters instead of a global optimization. I highly believe that this approach would be able to accurately detect heat sinks in the data. In summary, the method presented in this Chapter shows a high potential to aid the performing radiologist during minimally invasive thermal procedures and increase the success rate, while not necessarily hampering the workflow of the individual clinician.

Conclusion

7

> *Critical thinking is not something you do once with an issue and then drop it. It requires that we update our knowledge as new information comes in.*
>
> — **Daniel Levitin**
> Cognitive Psychologist

Minimally invasive thermal ablation procedures are becoming increasingly important in the treatment of malignant tissues. The full coverage of the malignant tissue is very important, as it mainly depicts the chances of local tumor progression after the intervention. Because the computation of volumetric thermometry is troublesome in terms of developed MR-sequences, it is of great interest to transfer the problem of volumetric thermometry reconstruction into another field.

The presented thesis covers a first approach on the transfer of the problem into the domain of computer science by developing a new image acquisition protocol. This protocol utilizes common 2D-GRE sequences by rotating the image plane around the applicators main axis and performing a simple 2D to 3D reconstruction. The developed algorithms were statistically compared regarding their efficiency. It was shown that conventional image processing methods are suitable to reconstruct a volumetric thermometry map for clinical use.

7.1 Contribution

In Chapter 1 the current problems were defined and explained in relation to the reconstruction of volumetric thermometry maps. These problems include:

1. Real-time image acquisition
2. Minimizing Motion Artifacts
3. Ease of Use

4. Coagulation Estimation

In addition, the following two research questions were defined in Chapter 1 and addressed in Chapters 3 to 6:

1. "Can conventional image processing algorithms be used to reconstruct volumetric thermometry maps from 2D slices with at least 80% accuracy while being real-time capable?"

2. "Is it possible to utilize the Pennes' Bioheat Transfer Equation to simulate the actual coagulation necrosis during thermal tumor ablation in real-time while avoiding simulation error accumulation?"

In the following, the contributions of this thesis will be summarized.

New Sequence Protocol

The approach presented in this thesis is not developing a new MR sequence but utilizing a common 2D GRE sequence. This sequence is available in a wide range of clinical setups and is exploited by rotating it around the applicator's main axis. The acquired images are fetched from the MR scanner using the Siemens Healthineers Access-I framework. For testing, a data base of 13 bioprotein phantoms (Bu-Lin et al., 2008) was created and made publicly available. This data base can be used by fellow researchers to develop and/or test 2D to 3D reconstruction algorithms for volumetric heat map generation.

The new sequence protocol addresses the problems:

- *Real-time image acquisition*, as the Access-I Framework allows for immediate fetching of the images without the delay through the PACS

- *Minimizing Motion Artifacts*, as the use of a single 2D image at a time is able to minimize the motion artifacts as it can be synchronized with the breathing cycle (Gorny et al., 2019)

- *Ease of Use*, as the maintenance and adjusting of a commonly known sequence is more intuitive and easy than a custom made sequence

Migration of the Problem from MR Physics to Computer Science

The new sequence protocol has additionally provided the possibility to sample the 3D volume with different temporal and spatial resolution, depending on the scenario. Using the sampled 2D images, simple 2D to 3D reconstruction algorithms can be utilized to create a volumetric heat map. In Chapter 4 the basic temperature interpolation, Delaunay triangulation, splines and MVEE were compared as possible approaches, including a statistical analysis. In addition, the implementation of all tested methods is publicly available via GitHub.

The migration of the problem from MR physics to computer science addresses the following problems and research questions:

- *Real-time image acquisition*, as the computation of the thermometry reconstruction is faster than the image acquisition during the intervention
- *Research question #1* can be answered positive as the statistical analysis shows a similarity of over 80% for the splines and MVEE methods

Adaptive Simulation for Interventional Use

After observation of the results presented in Chapter 4 an adaptive simulation was developed. The proposed method utilizes the same sequence protocol in combination with the Pennes' bio heat transfer equation, as the rotation around the applicator's main axis yields the benefit of showing the heat source in every acquired image. This advantage allows for elimination of the treatment specific heat source term and reduction of the problem to a diffusion process. To still enable real-time capabilities, the implementation was transferred to the GPU. In addition, all source code for the simulation is publicly available via GitHub.

The adaptive simulation for interventional use addresses the following problems and research questions:

- *Real-time image acquisition*, as the GPU implementation allows for computation times of less than 1.1s and therefore a faster reconstruction than the image acquisition
- *Research question #2* can be answered positive as the statistical analysis performed shows a similarity of 90% on average concluding that the error during simulation did not accumulate over the time of the intervention

Probabilistic CEM_{43} Model

All of the previously presented methods make use of the critical temperature model for the conversion of the heat maps into necrosis maps. This approach was used to compensate for the fact that the conventional CEM_{43} failed due to a bad SNR. To compensate for this, Chapter 5 introduces a mathematical model to convert the original CEM_{43} model into a probabilistic one, which integrates the MR measurement error. Evaluation shows that the new approach is able to increase the accuracy during prediction of the coagulation necrosis.

The probabilistic CEM_{43} model addresses the following problems:

- *Real-time image acquisition*, as the provided GPU acceleration cause the computations to be faster than the actual image acquisition
- *Coagulation Estimation*, as the accuracy of the conventional models could be increased

Considering the above-mentioned contribution, this thesis offers a contribution to the field of volumetric heat map reconstruction during minimally invasive thermal ablation procedures. It was shown that conventional 2D to 3D reconstruction methods are suitable for accurate reconstruction while considering the applicability and real-time capabilities of the developed methods.

7.2 Limitations

Even though the previously mentioned contributions show that the developed methods are suitable for volumetric thermometry reconstruction, some limitations still remain, and others are introduced. In the following paragraphs, the identified limitations and problems will be explained in detail including a suggestion on how to tackles these in the future.

Real-time image acquisition

Real-time image acquisition in the context of this thesis was defined using two major characteristics:

1. The fetching of the acquired images has to be transferred to the software without delay caused by, e.g., transfer through the PACS.

2. The performed computational operations need to be faster than the used image acquisition protocol (in the presented case less than 1.1 seconds) as per the feedback of available clinical partners.

As can be seen the achievement of a real-time capable reconstruction in the terms of interventional radiology is highly dependent on the used MR sequence protocol and therefore not unified. Especially in the field of thermal ablation procedures, a dynamic temporal mapping of the VOI is crucial. The coagulation necrosis grows very fast in the first few minutes of the intervention, while it slows down towards the end of the procedure until it reaches stagnation. Hence, it would be suitable to adapt the proposed method in a way to dynamically change the spatial and temporal resolution of the sequence protocol. This could be done utilizing a proper scanner remote control interface like Access-I. Here, a suitable protocol can be the implementation of a lower sampling rate in the VOI, resulting in fewer orientations and therefore providing a better overview of the heat distribution in the whole volume. In the later stages of the intervention, it would be more suitable to have a higher sampling rate with more orientations, as the observation of the MAM is crucial for the outcome of the intervention.

Necessity of PRFS reference images

The previously mentioned limitation regarding the dynamic temporal and spatial resolution is also caused by the necessity of reference images for the used PRFS thermometry method. This limits the approaches proposed in this thesis to a pre-defined set of orientations preventing a dynamic adjustment of the sampling factor. Here, it is necessary to implement a referenceless PRFS method. Zou et al. (2016) compare five different approaches for referenceless MR thermometry model. Their work can be used to analyse the potential of any of these for the use during intra-operative monitoring of thermal ablation processes.

Manual placement of the VOI

The introduced method can be used in three different ways as per the current implementation. First, the sequence protocol can be defined manually one time using different dependent slice groups. This preset can be saved and loaded during any intervention, but the whole VOI has to be placed manually inside the data set making sure that the intersection of the planes is also overlaying the artifact of the needle in the pre-intervention planning data set. The second approach

makes use of scanner remote control protocols like Access-I. Here, only one image plane has to be placed more or less centered within the applicator's artifact. The scanner remote control protocol is able to rotate this image plane around a defined axis (e.g., the applicator's main axis). In this thesis, the Access-I framework was implemented and tested to fetch the images from the MR device but the image planes were placed manually by a medical technical assistant to avoid ambiguities during phantom ablation. An improvement of the current procedure would be a third fully automatic approach for finding the the applicator's main axis inside the data set and placing the image plane into the intersection. Afterwards, the rotation angles can be automatically computed and the single image plane can be rotated around the applicator's main axis. For finding the needle inside the data set, Mehrtash et al. (2018) introduced an algorithm for automatic needle segmentation in 3D MRI data using convolutional neural networks. Utilizing up-to-date GPU architectures this approach could be implemented while preserving real-time capabilities. Another approach could be derived from the work of Van der Kouwe et al. (2005). Their work introduces an atlas-based approach for aligning the MRI plane in a region of interest.

Full sampling of the VOI is time-consuming

In the current version of the data base, a sequence protocol with 1.1 second pure image acquisition is utilized including an additional five second break to simulate the breathing cycle of a patient. Using a total of eight orientations, a full rotation in the VOI takes 48.8 seconds. Therefore, slices adjacent to the latest one are out of date but still used for interpolation. In the first half of an intervention, this introduced error can be very high; however, the error gets smaller over time as the heat propagation boundary converges towards its maximum extend. To reduce this error, a gradient propagation can be introduced. The latest acquired heat gradient profile will be extracted and analyzed for each row in the image matrix, separately. This profile is then compared with the one from the last time point in the same orientation. The difference in the heat gradient profiles can be computed and applied to all other orientations. Using the information from the other gradient profiles, the difference could also be adjusted to prevent an overcorrection of the real temperature.

Local vs. global optimization during simulation

The proposed adaptive Penne's BHTE offers an intra-operative simulation, but the optimization computes the used simulation parameters on a global base for the

whole image. This results in tissue inhomogeneities not being considered during this reconstruction approach. To overcome this limitation, a local optimization with more than one resulting parameter set would be beneficial. Here, the image could be analyzed row-wise or in smaller patches to create local optimized parameter sets. Using this approach, the possibility to detect heat sinks can be increased, and also non-homogeneous heat distribution can be simulated without the use of apriori knowledge. To keep this possibility real-time capable, the use of an optimized GPU architecture has to be utilized. Switching from the used FDM method to a meshless numerical technique for simulation like the material-to-points (MPM) method may increase the computational efficiency of the optimization problem. Here, Liu et al. (2020) introduced an approach for a multi-GPU MPM method using a shared memory. Their solution allows for synchronizing several GPU architectures to increase the computational power of the whole system. With more computational power, Penne's BHTE could also be replaced in the future by more complex but more accurate BHTEs.

Probabilistic CEM_{43} model only includes approximation of MR measurement error

For the development of the probabilistic CEM_{43} model, only the approximation of the MR measurement error was considered. Here, it would be suitable in the future to also consider the integration of other sources of errors, which can be considered by the probabilistic nature of the model like known MRI artifacts that can be detected using image processing software. A subsequent adjustment of σ_R and σ_I according to the character of these artifacts could further improve the robustness of the proposed approach. In addition, the results acquired are not meaningful to a full extent because of the small sample size during evaluation. More image data needs to be acquired and evaluation should be repeated for significant assumptions.

Heat sink detection

The last limitation identified is the proper detection of heat sink effects inside the acquired image data during the intervention. This detection is crucial as heat sinks are hampering the treatment especially near bigger blood vessels (Pillai et al., 2015). Right now, only the Splines method is able to consider these during the reconstruction of the volumetric thermometry map. This problem is usually not addressed directly, but indirectly through, e.g., the introduction of automatic

vessel segmentation algorithms. Lu et al. (2017) introduced an automatic vessel segmentation algorithm for vessels in the liver. Their proposed method is able to achieve a DSC similarity of over 80%, which as per definition is rated as clinically acceptable.

7.3 Future Work

Based on the identified limitations of the present thesis, this Section will provide a brief overview of specific steps, which should be conducted in the near future.

In order to improve the clinical applicability of the proposed methods, the following next steps need to be performed an integrated into the existing framework:

1. (Semi-)automatic placement of the slice groups
2. Integration of referenceless thermometry computation
3. Proper detection of heat sink effects

To assist the medical technical assistant and to reduce the need for specialized experts, the effort in preparing the sequence protocol has to be reduced. During data base acquisition in Chapter 3, the Access-I framework was already implemented. This framework has to be extended to not only fetch the images from the scanner, but to also rotate the image slice automatically around the main axis. This will reduce the time needed and provides a higher clinical applicability in the daily routine of the hospitals.

Using the automated rotation, the need for dynamic change of the slices of interested has to be considered. Here, referencless thermometry approaches must be included. One of the approaches introduced by Zou et al. (2016) can be re-implemented and replace the current PRFS thermometry. Additionally, the provided software interface shall include a mask to change the orientations of the slices during intervention. Here, a proper usability engineering has to be conducted to accurately determine a workflow.

The last step after sequence protocol optimization should focus on the detection of heat sink effect. Two approaches come to mind. First, the heat profile of the acquired image data is analyzed and anomalies (like drops in the heat profile) are identified and considered during reconstruction. Second, the major vessel system is automatically identified, extracted and applied to the homogeneously reconstructed thermometry map. As vessel segmentation algorithms already exist, which have

proven to be reliable, one of these should simply be integrated in the first prototype. Here, the work from Lu et al. (2017) yields good results and is also compatible with the current architectural design (e.g., GPU acceleration).

Further researchers are encouraged to follow the above-mentioned steps before addressing other limitations, as the clinical applicability is a major factor for further ex-vivo and in-vivo tests. Further limitations will surely arise during clinical tests and an early identification of these will reduce the effort, time and frustration on the way towards a usable volumetric thermometry approach for the monitoring of thermal ablation procedures.

Bibliography

Abo-Alsabeh, Rewayda and Abdellah Salhi (2020). “An evolutionary approach to constructing the minimum volume ellipsoid containing a set of points and the maximum volume ellipsoid embedded in a set of points”. In: *Journal of Physics: Conference Series*. Vol. 1530. IOP Publishing, p. 012087 (cit. on pp. 47, 49).

Ahmed, Muneeb, Luigi Solbiati, Christopher L. Brace, et al. (2014). “Image-guided tumor ablation: standardization of terminology and reporting criteria—a 10-year update”. In: *Radiology* 273.1, pp. 241–260 (cit. on pp. 1, 26).

Baron, Paul, Roel Deckers, Martijn de Greef, et al. (2014). “Correction of proton resonance frequency shift MR-thermometry errors caused by heat-induced magnetic susceptibility changes during high intensity focused ultrasound ablations in tissues containing fat”. In: *Magnetic Resonance in Medicine* 72.6, pp. 1580–1589 (cit. on p. 72).

Beaulieu, Norman C, Adnan A Abu-Dayya, and Peter J McLane (1995). “Estimating the distribution of a sum of independent lognormal random variables”. In: *IEEE Transactions on Communications* 43.12, p. 2869 (cit. on p. 80).

Becker, Dustin, Max Hefti, Martin J Schuler, et al. (2019). “Model assisted analysis of the hepatic arterial buffer response during ex vivo porcine liver perfusion”. In: *IEEE Transactions on Biomedical Engineering* 67.3, pp. 667–678 (cit. on pp. 41, 113).

Bever, Joshua de, Nick Todd, Allison Payne, Douglas A Christensen, and Robert B Roemer (2014). “Adaptive model-predictive controller for magnetic resonance guided focused ultrasound therapy”. In: *International Journal of Hyperthermia* 30.7, pp. 456–470 (cit. on pp. 100, 102).

Bever, Joshua T de, Henrik Odéen, Lorne W Hofstetter, and Dennis L Parker (2018). “Simultaneous MR thermometry and acoustic radiation force imaging using interleaved acquisition”. In: *Magnetic resonance in medicine* 79.3, pp. 1515–1524 (cit. on pp. 29, 30).

Blackwell, James, Marcin J Kraśny, Aoife O’Brien, et al. (2022). “Proton resonance frequency shift thermometry: a review of modern clinical practices”. In: *Journal of Magnetic Resonance Imaging* 55.2, pp. 389–403 (cit. on p. 15).

Bourantas, George C, Grand R Joldes, Adam Wittek, and Karol Miller (2019). “A flux-conservative finite difference scheme for the numerical solution of the nonlinear bioheat equation”. In: *Computational Biomechanics for Medicine*. Springer, pp. 69–81 (cit. on p. 105).

Bowyer, Adrian (1981). “Computing dirichlet tessellations”. In: *The computer journal* 24.2, pp. 162–166 (cit. on pp. 46, 52).

Brace, Christopher L (2009). “Microwave ablation technology: what every user should know”. In: *Current problems in diagnostic radiology* 38.2, pp. 61–67 (cit. on p. 17).

Bray, Freddie, Jacques Ferlay, Isabelle Soerjomataram, et al. (2018). “Global cancer statistics 2018: GLOBOCAN estimates of incidence and mortality worldwide for 36 cancers in 185 countries”. In: *CA: a cancer journal for clinicians* 68.6, pp. 394–424 (cit. on pp. 1, 17, 44).

Breen, Michael S, Miyuki Breen, Kim Butts, et al. (2007). “MRI-guided thermal ablation therapy: Model and parameter estimates to predict cell death from MR thermometry images”. In: *Annals of biomedical engineering* 35.8, pp. 1391–1403 (cit. on p. 57).

Brown, Robert W, Y-C Norman Cheng, E Mark Haacke, Michael R Thompson, and Ramesh Venkatesan (2014). *Magnetic resonance imaging: physical principles and sequence design*. John Wiley & Sons (cit. on pp. 11, 12).

Campwala, Zahabiya, Benjamin Szewczyk, Teresa Maietta, et al. (2021). “Predicting ablation zones with multislice volumetric 2-D magnetic resonance thermal imaging”. In: *International Journal of Hyperthermia* 38.1, pp. 907–915 (cit. on p. 32).

Carluccio, Giuseppe, Danilo Erricolo, Sukhoon Oh, and Christopher M Collins (2013). “An approach to rapid calculation of temperature change in tissue using spatial filters to approximate effects of thermal conduction”. In: *IEEE Transactions on Biomedical Engineering* 60.6, pp. 1735–1741 (cit. on p. 92).

Chen, Qiaoyan, Ye Li, Rui Jiang, et al. (2020). “A flexible 9-channel coil array for fast 3D MR thermometry in MR-guided high-intensity focused ultrasound (HIFU) studies on rabbits at 3 T”. In: *Magnetic Resonance Imaging* 65, pp. 37–44 (cit. on p. 30).

Chu, William, Robert M Staruch, Samuel Pichardo, et al. (2016). “Magnetic Resonance–Guided high-intensity focused ultrasound hyperthermia for recurrent rectal cancer: Mr thermometry evaluation and preclinical validation”. In: *International Journal of Radiation Oncology* Biology* Physics* 95.4, pp. 1259–1267 (cit. on pp. 31, 32).

Crank, John and Phyllis Nicolson (1947). “A practical method for numerical evaluation of solutions of partial differential equations of the heat-conduction type”. In: *Mathematical proceedings of the Cambridge philosophical society*. Vol. 43. Cambridge University Press, pp. 50–67 (cit. on p. 107).

Cui, Miao, Yi Zhao, Bingbing Xu, and Xiao-wei Gao (2017). “A new approach for determining damping factors in Levenberg-Marquardt algorithm for solving an inverse heat conduction problem”. In: *International Journal of Heat and Mass Transfer* 107, pp. 747–754 (cit. on p. 106).

De Boor, Carl and Carl De Boor (1978). *A practical guide to splines*. Vol. 27. springer-verlag New York (cit. on pp. 47, 55).

De Senneville, Baudouin Denis, Sébastien Roujol, Silke Hey, Chrit Moonen, and Mario Ries (2012). “Extended Kalman filtering for continuous volumetric MR-temperature imaging”. In: *IEEE Transactions on Medical Imaging* 32.4, pp. 711–718 (cit. on pp. 100, 102).

Deng, Xiang and Thomas S Denney (2004). “Three-dimensional myocardial strain reconstruction from tagged MRI using a cylindrical B-spline model”. In: *IEEE Transactions on Medical Imaging* 23.7, pp. 861–867 (cit. on p. 47).

Deshazer, Garron, Punit Prakash, Derek Merck, and Dieter Haemmerich (2017). “Experimental measurement of microwave ablation heating pattern and comparison to computer simulations”. In: *International Journal of Hyperthermia* 33.1, pp. 74–82 (cit. on p. 103).

Dharmadhikari, Shalmali, Judy R James, John Nyenhuis, and Navin Bansal (2016). “Evaluation of radiofrequency safety by high temperature resolution MR thermometry using a paramagnetic lanthanide complex”. In: *Magnetic Resonance in Medicine* 75.5, pp. 2121–2129 (cit. on pp. 29, 30).

Dijkstra, Edsger W (1959). “A note on two problems in connexion with graphs”. In: *Numerische mathematik* 1.1, pp. 269–271 (cit. on p. 104).

Dos Santos, Icaro, Dieter Haemmerich, David Schutt, Adson Ferreira da Rocha, and Leonardo Rax Menezes (2009). “Probabilistic finite element analysis of radiofrequency liver ablation using the unscented transform”. In: *Physics in Medicine & Biology* 54.3, p. 627 (cit. on p. 71).

Douglas, Jim and James E Gunn (1964). “A general formulation of alternating direction methods”. In: *Numèrische mathèmatik* 6.1, pp. 428–453 (cit. on p. 108).

Dutta, Joyita, Georges El Fakhri, Chuan Huang, et al. (2013). “Respiratory motion compensation in simultaneous PET/MR using a maximum a posteriori approach”. In: *2013 IEEE 10th International Symposium on Biomedical Imaging*. IEEE, pp. 800–803 (cit. on p. 41).

Ehses, Maik, Karen Meyer Zu Hartlage, Thomas Gerlach, et al. (2021). “3D-Printed Floating Cable Traps for MRI guided Microwave Ablation”. In: *2021 43rd Annual International Conference of the IEEE Engineering in Medicine & Biology Society (EMBC)*. IEEE, pp. 1419–1422 (cit. on p. 41).

Enholm, Julia K, Max O Kohler, Bruno Quesson, et al. (2009). “Improved volumetric MR-HIFU ablation by robust binary feedback control”. In: *IEEE Transactions on Biomedical Engineering* 57.1, pp. 103–113 (cit. on pp. 99, 102).

Faridi, Pegah, Tej B Shrestha, Marla Pyle, et al. (2020). “Temperature estimation for MR-guided microwave hyperthermia using block-based compressed sensing”. In: *2020 42nd Annual International Conference of the IEEE Engineering in Medicine & Biology Society (EMBC)*. IEEE, pp. 5057–5060 (cit. on pp. 48, 49).

Feddersen, Theresa V, Juan A Hernandez-Tamames, Martine Franckena, Gerard C van Rhoon, and Margarethus M Paulides (2020). “Clinical performance and future potential of magnetic resonance thermometry in hyperthermia”. In: *Cancers* 13.1, p. 31 (cit. on pp. 2, 26).

Fielden, Samuel W., Xue Feng, Li Zhao, et al. (2018). “A spiral-based volumetric acquisition for MR temperature imaging”. In: *Magnetic resonance in medicine* 79.6, pp. 3122–3127 (cit. on pp. 29, 30).

Fu, Yifan and Jian Wu (2014). “On verification of splines based intraoperative reconstruction of cardiac anatomy: Model research”. In: *2014 36th Annual International Conference of the IEEE Engineering in Medicine and Biology Society*. IEEE, pp. 2436–2439 (cit. on pp. 48, 49).

Fuentes, David, Yusheng Feng, Andrew Elliott, et al. (2010). “Adaptive real-time bioheat transfer models for computer-driven MR-guided laser induced thermal therapy”. In: *IEEE transactions on biomedical engineering* 57.5, pp. 1024–1030 (cit. on pp. 100, 102).

Fuentes, David, J Yung, John D Hazle, Jeffrey S Weinberg, and R Jason Stafford (2011). “Kalman filtered MR temperature imaging for laser induced thermal therapies”. In: *IEEE transactions on medical imaging* 31.4, pp. 984–994 (cit. on pp. 100, 102).

Galassi, Francesca, Mohammad Alkhalil, Regent Lee, et al. (2018). “3D reconstruction of coronary arteries from 2D angiographic projections using non-uniform rational basis splines (NURBS) for accurate modelling of coronary stenoses”. In: *PloS one* 13.1, e0190650 (cit. on p. 47).

Gorny, K. R., C. P. Favazza, A. Lu, et al. (2019). “Practical implementation of robust MR-thermometry during clinical MR-guided microwave ablations in the liver at 1.5 T”. In: *Physica Medica* 67, pp. 91–99 (cit. on pp. 2, 6, 26, 35, 50, 116).

Grover, Vijay PB, Joshua M Tognarelli, Mary ME Crossey, et al. (2015). “Magnetic resonance imaging: principles and techniques: lessons for clinicians”. In: *Journal of clinical and experimental hepatology* 5.3, pp. 246–255 (cit. on p. 10).

Gudbjartsson, Hákon and Samuel Patz (1995). “The Rician distribution of noisy MRI data”. In: *Magnetic resonance in medicine* 34.6, pp. 910–914 (cit. on p. 85).

Hafid, Mohamed and Marcel Lacroix (2017). “Fast inverse prediction of the freezing front in cryosurgery”. In: *Journal of Thermal Biology* 69, pp. 13–22 (cit. on pp. 100, 102).

He, Zhi-Zhu and Jing Liu (2016). “An efficient parallel numerical modeling of bioheat transfer in realistic tissue structure”. In: *International Journal of Heat and Mass Transfer* 95, pp. 843–852 (cit. on p. 92).

Hinkley, David V (1969). “On the ratio of two correlated normal random variables”. In: *Biometrika* 56.3, pp. 635–639 (cit. on p. 76).

Ishihara, Yasutoshi, Arturo Calderon, Hidehiro Watanabe, et al. (1995). “A precise and fast temperature mapping using water proton chemical shift”. In: *Magnetic resonance in medicine* 34.6, pp. 814–823 (cit. on p. 14).

Jeong, Hongbae, Matthew C Restivo, Peter Jezzard, and Aaron T Hess (2021). “Assessment of radio-frequency heating of a parallel transmit coil in a phantom using multi-echo proton resonance frequency shift thermometry”. In: *Magnetic resonance imaging* 77, pp. 57–68 (cit. on p. 30).

Jiang, Rui, Sen Jia, Yangzi Qiao, et al. (2020). “Real-time volumetric MR thermometry using 3D echo-shifted sequence under an open source reconstruction platform”. In: *Magnetic resonance imaging* 70, pp. 22–28 (cit. on pp. 26, 30).

Jiang, Yuwei and Lei Yang (2021). “Numerical modeling and Uncertainty analysis of irreversible electroporation in liver tumors”. In: *Proceedings of the 2021 International Conference on Bioinformatics and Intelligent Computing*, pp. 77–81 (cit. on p. 71).

Johnson, Peter C and Gerald M Saidel (2002). “Thermal model for fast simulation during magnetic resonance imaging guidance of radio frequency tumor ablation”. In: *Annals of Biomedical Engineering* 30.9, pp. 1152–1161 (cit. on p. 97).

Kägebein, Urte, Oliver Speck, Frank Wacker, and Bennet Hensen (2018). “Motion correction in proton resonance frequency–based thermometry in the liver”. In: *Topics in Magnetic Resonance Imaging* 27.1, pp. 53–61 (cit. on pp. 2, 44).

Kaye, Elena A, Kristin L Granlund, Elizabeth A Morris, Majid Maybody, and Stephen B Solomon (2015). “Closed-bore interventional MRI: percutaneous biopsies and ablations”. In: *American Journal of Roentgenology* 205.4, W400–W410 (cit. on p. 18).

Kickhefel, Antje, Clifford Weiss, Joerg Roland, et al. (2012). “Correction of susceptibility-induced GRE phase shift for accurate PRFS thermometry proximal to cryoablation iceball”. In: *Magnetic Resonance Materials in Physics, Biology and Medicine* 25.1, pp. 23–31 (cit. on pp. 29, 30).

Köhler, Max O, Charles Mougenot, Bruno Quesson, et al. (2009). “Volumetric HIFU ablation under 3D guidance of rapid MRI thermometry”. In: *Medical physics* 36.8, pp. 3521–3535 (cit. on pp. 31, 32).

Kokuryo, Daisuke, Etsuko Kumamoto, and Kagayaki Kuroda (2020). “Recent technological advancements in thermometry”. In: *Advanced Drug Delivery Reviews* 163, pp. 19–39 (cit. on pp. 26, 28).

Kouwe, André JW van der, Thomas Benner, Bruce Fischl, et al. (2005). “On-line automatic slice positioning for brain MR imaging”. In: *Neuroimage* 27.1, pp. 222–230 (cit. on pp. 113, 120).

Labarbera, Nicholas (2017). “Uncertainty quantification in irreversible electroporation simulations”. In: *Bioengineering* 4.2, p. 41 (cit. on p. 71).

Laimer, Gregor, Peter Schullian, Nikolai Jaschke, et al. (2020). “Minimal ablative margin (MAM) assessment with image fusion: an independent predictor for local tumor progression in hepatocellular carcinoma after stereotactic radiofrequency ablation”. In: *European radiology* 30.5, pp. 2463–2472 (cit. on pp. 1, 44, 68).

Landro, Martina de, Sanzhar Korganbayev, Khalid Ambarki, et al. (2021). “Magnetic resonance-based measurement system: comparison of 2D and 3D echo-planar imaging sequences for thermometry application”. In: *2021 IEEE International Instrumentation and Measurement Technology Conference (I2MTC)*. IEEE, pp. 1–6 (cit. on p. 32).

Levenberg, Kenneth (1944). “A method for the solution of certain non-linear problems in least squares”. In: *Quarterly of applied mathematics* 2.2, pp. 164–168 (cit. on p. 106).

Bu-Lin, Zhang, Hu Bing, Kuang Sheng-Li, et al. (2008). “A polyacrylamide gel phantom for radiofrequency ablation”. In: *International Journal of Hyperthermia* 24.7, pp. 568–576 (cit. on pp. 34, 35, 57, 113, 116).

Liu, Shuo, Bin Zou, Lamei Zhang, and Shulei Ren (2020). “A multi-GPU accelerated parallel domain decomposition one-step leapfrog ADI-FDTD”. In: *IEEE Antennas and Wireless Propagation Letters* 19.5, pp. 816–820 (cit. on p. 121).

Lloyd, David M, Kwan N Lau, Fenella Welsh, et al. (2011). “International multicentre prospective study on microwave ablation of liver tumours: preliminary results”. In: *Hpb* 13.8, pp. 579–585 (cit. on p. 17).

Lu, Siyu, Hui Huang, Ping Liang, Gang Chen, and Liang Xiao (2017). “Hepatic vessel segmentation using variational level set combined with non-local robust statistics”. In: *Magnetic resonance imaging* 36, pp. 180–186 (cit. on pp. 122, 123).

Lubner, Meghan G, Christopher L Brace, J Louis Hinshaw, and Fred T Lee Jr (2010). “Microwave tumor ablation: mechanism of action, clinical results, and devices”. In: *Journal of Vascular and Interventional Radiology* 21.8, S192–S203 (cit. on pp. 16–18).

Mariappan, Panchatcharam, Phil Weir, Ronan Flanagan, et al. (2017). “GPU-based RFA simulation for minimally invasive cancer treatment of liver tumours”. In: *International journal of computer assisted radiology and surgery* 12.1, pp. 59–68 (cit. on p. 92).

Marot, Célestin, Jeanne Pellerin, and Jean-François Remacle (2019). “One machine, one minute, three billion tetrahedra”. In: *International Journal for Numerical Methods in Engineering* 117.9, pp. 967–990 (cit. on pp. 47, 49).

Marquardt, Donald W (1963). “An algorithm for least-squares estimation of nonlinear parameters”. In: *Journal of the society for Industrial and Applied Mathematics* 11.2, pp. 431–441 (cit. on p. 106).

Marx, Michael, Pejman Ghanouni, and Kim Butts Pauly (2017). “Specialized volumetric thermometry for improved guidance of MR g FUS in brain”. In: *Magnetic resonance in medicine* 78.2, pp. 508–517 (cit. on pp. 31, 32).

Marx, Michael, Juan Plata, and Kim Butts Pauly (2014). “Toward volumetric MR thermometry with the MASTER sequence”. In: *IEEE transactions on medical imaging* 34.1, pp. 148–155 (cit. on pp. 31, 32).

Mauri, Giovanni, Luca Maria Sconfienza, Lorenzo Carlo Pescatori, et al. (2017). “Technical success, technique efficacy and complications of minimally-invasive imaging-guided percutaneous ablation procedures of breast cancer: a systematic review and meta-analysis”. In: *European radiology* 27.8, pp. 3199–3210 (cit. on pp. 1, 26).

McClelland, Jamie R, Benjamin AS Champion, and David J Hawkes (2014). “Combining image registration, respiratory motion modelling, and motion compensated image reconstruction”. In: *Biomedical Image Registration: 6th International Workshop, WBIR 2014, London, UK, July 7-8, 2014. Proceedings 6*. Springer, pp. 103–113 (cit. on p. 41).

McDannold, Nathan, P Jason White, and G Rees Cosgrove (2020). “MRI-based thermal dosimetry based on single-slice imaging during focused ultrasound thalamotomy”. In: *Physics in Medicine & Biology* 65.23, p. 235018 (cit. on pp. 70, 73).

McVeigh, ER, RM Henkelman, and MJ Bronskill (1985). “Noise and filtration in magnetic resonance imaging”. In: *Medical physics* 12.5, pp. 586–591 (cit. on p. 75).

Mehrtash, Alireza, Mohsen Ghafoorian, Guillaume Pernelle, et al. (2018). “Automatic needle segmentation and localization in MRI with 3-D convolutional neural networks: application to MRI-targeted prostate biopsy”. In: *IEEE transactions on medical imaging* 38.4, pp. 1026–1036 (cit. on p. 120).

Min, Tao, Xing Chen, Yao Sun, and Qiang Huang (2014). “A numerical approach to solving an inverse heat conduction problem using the Levenberg-Marquardt algorithm”. In: *Mathematical Problems in Engineering* 2014 (cit. on p. 106).

Mitchell, Richard L (1968). “Permanence of the log-normal distribution”. In: *JOSA* 58.9, pp. 1267–1272 (cit. on p. 80).

Mohammadi, Ahad, Leonardo Bianchi, Somayeh Asadi, and Paola Saccomandi (2021). “Measurement of Ex Vivo Liver, Brain and Pancreas Thermal Properties as Function of Temperature”. In: *Sensors* 21.12, p. 4236 (cit. on p. 109).

Moshtagh, Nima et al. (2005). “Minimum volume enclosing ellipsoid”. In: *Convex optimization* 111.January, pp. 1–9 (cit. on p. 53).

Mougenot, Charles, Luis Kabongo, Bruno Quesson, and Chrit TW Moonen (2009). “MRgHIFU: Feedback temperature control with automatic deduction of BHT tissue parameters”. In: *AIP Conference Proceedings*. Vol. 1113. American Institute of Physics, pp. 231–235 (cit. on pp. 99, 102).

Odéen, Henrik, Scott Almquist, Joshua de Bever, Douglas A Christensen, and Dennis L Parker (2016). “MR thermometry for focused ultrasound monitoring utilizing model predictive filtering and ultrasound beam modeling”. In: *Journal of therapeutic ultrasound* 4.1, pp. 1–13 (cit. on pp. 29, 30).

Odéen, Henrik, Joshua de Bever, Scott Almquist, et al. (2014). “Treatment envelope evaluation in transcranial magnetic resonance-guided focused ultrasound utilizing 3D MR thermometry”. In: *Journal of Therapeutic Ultrasound* 2.1, pp. 1–11 (cit. on pp. 29, 30).

Odéen, Henrik and Dennis L Parker (2019). “Improved MR thermometry for laser interstitial thermotherapy”. In: *Lasers in surgery and medicine* 51.3, pp. 286–300 (cit. on pp. 31, 32).

Overduin, Christiaan G, Jurgen J Fütterer, and Tom WJ Scheenen (2016). “3D MR thermometry of frozen tissue: Feasibility and accuracy during cryoablation at 3T”. In: *Journal of Magnetic Resonance Imaging* 44.6, pp. 1572–1579 (cit. on pp. 29, 30).

Paschal, Cynthia B and H Douglas Morris (2004). “K-space in the clinic”. In: *Journal of Magnetic Resonance Imaging: An Official Journal of the International Society for Magnetic Resonance in Medicine* 19.2, pp. 145–159 (cit. on p. 13).

Pearce, John A (2009). “Relationship between Arrhenius models of thermal damage and the CEM 43 thermal dose”. In: *Energy-based Treatment of Tissue and Assessment V*. Vol. 7181. SPIE, pp. 35–49 (cit. on p. 72).

Pennes, Harry H (1948). “Analysis of tissue and arterial blood temperatures in the resting human forearm”. In: *Journal of applied physiology* 1.2, pp. 93–122 (cit. on pp. 4, 92, 105).

Petrusca, Lorena, Vincent Auboiroux, Thomas Goget, et al. (2014). “A nonparametric temperature controller with nonlinear negative reaction for multi-point rapid MR-guided HIFU ablation”. In: *IEEE transactions on medical imaging* 33.6, pp. 1324–1337 (cit. on pp. 31, 32).

Pillai, Krishna, Javid Akhter, Terence C Chua, et al. (2015). “Heat sink effect on tumor ablation characteristics as observed in monopolar radiofrequency, bipolar radiofrequency, and microwave, using ex vivo calf liver model”. In: *Medicine* 94.9 (cit. on p. 121).

Pooley, Robert A (2005). “Fundamental physics of MR imaging”. In: *Radiographics* 25.4, pp. 1087–1099 (cit. on pp. 9–11).

Poorter, John De (1995). “Noninvasive MRI thermometry with the proton resonance frequency method: study of susceptibility effects”. In: *Magnetic resonance in medicine* 34.3, pp. 359–367 (cit. on pp. 14, 16).

Poorter, John De, Carlos De Wagter, Yves De Deene, et al. (1995). “Noninvasive MRI thermometry with the proton resonance frequency (PRF) method: in vivo results in human muscle”. In: *Magnetic resonance in medicine* 33.1, pp. 74–81 (cit. on p. 14).

Poulou, Loukia S, Evanthia Botsa, Ioanna Thanou, Panayiotis D Ziakas, and Loukas Thanos (2015). “Percutaneous microwave ablation vs radiofrequency ablation in the treatment of hepatocellular carcinoma”. In: *World journal of hepatology* 7.8, p. 1054 (cit. on p. 17).

Prakosa, A, P Malamas, S Zhang, et al. (2014). “Methodology for image-based reconstruction of ventricular geometry for patient-specific modeling of cardiac electrophysiology”. In: *Progress in biophysics and molecular biology* 115.2-3, pp. 226–234 (cit. on pp. 48, 49).

Quah, Kristin, Megan E Poorman, Steven P Allen, and William A Grissom (2020). “Simultaneous multislice MRI thermometry with a single coil using incoherent blipped-controlled aliasing”. In: *Magnetic resonance in medicine* 83.2, pp. 479–491 (cit. on p. 32).

Quesson, Bruno, Frédéric Vimeux, Rares Salomir, Jacco A de Zwart, and Chrit TW Moonen (2002). “Automatic control of hyperthermic therapy based on real-time Fourier analysis of MR temperature maps”. In: *Magnetic Resonance in Medicine: An Official Journal of the International Society for Magnetic Resonance in Medicine* 47.6, pp. 1065–1072 (cit. on pp. 99, 102).

Reddy, Neha K, Patrick Schlegel, Yoonjeong Lee, and Dinesh K Chhetri (2022). “3D reconstruction of phonatory glottal shape and volume: Effects of neuromuscular activation”. In: *The Laryngoscope* (cit. on pp. 47, 49).

Reiser, Maximilian F, Wolfhard Semmler, and Hedvig Hricak (2007). *Magnetic resonance tomography*. Springer Science & Business Media (cit. on pp. 10–14).

Rempp, Hansjörg, Rüdiger Hoffmann, Jörg Roland, et al. (2012). “Threshold-based prediction of the coagulation zone in sequential temperature mapping in MR-guided radiofrequency ablation of liver tumours”. In: *European radiology* 22.5, pp. 1091–1100 (cit. on p. 57).

Rieke, Viola and Kim Butts Pauly (2008). “MR thermometry”. In: *Journal of Magnetic Resonance Imaging: An Official Journal of the International Society for Magnetic Resonance in Medicine* 27.2, pp. 376–390 (cit. on pp. 2, 15, 16).

Rim, Yonghoon, David D McPherson, and Hyunggun Kim (2013). “Volumetric three-dimensional intravascular ultrasound visualization using shape-based nonlinear interpolation”. In: *Biomedical engineering online* 12, pp. 1–15 (cit. on pp. 48, 49).

Ristovski, Gordan, Nicole Garbers, Horst K Hahn, Tobias Preusser, and Lars Linsen (2019). “Uncertainty-aware visual analysis of radiofrequency ablation simulations”. In: *Computers & Graphics* 79, pp. 24–35 (cit. on pp. 70, 71).

Ritter, Felix, Tobias Boskamp, André Homeyer, et al. (2011). “Medical image analysis”. In: *IEEE pulse* 2.6, pp. 60–70 (cit. on p. 36).

Roujol, Sébastien, B Denis de Senneville, Silke Hey, Chrit Moonen, and Mario Ries (2011). "Extended Kalman filtering for MR-thermometry guided high intensity focused ultrasound using the bio heat transfer equation". In: *2011 18th IEEE International Conference on Image Processing*. IEEE, pp. 2281–2284 (cit. on p. 97).

Ruiter, Simeon JS, Wouter J Heerink, and Koert P de Jong (2019). "Liver microwave ablation: a systematic review of various FDA-approved systems". In: *European radiology* 29.8, pp. 4026–4035 (cit. on p. 44).

Salomir, Rares, Magalie Viallon, Antje Kickhefel, et al. (2011). "Reference-free PRFS MR-thermometry using near-harmonic 2-D reconstruction of the background phase". In: *IEEE transactions on medical imaging* 31.2, pp. 287–301 (cit. on p. 64).

Sapareto, Stephen A and William C Dewey (1984). "Thermal dose determination in cancer therapy". In: *International Journal of Radiation Oncology* Biology* Physics* 10.6, pp. 787–800 (cit. on pp. 72, 73).

Seasons, Graham M, Erin L Mazerolle, Tejas Sankar, et al. (2019). "Predicting high-intensity focused ultrasound thalamotomy lesions using 2D magnetic resonance thermometry and 3D Gaussian modeling". In: *Medical physics* 46.12, pp. 5722–5732 (cit. on pp. 48, 49).

Senneville, Baudouin Denis de, Charles Mougenot, Bruno Quesson, et al. (2007). "MR thermometry for monitoring tumor ablation". In: *European radiology* 17.9, pp. 2401–2410 (cit. on p. 2).

El-Sharkawy, AbdEl Monem, Michael Schär, Paul A Bottomley, and Ergin Atalar (2006). "Monitoring and correcting spatio-temporal variations of the MR scanner's static magnetic field". In: *Magnetic resonance materials in Physics, Biology and Medicine* 19.5, pp. 223–236 (cit. on p. 16).

Simon, Caroline J, Damian E Dupuy, and William W Mayo-Smith (2005). "Microwave ablation: principles and applications". In: *Radiographics* 25.suppl_1, S69–S83 (cit. on p. 16).

Su, Tianyun, Wen Wang, Haixing Liu, et al. (2020). "An adaptive and rapid 3D Delaunay triangulation for randomly distributed point cloud data". In: *The Visual Computer*, pp. 1–25 (cit. on pp. 47, 49).

Sunday, Dan (2004). "Fast winding number inclusion of a point in a polygon". In: *Dostupné z:¡ http://softsurfer. com/Archive/algorithm 0103/algorithm 0103. htm* (cit. on p. 55).

Sung, Hyuna, Jacques Ferlay, Rebecca L Siegel, et al. (2021). "Global cancer statistics 2020: GLOBOCAN estimates of incidence and mortality worldwide for 36 cancers in 185 countries". In: *CA: a cancer journal for clinicians* 71.3, pp. 209–249 (cit. on pp. 1, 44).

Svedin, Bryant T, Allison Payne, Bradley D Bolster Jr, and Dennis L Parker (2018). "Multiecho pseudo-golden angle stack of stars thermometry with high spatial and temporal resolution using k-space weighted image contrast". In: *Magnetic resonance in medicine* 79.3, pp. 1407–1419 (cit. on pp. 29, 30).

Svedin, Bryant T, Allison Payne, and Dennis L Parker (2016). "Respiration artifact correction in three-dimensional proton resonance frequency MR thermometry using phase navigators". In: *Magnetic resonance in medicine* 76.1, pp. 206–213 (cit. on pp. 29, 30).

Tehrani, Masoud HH, M Soltani, Farshad Moradi Kashkooli, and Kaamran Raahemifar (2020). “Use of microwave ablation for thermal treatment of solid tumors with different shapes and sizes—A computational approach”. In: *Plos one* 15.6, e0233219 (cit. on p. 1).

Tillander, Matti, Steffen Hokland, Julius Koskela, et al. (2016). “High intensity focused ultrasound induced in vivo large volume hyperthermia under 3D MRI temperature control”. In: *Medical physics* 43.3, pp. 1539–1549 (cit. on pp. 31, 32).

Todd, Nick, Allison Payne, and Dennis L Parker (2010). “Model predictive filtering for improved temporal resolution in MRI temperature imaging”. In: *Magnetic resonance in medicine* 63.5, pp. 1269–1279 (cit. on p. 97).

Todd, Nick, Jaya Prakash, Henrik Odéen, et al. (2014). “Towards real-time availability of 3D temperature maps created with temporally constrained reconstruction”. In: *Magnetic resonance in medicine* 71.4, pp. 1394–1404 (cit. on pp. 29, 30).

Tomasian, Anderanik, Afshin Gangi, Adam N Wallace, and Jack W Jennings (2018). “Percutaneous thermal ablation of spinal metastases: recent advances and review”. In: *American Journal of Roentgenology* 210.1, pp. 142–152 (cit. on pp. 1, 26).

Toupin, Solenn, Pierre Bour, Matthieu Lepetit-Coiffé, et al. (2017). “Feasibility of real-time MR thermal dose mapping for predicting radiofrequency ablation outcome in the myocardium in vivo”. In: *Journal of Cardiovascular Magnetic Resonance* 19.1, pp. 1–12 (cit. on pp. 31, 32).

Van Aelst, Stefan and Peter Rousseeuw (2009). “Minimum volume ellipsoid”. In: *Wiley Interdisciplinary Reviews: Computational Statistics* 1.1, pp. 71–82 (cit. on pp. 47, 49).

Verhaart, René F, Gerda M Verduijn, Valerio Fortunati, et al. (2015). “Accurate 3D temperature dosimetry during hyperthermia therapy by combining invasive measurements and patient-specific simulations”. In: *International Journal of Hyperthermia* 31.6, pp. 686–692 (cit. on pp. 100, 102).

Viallon, Magalie, Sylvain Terraz, Joerg Roland, et al. (2010). “Observation and correction of transient cavitation-induced PRFS thermometry artifacts during radiofrequency ablation, using simultaneous Ultrasound/MR imaging”. In: *Medical physics* 37.4, pp. 1491–1506 (cit. on p. 72).

VilasBoas-Ribeiro, Iva, Sven AN Nouwens, Sergio Curto, et al. (2022). “POD–Kalman filtering for improving noninvasive 3D temperature monitoring in MR-guided hyperthermia”. In: *Medical Physics* (cit. on pp. 1, 33).

Wan, Min, Wei Huang, Jun-Mei Zhang, et al. (2015). “Variational reconstruction of left cardiac structure from CMR images”. In: *PloS one* 10.12, e0145570 (cit. on pp. 46, 49).

Watson, David F (1981). “Computing the n-dimensional Delaunay tessellation with application to Voronoi polytopes”. In: *The computer journal* 24.2, pp. 167–172 (cit. on pp. 46, 52).

Wissler, Eugene H (1998). “Pennes’ 1948 paper revisited”. In: *Journal of applied physiology* 85.1, pp. 35–41 (cit. on pp. 4, 64, 105).

Xiong, Huahui, Xiaoqing Huang, Yong Li, et al. (2015). “A method for accurate reconstructions of the upper airway using magnetic resonance images”. In: *Plos one* 10.6, e0130186 (cit. on pp. 47, 49).

Xue, Hui, Yu Ding, Christoph Guetter, et al. (2011). “Motion compensated magnetic resonance reconstruction using inverse-consistent deformable registration: application to real-time cine imaging”. In: *Medical Image Computing and Computer-Assisted Intervention–MICCAI 2011: 14th International Conference, Toronto, Canada, September 18-22, 2011, Proceedings, Part I 14*. Springer, pp. 564–572 (cit. on p. 41).

Yang, Gang, Yongfu Xiong, Ji Sun, et al. (2020). “The efficacy of microwave ablation versus liver resection in the treatment of hepatocellular carcinoma and liver metastases: A systematic review and meta-analysis”. In: *International Journal of Surgery* 77, pp. 85–93 (cit. on p. 44).

Yu, Weimin, Chengwen Chu, Moritz Tannast, and Guoyan Zheng (2016). “Fully automatic reconstruction of personalized 3D volumes of the proximal femur from 2D X-ray images”. In: *International journal of computer assisted radiology and surgery* 11, pp. 1673–1685 (cit. on pp. 47, 49).

Yung, Joshua P, Anil Shetty, Andrew Elliott, et al. (2010). “Quantitative comparison of thermal dose models in normal canine brain”. In: *Medical physics* 37.10, pp. 5313–5321 (cit. on pp. 4, 89).

Zhang, Jinao and Sunita Chauhan (2019a). “Neural network methodology for real-time modelling of bio-heat transfer during thermo-therapeutic applications”. In: *Artificial Intelligence in Medicine* 101, p. 101728 (cit. on pp. 101, 102).

– (2019b). “Real-time computation of bio-heat transfer in the fast explicit dynamics finite element algorithm (FED-FEM) framework”. In: *Numerical Heat Transfer, Part B: Fundamentals* 75.4, pp. 217–238 (cit. on p. 105).

Zhang, Jinao, Sunita Chauhan, Wa Cheung, and Stuart K Roberts (2021). “Thermal Dose Modeling for Thermal Ablative Cancer Treatments by Cellular Neural Networks”. In: *Machine Learning in Medicine*. Chapman and Hall/CRC, pp. 27–54 (cit. on p. 92).

Zhang, Le, Tess Armstrong, Xinzhou Li, and Holden H Wu (2019). “A variable flip angle golden-angle-ordered 3D stack-of-radial MRI technique for simultaneous proton resonant frequency shift and T1-based thermometry”. In: *Magnetic resonance in medicine* 82.6, pp. 2062–2076 (cit. on p. 30).

Zhang, Yuxin, Shuo Chen, Kexin Deng, et al. (2016). “Kalman filtered bio heat transfer model based self-adaptive hybrid magnetic resonance thermometry”. In: *IEEE transactions on medical imaging* 36.1, pp. 194–202 (cit. on p. 64).

Zhao, Yuanyu, Ting Chen, Hui Wang, et al. (2022). “Influence of Three-Dimensional Visual Reconstruction Technology Combined with Virtual Surgical Planning of CTA Images on Precise Resection of Liver Cancer in Hepatobiliary Surgery”. In: *Computational and Mathematical Methods in Medicine* 2022 (cit. on pp. 47, 49).

Zhu, Mingming, Ziqi Sun, and Chin K Ng (2017). “Image-guided thermal ablation with MR-based thermometry”. In: *Quantitative imaging in medicine and surgery* 7.3, pp. 356–368 (cit. on p. 44).

Zou, Chao, Changjun Tie, Min Pan, et al. (2016). “Referenceless MR thermometry—a comparison of five methods”. In: *Physics in Medicine & Biology* 62.1, p. 1 (cit. on pp. 119, 122).

Zucconi, Fabio, Paola E Colombo, Stefano Pasetto, et al. (2014). “Analysis and reduction of thermal dose errors in MRgFUS treatment”. In: *Physica Medica* 30.1, pp. 111–116 (cit. on pp. 71, 72).

List of Figures

List of Tables